Implementation and validation of the linear collider final focus prototype: ATF2 at KEK (Japan)

Y. Renier

▶ To cite this version:

Y. Renier. Implementation and validation of the linear collider final focus prototype: ATF2 at KEK (Japan). High Energy Physics - Experiment [hep-ex]. Université Paris Sud - Paris XI, 2010. English. NNT : . tel-00523218

HAL Id: tel-00523218
https://theses.hal.science/tel-00523218

Submitted on 4 Oct 2010

LAL 10-91
Juin 2010

THÈSE

Présentée le 11 juin 2010

Par

Yves Renier

Pour obtenir le grade de

Docteur ès Sciences
De l'Université Paris XI Orsay

Implementation and validation of the linear collider final focus prototype : ATF2 at KEK (Japan)

Soutenue devant la commission d'examen composée de :

M.	Ph.	Bambade	Directeur de thèse
M.	Ph.	Burrows	Rapporteur
M.	P.	Puzo	
M.	G.	Russell White	
M.	T.	Tauchi	Codirecteur de thèse
M.	A.	Variola	
M.	G.	Wormser	Président
M.	F.	Zimmermann	Rapporteur

ABSTRACT

A future e^+/e^- linear collider is planned to be built in order to obtain precise measurements (at the TeV scale) which would be complementary to the ones from the LHC. One of the challenges of this linear collider will be to focus the beam down to nanometer level transverse sizes at the interaction point, to obtain a high luminosity of a few $10^{-34}cm^2s^{-1}$. The two linear collider projects (ILC and CLIC) require beam delivery systems with the same local chromaticity correction scheme in the final focus.

ATF2 at KEK (Japan), an implementation of this scheme scaled down in energy, uses the beam extracted from ATF, which is one of the most successful damping rings in the world. The ATF2 goals are to prove the feasibility and the stability of the linear collider final focus system and to define and test the experimental correction procedures. The nominal beam sizes at the interaction point are $3\mu m$ horizontally and $37nm$ vertically.

The work in this thesis was started before the commissioning and covered its first year at KEK.

At the beginning, we observed that the striplines BPMs were not working properly so we investigated their behavior in detail. The problem was characterized and later solved in 2010 by upgrading the electronics. We then developed an efficient procedure to check the modeling of the beam line, comparing measurements of transfer matrices to model predictions calculated on line. After obtaining a good agreement, we were able to successfully test the trajectory correction algorithm which had been developed, reducing the difference between BPM measurements and the target values down to $0.5mm$ horizontally and $0.2mm$ vertically. We also successfully developed an algorithm to reconstruct pulse to pulse beam trajectory fluctuations with sub-micron precision. This reconstruction also gave a precise determination of the energy fluctuation, allow-

ing a global fit of the dispersion function along the beam line with a precision of a few mm, dominated by systematic errors from transfer matrices and BPMs scale factor uncertainties.

A simple and robust IP beam size tuning method using sextupoles displacements was also studied in simulation, whose performance indicates that, given some assumptions on the error level of the beam, convergence within 20% of the nominal beam size should be possible in 8 hours with a 80% probability. The first experimental tests of such beam size tuning methods, based on measurements at the interaction point are on-going in 2010 and 2011.

RÉSUMÉ

La construction d'un futur collisionneur linéaire e^+/e^- est prévue pour obtenir des mesures précises (à l'échelle du TeV) qui seraient complémentaires de celles obtenues du LHC. Un des défis de ce collisionneur linéaire sera de focaliser le faisceau à des tailles transverses nanométriques au point d'interaction, afin d'obtenir une importante luminosité de quelques $10^{-34}cm^2s^{-1}$. Les deux projets de collisionneur linéaire (ILC et CLIC) requièrent un système de distribution du faisceau partageant le même schéma de correction de chromaticité locale dans le système de focalisation finale.

ATF2 à KEK (Japon), une implémentation de ce schéma mis à l'échelle en énergie, utilise le faisceau extrait d'ATF, qui est un des meilleurs anneaux d'amortissement au monde. Les objectifs d'ATF2 sont de prouver la faisabilité et la stabilité du système de focalisation finale et de définir et tester les procédures de corrections expérimentales. Les tailles nominales du faisceau au point d'interaction sont de $3\mu m$ horizontalement et $37nm$ verticalement.

Le travail de thèse a commencé avant la mise en service et en couvre la première année à KEK.

Au début, nous avons observé que les BPMs 'stripline' ne fonctionnaient pas correctement, nous avons donc examiné leurs comportements en détail. Le problème a été caractérisé puis résolu plus tard, en 2010, en changeant l'électronique. Nous avons alors développé une procédure efficace pour vérifier la modélisation de la ligne de faisceau, en comparant les mesures des matrices de transfert aux prédictions du modèle calculé en direct. Après avoir obtenu un bon accord, nous avons pu tester avec succès l'algorithme de correction de trajectoire que nous avions développé, réduisant la différence entre les mesures obtenues par les BPMs et les valeurs cibles jusqu'à $0.5mm$ horizontalement et $0.2mm$ verticalement. Nous avons aussi développé avec succès un

algorithme pour reconstruire les fluctuations de la trajectoire du faisceau pour chaque paquet avec une résolution inférieure au micron. Cette reconstruction détermine aussi les fluctuations en énergie, permettant un ajustement général de la fonction de dispersion sur la longueur de la ligne de faisceau avec une précision de quelques millimètres, dominé par les erreurs systématiques provenant des matrices de transfert et des incertitudes sur les facteurs d'échelles des BPMs.

Une méthode simple et robuste de réglage de la taille du faisceau à l'IP utilisant des déplacements de sextupoles a aussi été étudiée en simulation. Les performances indiquent que, en faisant quelques hypothèses sur le niveau d'erreur du faisceau, la convergence à 20% de la taille nominale devrait être possible en 8 heures avec une probabilité de 80%. Les premiers résultats expérimentaux de telles méthodes de réglages de la taille du faisceau sont actuellement en cours pour 2010 et 2011.

TABLE OF CONTENTS

Page

Table of Contents i

List of Figures v

List of Tables xi

Chapter 1: Introduction 1

Chapter 2: Linear Colliders 11
- 2.1 Relevance of a Future Linear Collider 11
  - 2.1.1 The Partner of the LHC 11
  - 2.1.2 The physics Looked for 12
- 2.2 Linear Collider designs 14
  - 2.2.1 Specificities of Linear Colliders and Parameter Optimisation 14
  - 2.2.2 Main Components 18
  - 2.2.3 The Beam Delivery System 23

Chapter 3: The ATF2 project 25
- 3.1 Project Description 25
  - 3.1.1 Overview of ATF Project 25
  - 3.1.2 Goals of ATF2 27
  - 3.1.3 Planning of the Commissioning 31
- 3.2 Optics 31
  - 3.2.1 The Different Sections 31
  - 3.2.2 The Local Chromaticity Correction 34
  - 3.2.3 Tolerances 38

Chapter 4: The Instrumentation at ATF2 45
  4.1 Beam Position and Tilt Monitors 45
    4.1.1 Stripline BPMs 45
    4.1.2 Cavity BPMs 45
    4.1.3 Interaction Point BPM 48
    4.1.4 Tilt Monitor 49
  4.2 Beam Size Measurement 50
    4.2.1 Wire-Scanners 50
    4.2.2 Optical Transition Radiation Monitor 51
    4.2.3 Laser Wire 54
    4.2.4 "Shintake" Monitor 55

Chapter 5: Work Done on Stripline BPMs Electronics 59
  5.1 Description of the Stripline BPMs and Electronics 62
    5.1.1 Stripline BPMs 62
    5.1.2 Head-Amp Circuit 67
    5.1.3 Clipping Circuit 68
  5.2 Check of the Electronics 68
  5.3 Tuning of the Clipping Circuit 69
    5.3.1 Tuning of the Amplifier Offsets 69
    5.3.2 Tuning of the Clipping Level 70
  5.4 Study of the Calibration Procedure 70
    5.4.1 Kicker Noise Effects 70
    5.4.2 Stability of the Calibration 71
  5.5 Improvements 75

Chapter 6: Procedure to Achieve a Vertical Beam Size of 37 nm 77
  6.1 Overview of the Tuning Procedure 77
  6.2 Trajectory Correction 78
    6.2.1 Beam Based Alignment 78
    6.2.2 Trajectory Steering 80
  6.3 Corrections in the Extraction Line 80
    6.3.1 Dispersion Correction 80

6.3.2 Coupling Correction 81
6.3.3 Beta Matching 82
6.4 Corrections in the Final Focus 82
6.4.1 Waist Position Correction 82
6.4.2 Dispersion Correction 84
6.4.3 Coupling Correction 84
6.4.4 Other Higher Order Aberration Corrections 85
6.5 Overview of the 2009 ATF Commissioning Runs 85

Chapter 7: The ATF2 Flight Simulator 87
7.1 Principle 87
7.1.1 Present Control System 87
7.1.2 The ATF2 Flight Simulator Concept 88
7.1.3 Architecture 89
7.2 Built-in Abilities 91
7.2.1 The Flight Simulator Server 91
7.2.2 The Flight Simulator Client 92
7.2.3 Security and Other Issues 93
7.3 Developed Tools 94
7.3.1 Transfer Matrix Checks 95
7.3.2 Trajectory Correction 97
7.3.3 Trajectory Reconstruction and Dispersion Measurement . 98

Chapter 8: Experimental Results 101
8.1 Transfer Matrix Measurements 101
8.2 Static Trajectory Correction 107
8.2.1 Principle of the Average Trajectory Correction 107
8.2.2 Simulation Results 110
8.2.3 Experimental Correction 114
8.3 Trajectory Fluctuation Reconstruction 116
8.3.1 Principle of Pulse to Pulse Trajectory Fluctuation Reconstruction 121
8.3.2 BPMs Noise Level Measurements 122
8.3.3 Experimental Fluctuation Determination 123

8.4 Dispersion Measurement 131
8.4.1 Principle of the Dispersion Measurement 131
8.4.2 Dispersion Correction 133
8.4.3 Comparison of two Dispersion Reconstruction Methods . . 138

Chapter 9: Beam Size Tuning 145
9.1 Correction Moving Sextupoles 145
9.1.1 Effect of Sextupole Displacements 145
9.1.2 Knob Determination 153
9.1.3 Simulation results 157

Chapter 10: Conclusion and Prospects 165
10.1 Conclusion 165
10.2 Prospects 166

Appendix A: Linear Optics 169
A.1 Twiss Parameters 169
A.1.1 Beam Motion in magnet systems 169
A.1.2 Twiss Functions 170
A.2 Transfer Matrices 172
A.2.1 Drift space 173
A.2.2 Quadrupole Magnet 173
A.2.3 Skew Quadrupole Magnet 175
A.2.4 Sector Magnet 175
A.2.5 Sextupole 176

Greetings, Remerciments 178

Bibliography 181

LIST OF FIGURES

Figure Number Page

1.1 Hadron and leptons colliders from 1970 to present days. 2
1.2 ATF layout before ATF2 construction. 4
1.3 ATF2 layout. 4
2.1 Cross section for possible states accessible at a linear collider. . . 13
2.2 Standard Model and Supersymmetry "partners" particles. 14
2.3 A schematic layout of the International Linear Collider. 18
2.4 A schematic layout of the Compact LInear Collider. 19
2.5 The ATF photo-cathode RF gun. 19
2.6 Baseline of the positron source scheme 20
2.7 Laser Compton scattering scheme for the positron source 21
2.8 A cell of 9 ILC prototype superconducting cavities. 23
2.9 Principle of a bunch compressor. 23
3.1 Layout of ATF before ATF2 construction. 26
3.2 ATF2 beam line. 29
3.3 Layout of the extraction inflector. 29
3.4 Layout of the extraction diagnostic section. 30
3.5 Layout of the final focus section. 30
3.6 Twiss parameters of the extraction inflector with the transfer matrix between the two kickers. 32
3.7 Twiss parameters of the extraction diagnostic section with phase advances between skew quadrupoles and wire scanners 33
3.8 Twiss parameters of the final focus section. 35
3.9 Scheme of the non-local chromaticity correction scheme. 36
3.10 Scheme of the local chromaticity correction 37
3.11 Vertical displacement of the beam at the IP for a one micron displacement of each magnet, applied one at the time. 39

3.12 Vertical beam size at the IP for a one micron displacement of each magnet, applied one at the time 40
3.13 Vertical displacement of the indicated magnet giving a 2% increase of the beam size in ATF2 and ILC. 41
3.14 Roll of the indicated magnet giving a 2% increase of the beam size in ATF2 and ILC. 42
3.15 Field error of the indicated magnet giving a 2% increase of the beam size in ATF2 and ILC. 43

4.1 Quarter view of the inside surface of a cavity BPM. 46
4.2 Fields of the TM_{110} mode, also called dipole mode. 47
4.3 The MSF1FF S-band cavity BPM and SF1FF sextupole in assembly in the ATF2 final focus. 48
4.4 The block of 2 IPBPMs structure. 49
4.5 Scheme of the tilt monitor. 50
4.6 Wire-scanner in the ATF2 diagnostic section. 52
4.7 Scheme of the OTR installed in the ATF2 extraction line. 53
4.8 Schematics of the laser wire apparatus. 54
4.9 Schematics of the "Shintake" monitor. 56
4.10 Expected resolution curves of beam size measurement in different crossing angles. 56

5.1 Orbits and spread of the offset between BPMs and magnet centers after several beam based alignment implementations 60
5.2 Beam position measured by the indicated stipline BPM function of the intensity of the beam for different beam positions in the stripline. 61
5.3 Transverse and longitudinal scheme of a stripline BPM. 62
5.4 Schematic of the ATF2 extraction line with the stripline BPM locations. 63
5.5 Shape of the signal at the output of a stripline BPM. 64
5.6 Frequency response of the striplines. 65
5.7 Head-amp electronics of stripline BPMs. 67
5.8 Clipping circuit electronics of stripline BPMs. 68
5.9 Kicker induced signal at MQF1X and its FFT before the head amp circuit. 72

5.10 Kicker induced signal at MQF1X and after the head amp circuit. 73
5.11 Fractional differences between the signal on each of the four electrodes of MQF1X and the fitted polynomials obtained during the calibration without the kicker. 74
5.12 Relative spread of the ADC counts function of the attenuation for MQF1X, MQF4X and MQF9X. 75

6.1 Typical measurements at a downstream BPM during a Beam Based Alignment. 79
6.2 Comparison of the measured dispersion (varying the ring cavity frequency), the design dispersion and the estimation of result of the calculated corrections. 81
6.3 Square of the vertical beam size as a function of QF5X intensity. 83

7.1 Scheme of the ATF2 Flight Simulator. 90
7.2 The Flight Simulator server. 92
7.3 The Flight Simulator client. 93
7.4 The Transfer Matrix Check tool. 96
7.5 The Trajectory Correction tool. 97
7.6 The Trajectory Reconstruction and Dispersion Measurement tool. 99

8.1 Comparison of measured transfer matrices between ZH4X and ZV8X correctors and all BPMs with the optics model reconstructed from the currents of the magnets. 103
8.2 Comparison between the displacement measured in all BPM, normalized to the vertical displacement of the QM15FF mover, and the model prediction. 104
8.3 The transfer matrix diagnostic tool interface in the Flight Simulator environment. 105
8.4 Result of the steering algorithm with nominal errors and optics. . 112
8.5 Result of the steering algorithm with large errors and nominal optics. 113
8.6 Result of the steering algorithm with large errors and high beta optics. 115
8.7 Result of first experimental horizontal steering. 117
8.8 Result of the second experimental steering. 118
8.9 Results of the third experimental steering (horizontal). 118

8.10 Results of the fourth experimental steering. 119
8.11 Result of the fifth experimental steering. 119
8.12 Result of the final focus steering (vertical). 120
8.13 Determination of horizontal and vertical BPM resolutions using correlation analysis. 124
8.14 Reconstruction of the parameters at the injection point during a dispersion measurement. 125
8.15 Histogram of the errors on the reconstruction of the energy in figure 8.14. 126
8.16 Fit of the momentum compaction factor. 127
8.17 Horizontal and vertical resolution of the BPMs along with the fit resolution. 129
8.18 Energy jitter reconstructed. 130
8.19 Amplitude of the jitter reconstructed normalized to the corresponding beam size. 130
8.20 Two methods for horizontal dispersion fit at MQF1X. 140
8.21 Reconstructed dispersion compared to individual BPM measurements based on changing the ring cavity frequency. 141
8.22 Reconstructed dispersion compared to individual BPM measurements based on using beam fluctuations. 141

9.1 $\overline{X}$ and $\overline{X'}$ positions of the electrons with or without a quadrupole field. 148
9.2 Nominal β function and dispersion function in the final focus. . . 152
9.3 Horizontal and vertical phases along ATF2. 153
9.4 Proportion of seeds which has a vertical beam size below $1.2\times$, $2.4\times$ and $12\times$ the nominal beam size after 800 beam size measurements function of the misalignment factor. 161
9.5 Proportion of seeds which has reached 110% of the minimal achieved size before the step 200, 400 and 800. 163

A.1 Curved coordinate system following a reference trajectory. 169
A.2 Beam ellipse function of the twiss functions. 171
A.3 Field (quarter profile) of a quadrupole magnet. The iron core is shown in blue and conductors in yellow. 174
A.4 Field (half of a profile) and shape (top view) of a sector magnet. . 176

A.5 Field (half of a profile) of a sextupole magnet. 177

LIST OF TABLES

Table Number Page

2.1 Comparison of the parameters of ILC, CLIC and ATF2 17

3.1 Major ATF performances. 26

5.1 Characteristics of the stripline BPMs 63

5.2 Stripline errors sum-up. 75

8.1 Table of the set of errors parameters take into account in the simulation 110

8.2 Simulation results of the steering. 114

8.3 Comparison of the two dispersion fit methods using MQD10X or IP as reference point. 142

Chapter 1

INTRODUCTION

The progress made in particle physics has been closely related to the improvements of the accelerators and there is no reason that will change. Also, the research and development on the next accelerators has been made at the same time as the exploitation of the present ones. With the increase of their size and complexity, this becomes even more necessary.

There are two ways to explore the sub-atomic world, the first is to go to higher energy to discover new particles and measure their properties, the second is to increase the precision of the measurements to detect rare processes and make detailed studies. Higher energies has been usually explored with hadron colliders and the precision measurements has been done afterwards by lepton colliders (see figure 1.1), demonstrating a complementarity between them.

The exploitation of the Large Hadron Collider (LHC) has just started and for a long time research has been done on a future complementary high energy linear e^-e^+ collider. A linear electron-positron collider provides more precise measurements as it involves elementary particles. To reach high statistics (and so high precision measurements) and high energy, a linear accelerator has to solve challenges, in particular obtain very small transverse beam sizes (at the nanometer level), sub-nanometer stability at the Interaction Point (IP) and develop an efficient acceleration technology. Getting similar results, the energy can be lowered (the energy is proportional to the length of the linac and so almost proportional to its cost) if the statistics is increased (reducing the beam

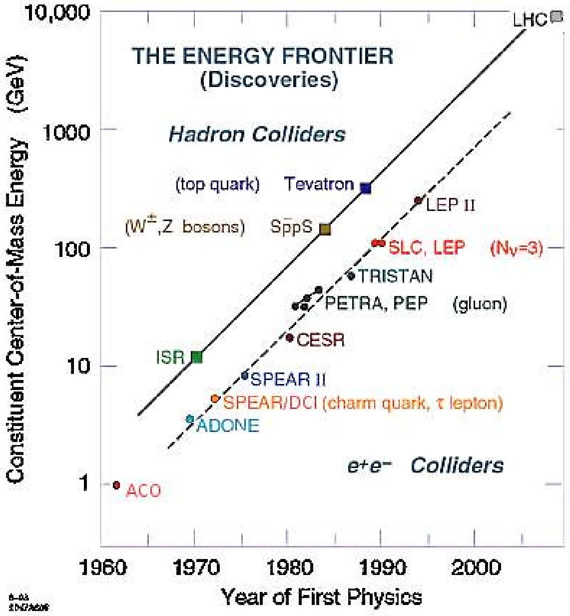

Figure 1.1: Hadron (square) and leptons (point) colliders from 1970 to present days.

size at IP).

To keep the cost of the future linear collider as low as possible, extensive research has been made on both acceleration and focusing. The research on the acceleration has led to two designs:

- The International Linear Collider (ILC), based on superconducting cavity technology, with a nominal center-of-mass energy of $500MeV$
- The Compact Linear Collider (CLIC), based on a two-beam-acceleration concept, with a nominal center-of-mass energy of $3TeV$.

Both share the same final focus line concept which requires the collision of nanometer scale vertical beam sizes.

The ATF2 project is a part of the global effort to prove the feasibility of a linear collider. Its goal is to achieve the small beam sizes, the stability required and to train the next generation of physicist in an international collaboration. ATF2 will continue the work done on these topics on the Final Focus Test Beam (FFTB) and Stanford Linear Collider (SLC) facility at SLAC and will try to address the concerns remaining after these experiments. These concerns are mainly the test of the local chromaticity correction scheme never implemented yet, the stability and the reproducibility of the operations with a linac, only experimented in the SLC but with much larger beam size at the IP ($\simeq 1\mu m$).

ATF2 (see figure 1.3) is an extension of the Accelerator Test Facility (ATF, see figure 1.2) which has been a successful test facility for the linear collider. ATF2 will use the beam extracted from the ATF damping ring, with the smallest emittances of the world. These emittances are needed to reach nanometer transverse beam size. Like ATF, it will also be used as a test facility for new instruments, most of them prototypes for the future linear collider.

ATF2 construction was completed in December 2008 and the commissioning started with only a few of the magnets turned on to make basic hardware and software checks. The ATF2 runs in 2009 were done using higher beta optics than the nominal one, with all the quadrupoles magnets switched on, to test in a relaxed environment the tuning procedures and to initial operation of the hardware. The commissioning program had a direct influence on the presented work because we focused on what was needed at that time (instrumentation tests, control system, characterization of the optics and first correction algorithms) to help as much as possible the collaboration and to get experimental data.

The scientific relevance and a description of the two concepts of future linear colliders will be summarized in chapter 2. ATF and ATF2 projects are described in chapter 3 and a quick overview of the available instrumentation is given in chapter 4.

A deeper description of the stripline BPMs and their electronics as well as

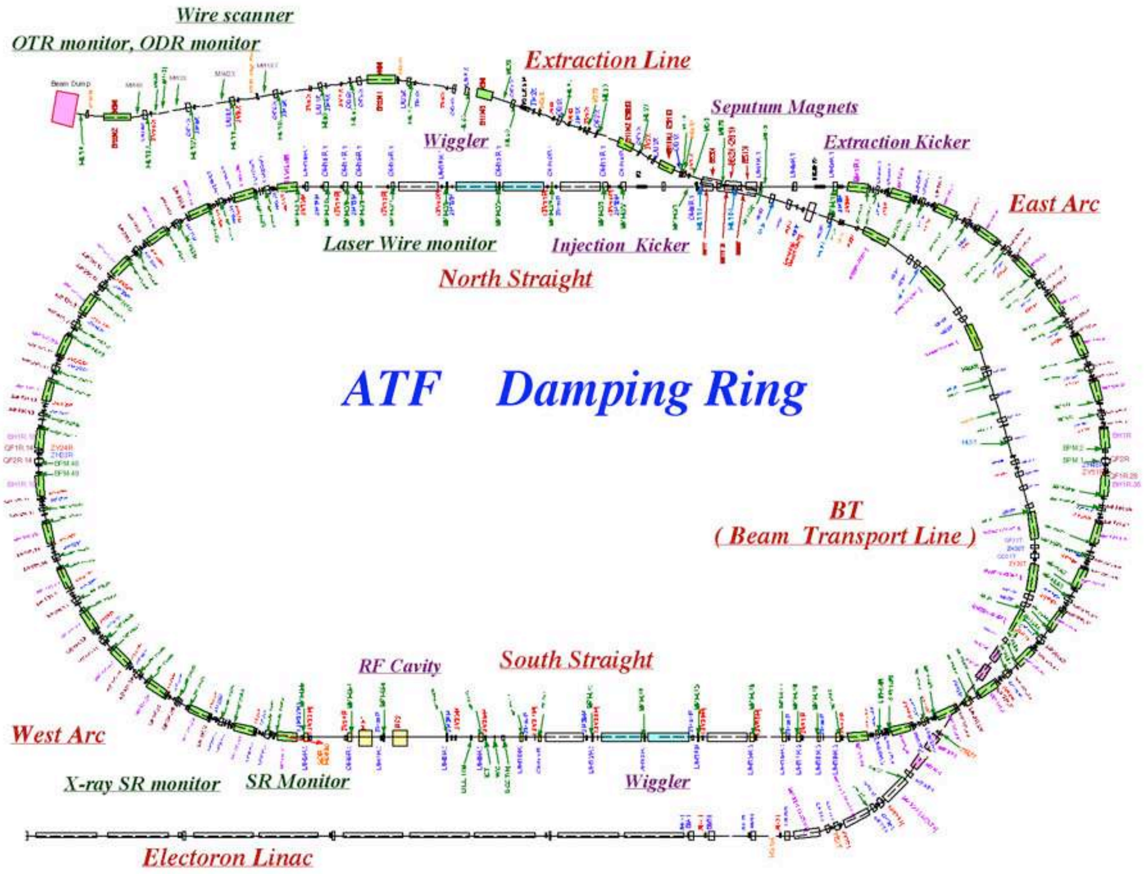

Figure 1.2: ATF layout before ATF2 construction.

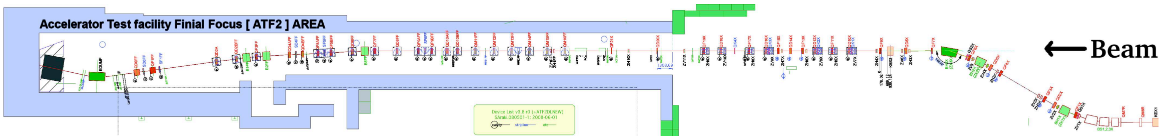

Figure 1.3: ATF2 layout.

the tuning done is presented in chapter 5. The overall ATF2 tuning procedure is described in chapter 6 as well as an overview of the 2009 ATF2 commissioning runs.

An attractive control system concept allowing off-line development adapted to the ATF2 global collaboration and including a simulation mode is described in chapter 7. The tools developed and made available to the collaboration are included as well.

The chapter 8 includes: the linear optics formalism, a comparison between the ATF2 "on-line" model and the measurement, as well as the principles and results of the implemented average trajectory correction, trajectory variation reconstruction and dispersion measurements based on beam fluctuation.

A simple beam size tuning method displacing the Final Focus (FF) sextupoles is shown with simulation results in chapter 9, just before the conclusion and prospects in chapter 10.

INTRODUCTION

Les progrès accomplis en physiques des particules ont été fortement corrélés avec les améliorations faites sur les accélérateurs, et cela n'a aucune raison de changer. Aussi, la recherche et le développement sur les prochains accélérateurs a été effectuée en parralèlle avec l'exploitation des accélérateurs actuels et cela devient encore plus une nécessité avec l'accroissement de leur taille et de leur complexité.

Il y a deux manières d'explorer le monde sub-atomique. La première est d'augmenter l'énergie pour découvrir de nouvelles particules et mesurer leurs propriétés; la seconde est d'augmenter la précision des mesures pour détecter des processus rares et faire des études détaillées. Les plus hautes énergies sont le plus souvent explorées avec des collisionneurs hadroniques, et les mesures de précisions sont par la suite faites par des collisionneurs leptoniques (voir la figure 1.1). Ceci démontre leur complémentarité.

L'exploitation du Large Hadron Collider (LHC) vient juste de commencer et, depuis longtemps, des recherches ont été faites sur un collisionneur leptonique complémentaire. Celui-ci sera un collisionneur d'électrons et de positrons ; il fournira des mesures plus précises en utilisant des particules élémentaires. Pour atteindre une statistique importante (et donc des mesures précises) ainsi qu'une grande énergie, un accélérateur linéaire doit résoudre plusieurs défis : obtenir une taille transverse très petite (à l'échelle nanométrique), une stabilité sub-nanométrique au point d'interaction (IP), et développer une technologie d'accélération efficace. Pour des résultats similaires, l'énergie peut être diminuée (l'énergie étant proportionnelle à la taille du linac et donc à son coût) si la statistique est augmentée (en réduisant la taille du faisceau à l'IP).

Afin de garder le coût du futur collisionneur linéaire aussi bas que possible, des recherches poussées ont été faites à la fois sur l'accélération et la focalisation. Les recherches sur l'accélération ont conduit à deux projets :

- l'International Linear Collider (ILC), basé sur une technologie de cavités super-conductrices, avec une énergie nominale dans le centre de masse de $500MeV$
- Le Compact Linear Collider (CLIC), basé sur un concept d'accélération à deux faisceaux, avec une énergie nominale dans le centre de masse de $3TeV$.

Toutes les deux partagent le même concept de focalisation finale qui permet la collision de faisceaux de taille verticale nanométrique.

Le projet ATF2 fait partie de l'effort mondial pour démontrer la faisabilité d'un collisionneur linéaire. Son but est d'accomplir les petites tailles de faisceau, la stabilité requise et de former la prochaine génération de physiciens dans une collaboration internationale. ATF2 continuera le travail effectué sur le Final Focus Test Beam (FFTB) et sur le Standford Linear Collider (SLC) à SLAC et il abordera les questions restantes après ces expériences. Ces questions concernent principalement le test de la correction locale de chromaticité (qui n'a jamais été testée jusqu'à présent), la stabilité et la reproductibilité des opérations avec un linac (qui n'ont été testées que sur le SLC, mais avec des tailles de faisceaux beaucoup plus importantes à l'IP :$1\mu m$).

ATF2 est une extension de l'Accelerator Test Facility (ATF) qui a été une installation de test pour le collisionneur linéaire couronnée de succès. ATF2 utilisera le faisceau d'ATF qui produit les émittances les plus petites au monde. Ces émittances sont nécessaires pour obtenir les tailles transverses nanomètriques du faisceau. Comme ATF, il sera aussi utilisé comme installation de test pour de nouveaux instruments, dont la plupart sont des prototypes pour le futur collisionneur linéaire.

La construction d'ATF2 s'est terminée en décembre 2008 et la mise en service a commencé avec seulement quelques uns des aimants allumés pour faire des vérifications matérielles et logicielles basiques. Les opérations de 2009 ont été faites avec des optiques à plus grand β que les optiques nominales, en utilisant tous les aimants, afin de tester avec moins de contraintes les procédures de réglages et de développer le matériel. Le déroulement de la mise en service a eu une influence directe sur ce travail puisque nous nous sommes concentrés sur ce qui était nécessaire à ce moment (test de l'instrumentation, système de contrôle, caractérisation de l'optique et premiers algorithmes de corrections) afin d'aider autant que possible la collaboration et pour obtenir des données expérimentales.

La pertinence et une description des deux concepts de collisionneur linéaire seront résumées dans le chapitre 2. Les projets ATF and ATF2 sont décrits dans le chapitre 3 et un rapide aperçu de l'instrumentation présente est donné chapitre 4.

Une description plus détaillée des BPMs striplines ainsi que de leurs électronique et les réglages effectués sont donnés chapitre 5. La procédure de réglage générale d'ATF2 est décrite chapitre 6 ainsi qu'un historique de la mise en service de 2009.

Un concept intéressant de système de contrôle permettant un développement hors-ligne adapté à la collaboration mondiale d'ATF2 et incluant un mode de simulation est décrit dans le chapitre 7. Les outils développés et rendus accessibles à la collaboration sont aussi inclus.

Le chapitre 8 inclut : une comparaison entre le modèle en ligne d'ATF2 et les mesures, le fonctionnement et les résultats de la correction de trajectoire moyenne implémentée, la reconstruction des variations de trajectoire, et la mesure de la dispersion basée sur les fluctuations du faisceau.

Une méthode simple de réglage du faisceau déplaçant les sextupoles du FF est montrée avec ses résultats simulés au chapitre 9, juste avant la conclusion et les perspectives chapitre 10.

Chapter 2

LINEAR COLLIDERS

The LHC has been built to discover the Higgs boson and to explore the physics beyond the Standard Model, nevertheless, to get precise measurements, a lepton collider is planned to complement these discoveries. This chapter presents the relevance of this collider and includes an overview of the design of its main parameters for the case of ILC and CLIC.

2.1 Relevance of a Future Linear Collider

2.1.1 The Partner of the LHC

When two protons of the LHC collide, in fact it is the quarks, anti-quarks and gluons forming the proton which are colliding each of them sharing a poorly known part of the proton momentum, so the center-of-mass energy of the collision is not known precisely. Due to this uncertainty on the energy, a broader range of physical processes can be probed but it makes the analysis more complex and it has an impact on the precision of the final measurements. Strong interaction parasitic processes also make the analysis more complex through the background they generate.

When leptons, which are elementary particles, collide, the center-of-mass energy is much better known, allowing more precise measurement. On the other hand, you can study only one collision energy at the time. Also, leptons do not interact through the strong force, so the background level is lower than with hadron collisions.

That is why these two kinds of colliders are complementary: the hadron colliders are more adapted to look for interesting phenomena in a large range of energies, showing the way to the lepton colliders, which are able to make much more precise measurements.

However, due to the energy losses to synchrotron radiation at every turn : $\Delta E_{turn} = \frac{E^4}{3Rm^4c^8}$ (where m is the electron mass and c the speed of light), which are proportional to the fourth power of the particle energy E, there is a limit to the energy reachable in a circular accelerator for a reasonable radius. LEP2, with a beam energy $100 GeV$, even with a radius of $R = 4.2km$, almost reached that limit (for electrons and positrons) since $\sim 3\%$ of the energy was lost to synchrotron radiation each turn [1]. For this reason, the future e^+e^- collider must be a linear collider.

2.1.2 *The physics Looked for*

The study of high energy collisions is a way to probe the matter at very small scale according to the Heisenberg uncertainty principle: $\Delta p \Delta x \leq \frac{\hbar}{2}$ so $\Delta x \leq \frac{\hbar}{2\Delta p}$. That means that for a momentum transfer in the TeV range, it is possible to probe down to $10^{-19}m$ or one thousand millionth of an atom size !

The cross section of an interaction process measures the likelihood that it occurs.Cross sections typically decrease as $\frac{1}{E^2}$ above particle production thresholds (see figure 2.1).

The Standard Model of particle physics is a theory of three of the four fundamental interactions (electromagnetic, weak and strong interactions, but not gravitation) and the elementary particles that take part in these interactions. The particles involved in the Standard Model are the six quarks (up, down, charm, strange, top and bottom), the six leptons (electron, muon, tau and the corresponding neutrinos), the four bosons (photon, gluon, Z and W) and the Higgs particles (see figure 2.2). All of these particles has been observed except for the Higgs particles and their properties agree with the Standard model.

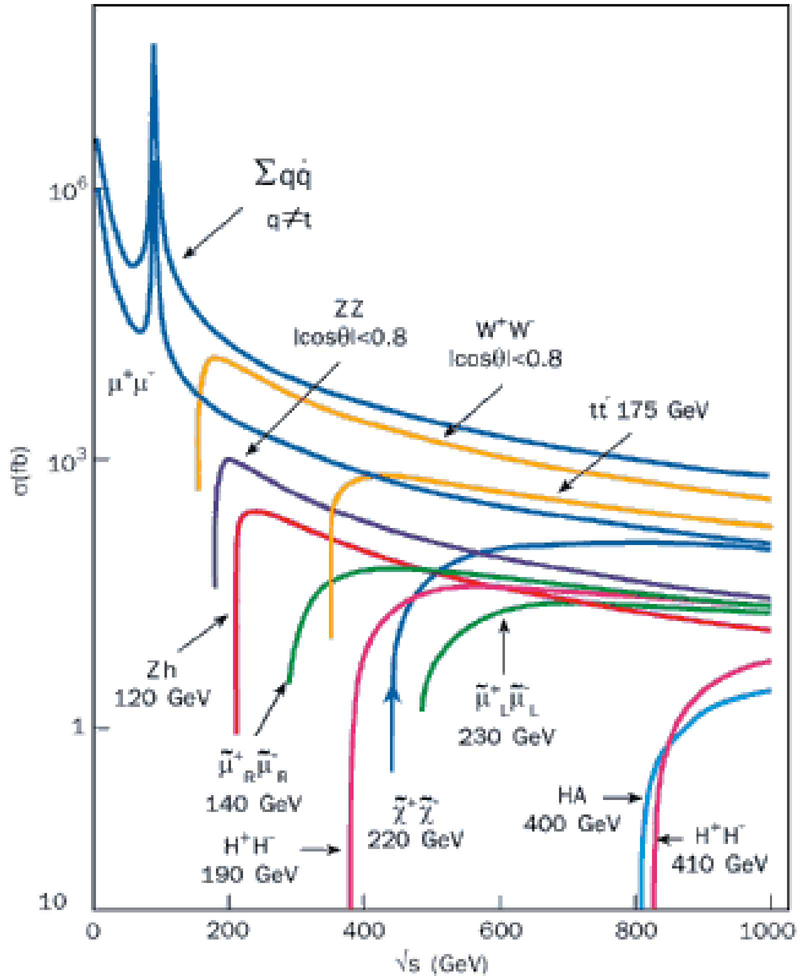

Figure 2.1: Cross section for possible states accessible at a linear collider. The horizontal axis is the energy that is available to make new particles in electron positron collisions. The vertical axis is the cross-section in femtobarns ($1fb = 10^{-24}m^2$). (Plot from the Japanese Linear Collider team).

At the high energies explored by the LHC and the future linear collider, the prediction of the cross sections can be checked as well as new process such as the Higgs creation. It is very important since the Higgs particle is an integral part of the process to explain the particles' masses in the Standard Model as well as in several extended models. One of this models: the SUperSYmmetry (SUSY) model, involves even more particles as shown in figure 2.2. Some of them could be discovered and studied at the LHC and the linear collider.

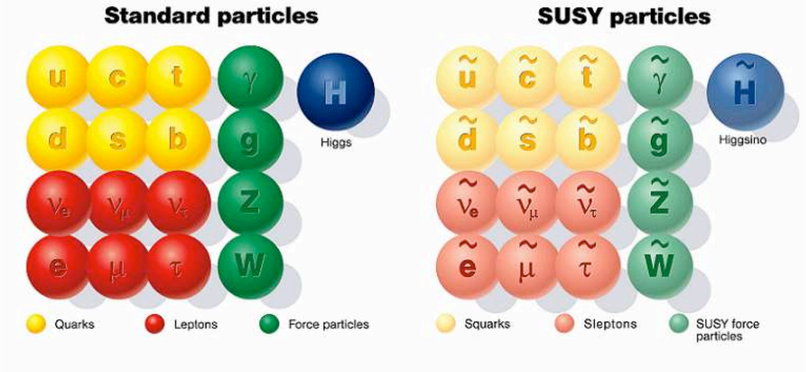

Figure 2.2: Standard Model and Supersymmetry "partners" particles.

2.2 Linear Collider designs

2.2.1 Specificities of Linear Colliders and Parameter Optimisation

In a circular accelerator, particles make hundreds of thousands of turns in the ring, unlike in a linear accelerator where they go through only once. So in order to have a large beam energy for a reasonable size, linear accelerators need a large number of very efficient accelerating cavities. The length of the collider is fixed by the choice of the accelerating technology and the center-of-mass energy required for the physics looked for.

The ILC collaboration chose a 1.3 GHz superconducting RF technology, with a gradient of $31.5 MV/m$. It is an ambitious goal, even if $50 MV/m$ has already been achieved [2], because it is needed to be obtained in a mass-production context (~ 17000 cavities for $2 \times 250GeV$). The corresponding linacs are then $2 \times 11km$ long[3].

The CLIC collaboration chose a 12GHz frequency with a two-beam concept where a "drive beam" is used to accelerate the colliding beam with a gradient of $100MV/m$. The feasibility (for instance the break-down rate) should be demonstrated soon. With such parameters, the entire size of CLIC will be $12km$ for $500GeV$ and $\sim 50km$ for $3TeV$.

In a circular collider, the bunches collide every turn, increasing the luminosity a lot. The luminosity is defined as the ratio between the event rate and the cross-section for a given event. It is proportional to the density in the overlap of the colliding bunches. In a linear accelerator, to obtain a comparable luminosity as in a circular accelerator, the beam size at the Interaction Point (IP) is made very small according to the expression of the luminosity $\mathcal{L}$ given in equation 2.1 function of the repetition frequency f_{rep} of the bunch trains, the charge of the colliding bunch population N_b, the number of bunches per train n_b, the horizontal and vertical beam sizes at the IP σ_x^* and σ_y^* and a factor H_D which describes an enhancement of the luminosity self focusing the beams during the collision.

$$\mathcal{L} = \frac{f_{rep} n_b N_b^2}{4\pi \sigma_x^* \sigma_y^*} H_D \tag{2.1}$$

Such a small beam size is not possible in a circular accelerator because the beams are totally disrupted after a collision and cannot be used any more unless new designs (such as crab-waist [4]) are used.

To obtain the design luminosity, it needs to take care of several constraints and effects:

- The repetition frequency f_{rep} of the trains and the number of bunches per train nb are defined by the accelerating technology. f_{rep} is also driven by the total power cost.

- The colliding bunch population N_b is mainly limited by wake-field effects kicking the bunches and increasing the effective beam size. That wake-fields are lower in ILC with its large cavities running at $1.3GHz$ than in CLIC with its narrow cavities running at $12GHz$.

- The transverse beam size is limited by the need to keep the Beamstrahlung (synchrotron radiation due to strong beam fields, see eq. 2.2 for the Beamstrahlung power emission function of the center-of-mass energy E) at the level of few $\%$ of the beam energy and to keep the possibility to correct for high order beam aberrations.

$$\delta_{BS} = 0.86 \frac{e r_e^3}{2 m_0 c^2} \frac{N_b^2 E}{\sigma_z (\sigma_x + \sigma_y)^2} \tag{2.2}$$

- The longitudinal beam size is limited by the hourglass effect : if the beam size is long compared to the longitudinal extent of the focal point, it will decrease the luminosity. The vertical beta function at the IP must be similar to the longitudinal beam size. Bunch compressors are used to reduce the longitudinal beam size, allowing a stronger focusing.

Maximizing the luminosity keeping the beamstrahlung at a reasonable low level impose to have a flat beam ($\sigma_x \gg \sigma_y$).

The emittance ϵ is quantifying the extent occupied by the beam particles in phase space as it travels (eq. 2.3 and section A.1 for further details). That emittance must be small to obtain small beam size.

$$\epsilon_x = \frac{< (x - < x >)^2 > < (x' - < x' >)^2 >}{< x x' >^2} \tag{2.3}$$

parameters	symbol	ILC ($500GeV$)	CLIC ($3TeV$)	ATF2 ($1.3GeV$)
bunch population	N_b	2.10^{10}	4.10^{9}	$1-2.10^{1}0$
number of bunches / train	n_b	2625	312	1(goal 1)$-$30(goal 2)
linac repetition rate	f_{rep}	$5Hz$	$50Hz$	$1.5Hz$
horizontal beam size at IP	σ_x^*	$640nm$	$45nm$	$3\mu m$
vertical beam size at IP	σ_y^*	$5.7nm$	$1nm$	$37nm$
bunch length	σ_z	$300\mu m$	$44\mu m$	$8mm$
horizontal emittance	$\gamma\epsilon_x$	$1000nm.rad$	$660nm.rad$	$5000nm.rad$
vertical emittance	$\gamma\epsilon_y$	$40nm.rad$	$20nm.rad$	$30nm.rad$
energy loss to beamstrahlung	δ_{BS}	2.4%	29%	non-relevant
peak luminosity	$\mathcal{L}_{pk}$	$2.10^{34}cm^2s^{-1}$	$6.10^{34}cm^2s^{-1}$	non-relevant

Table 2.1: Comparison of the parameters of ILC, CLIC and ATF2

All this constraints allow determining the parameters of ILC and CLIC (shown in the table 2.1).

2.2.2 Main Components

An e^+e^- linear collider contains an electron source to produce the initial beam, the electron beam is then accelerated a first time to suppress the non-relativistic repulsion of the electrons. Before being extracted in the main linac where the beam is accelerated to its nominal energy, it is injected to a damping ring to reduce its emittance and then it is focused in the final focus section where it collides with a positron beam. That positron beam has been produced from the electron beam and has been damped and focused as well. The global schemes of the ILC and CLIC are shown in figure 2.3 and figure 2.4, respectively.

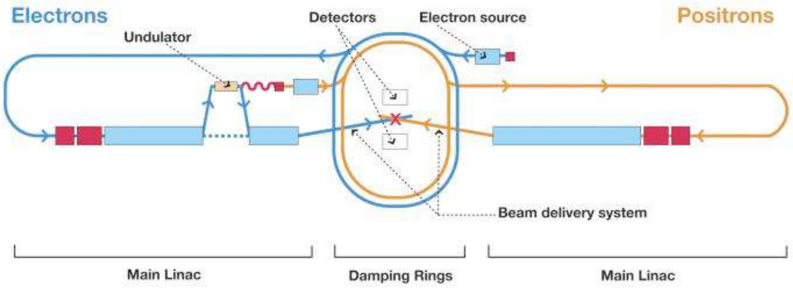

Figure 2.3: A schematic layout of the International Linear Collider.

Electron Source

The electron source is composed by a GaAs cathode hited by a nanosecond long high intensity laser pulse causing it to emit circular polarized electrons. these electrons are then accelerated to avoid increasing of the emittance due to the space charge of the beam and to reach the energy of the damping ring.

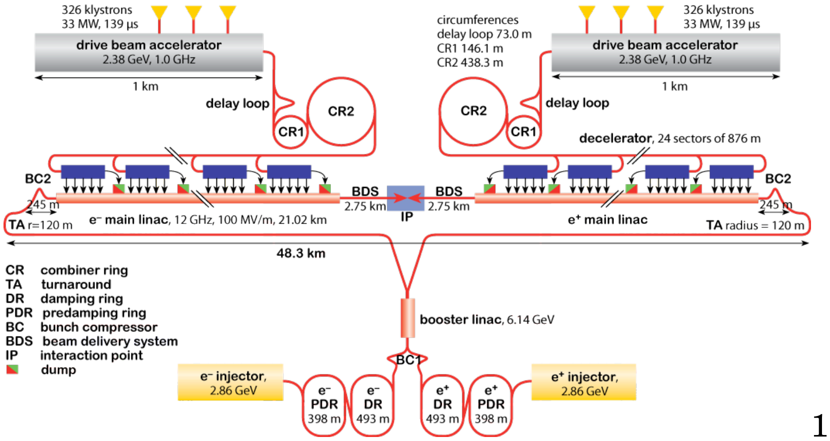

Figure 2.4: A schematic layout of the Compact LInear Collider.

During the acceleration, the beam is bunched by the Radio Frequency (RF) cavity to obtain the right time-structure and is accelerated to a few GeV ($5GeV$ for ILC and $\sim 3GeV$ for CLIC). A photo of the ATF photo-cathode RF gun is shown figure 2.5.

Figure 2.5: The ATF photo-cathode RF gun.

Positron Source

The scheme of the baseline positron source is displayed in figure 2.6. A part of the accelerated electrons goes through an undulator producing photons. These photons, when they go trough a target, will convert in e^+e^- pairs. Separated by a magnet, the positrons are then accelerated and injected into a damping ring to decrease their emittance. The target must rotate and be cooled to sustain the energy deposition. The principle of this scheme has already been successfully tested in the E166 experiment at SLAC [5].

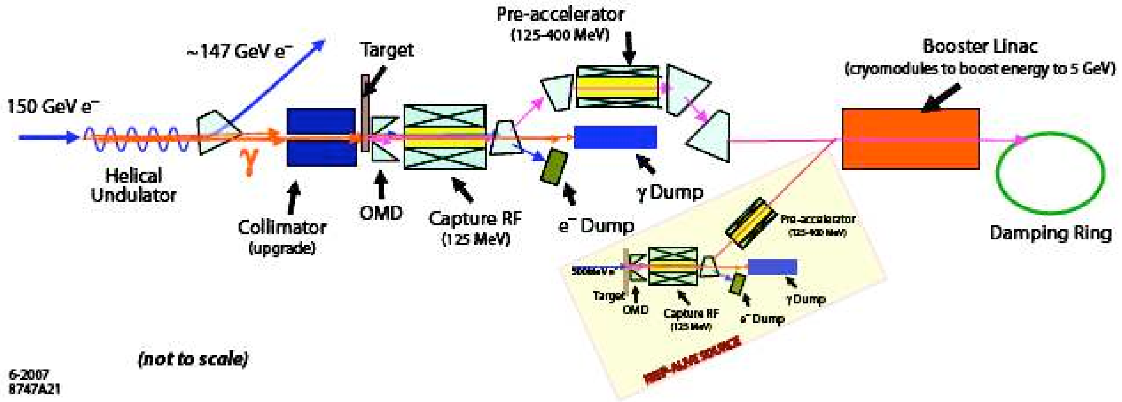

Figure 2.6: Baseline of the positron source scheme

An alternate solution that uses Compton scattering is shown figure 2.7. Instead of an undulator to produce the photons, a very high power laser interacting with the electrons in a ring is used. This scheme allows low energy electrons but imposes stacking of the positron bunches in the damping ring due to a low number of positrons produced within the acceptance of that ring ($\sim 1\%$ of the produced positrons).

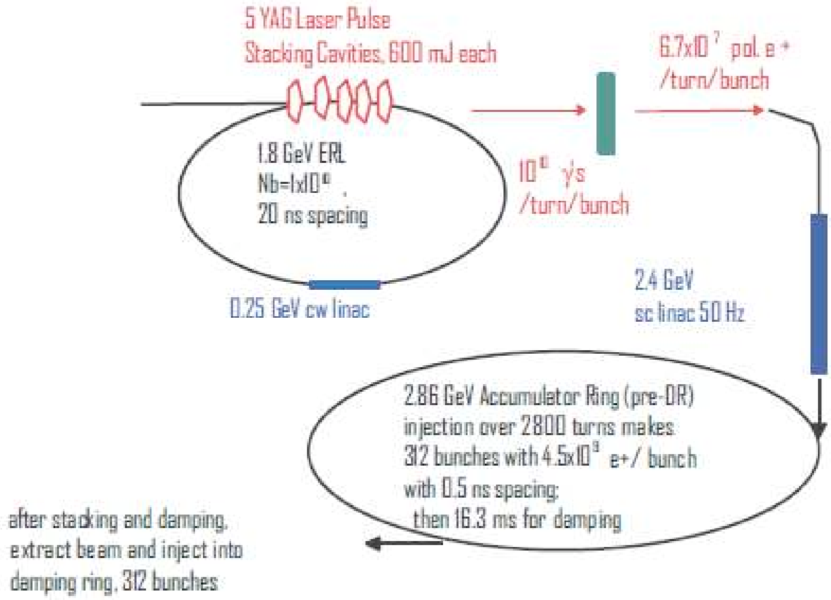

Figure 2.7: Laser Compton scattering scheme for the positron source

Damping Rings

To obtain the required emittances for the electrons and positrons, cooling of the phase space is needed. The cooling is obtained by using a damping ring, where the particles lose energy to synchrotron radiation according to their trajectory while they gain energy longitudinally in the ring cavity. The combined effect is a loss in transverse motion proportional to this initial motion, producing an exponential decrease of the emittance down to equilibrium.

This equilibrium emittance comes from:

- About the horizontal emittance: the synchrotron radiation is a quantum phenomena, so it happens randomly introducing energy loss in bending magnets where there is dispersion. That introduces horizontal oscillations not coherent between the electrons of the bunch, increasing the horizontal emittance. That emittance growth is proportional to the average of the Courant-Snyder dispersion invariant[6] : $\eta_x(s)^2\gamma_x + 2\eta_x(s)\eta'_x(s)\alpha_x + \eta'_x(s)^2\beta_x$ so damping rings are designed to have small dispersion in the arcs sections.

- About the vertical emittance: the synchrotron radiation is emitted with an angle $\sim \frac{1}{\gamma}$, so the equilibrium emittance is non-zero. However, this effect is usually much smaller than the emittance introduced by the coupling with horizontal motion and the dispersion caused by the misalignments of the magnets.

The emittance required for linear colliders has already been obtained in the ATF damping ring.

The Main Linac

Once the electron and positron beams have been produced and cooled, they must be accelerated to high energy. This is achieved thanks to a large number of cavities along the main linac. These cavities provide Radio Frequency (RF) fields such that during the passage of the beam through them, they see an accelerating electric field.

A particle coming in with a lower energy than the reference one will arrive later, so a larger field must be applied to make up for its missing energy. This means the bunches should arrive during the rise time of the field.

ILC uses conventional klystrons and superconducting cavities (see fig. 2.8) whereas CLIC uses the deceleration of a high intensity beam to produce the RF for the main linac.

Position feedbacks are implemented to center the beams in the cavities, to limit the emittance growth due to wake-fields.

At the beginning of that section is also implemented the bunch compression: cavities are used to introduce a correlation between the longitudinal positions

Figure 2.8: A cell of 9 ILC prototype superconducting cavities.

of the particles in the bunch and their energies. The first particles receive less energy than the last ones, such that thanks to a chicane where the higher energy particles have a shorter trajectory, longitudinal position differences downstream reduce bunch length (see figure 2.9).

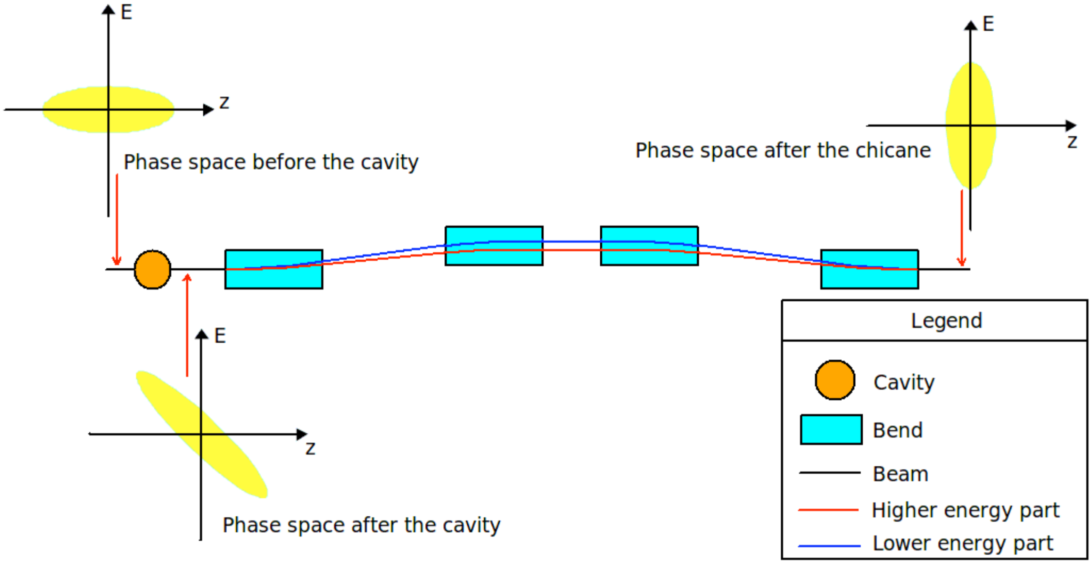

Figure 2.9: Principle of a bunch compressor.

2.2.3 The Beam Delivery System

After the acceleration, in the Beam Delivery System (BDS) the beam needs to be focused and higher order aberrations must be compensated to obtain a nanometer transverse beam size. The chromaticity, ξ, which quantities the error on the focusing due to the energy spread of the beam, is the main source of aberration at the IP. Its formula is given in equation 2.4 [7] with k the quadrupoles strength, m the sextupole strength and D_x the horizontal dispersion.

$$\xi = \frac{1}{4\pi}\int \left(k(s) + m(s)D_x(s)\right)\beta(s)\mathrm{d}s \tag{2.4}$$

As the β functions and the strengths K of the quadrupoles are much larger in the final doublet (FD) than anywhere else, the chromaticity introduced by the quadrupoles can be approximated as $\xi = \frac{L^*}{\beta^*}$ where β^* is the value of the beta function at the IP and L^* is the distance between the last quadrupole and the IP. As that chromaticity must be corrected using sextupoles, which introduces non-linearities, the chromaticity can be saw as a measure of the difficulty to design and tune the BDS. Keeping the same chromaticity (and so the same level of the difficulty in the design of the BDS and its tuning), it is possible to reduce β^* if L^* is reduced by the same amount.

However reducing L^* means increasing the strength of the final doublet which eventually leads to technological limits, especially at high energy. Also, in a collider very large detectors are placed around the IP and they need enough spaces to operate in good conditions. Also, as the longitudinal beam size σ_z must be comparable to the vertical beam size to avoid the hourglass effect, it implies to reduce further σ_z.

In the BDS, the beam from the main linac must be adapted to correct for the trajectory and focusing errors in the other parts of the accelerator. The alignment of the magnets, their stabilization and beam position feedback must be used to control emittance growth. An efficient collimation system must also be included to remove the beam halo which would otherwise generate large background in the detector at IP. ATF2 is a low energy prototype of one side of the linear collider BDS. A more precise description will be given in section 3.2.

Chapter 3

THE ATF2 PROJECT

An important challenge for the ILC is the collision of nanometer size beams, which requires the creation of a small emittance beam, conserved during the acceleration and the transport, and final focusing. As ATF has shown the ability to create emittances close to those required for ILC [8][9], an extension called ATF2 has been decided to test the focusing to nanometer beams. ATF2 will continue the work achieved by the Final Focus Test Beam (FFTB) at SLAC [10]. The ILC Beam Delivery System has also changed significantly (notably the chromaticity correction section) and a number of important issues could not be addressed at FFTB[11].

3.1 Project Description

3.1.1 Overview of ATF Project

The Accelerator Test Facility (ATF) is composed of an electron-gun, a $1.3 GeV$ electron linac and a 1.3 GeV damping ring. Before ATF2 construction, the beam was extracted in a short extraction line where the extracted beam emittance could be measure in a diagnostic section. The layout of ATF before ATF2 construction is shown in figure 3.1.

The beam operation began in 1997 and beam emittances produced by ATF were among the lowest for the same type of rings. The main parameters are presented in table 3.1.

ATF is also used to develop instrumentation:

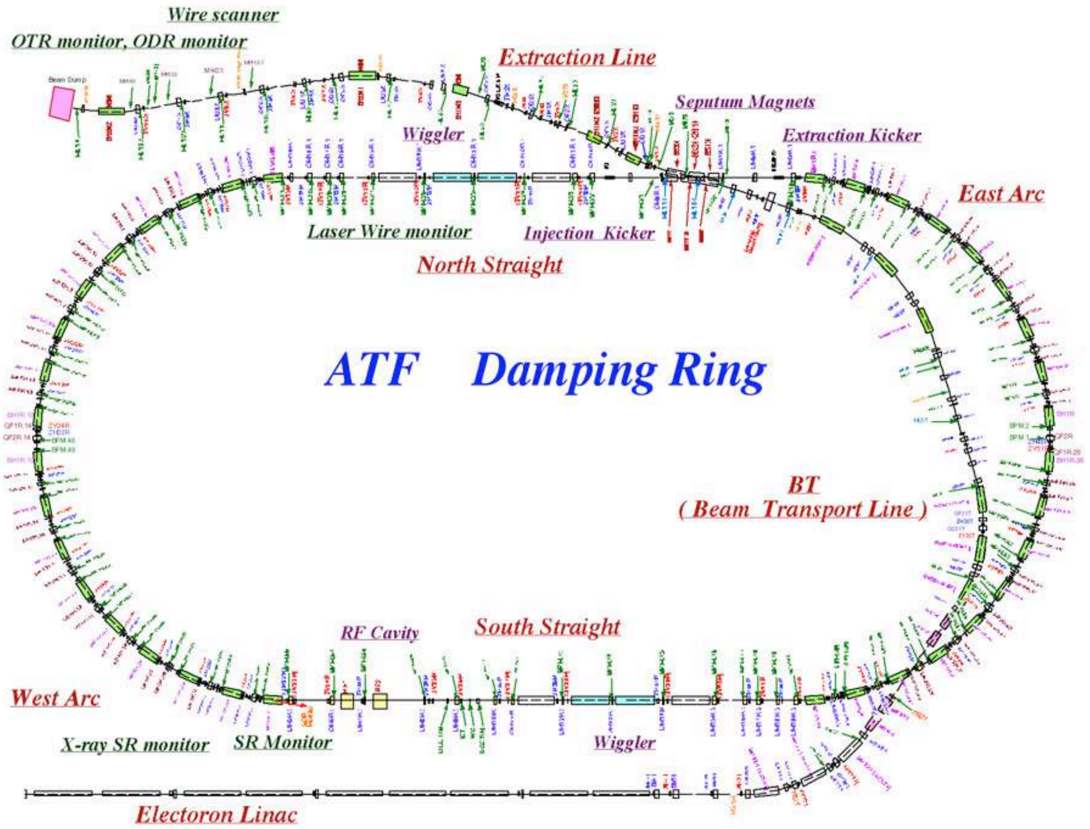

Figure 3.1: Layout of ATF before ATF2 construction.

Beam energy	$1.28 GeV$
Beam intensity single bunch operation multi bunch operation	$1.0 \times 10^{10} e^-/bunch$ $0.7 \times 10^{10} e^-/bunch \times 20 bunch$
Beam repetition	$0.7 \rightarrow 6.4 Hz$
X emittance (extrapolated to 0 intensity)[8]	$1.0 \times 10^{-9} rad.m$
Y emittance (extrapolated to 0 intensity)[8]	$1.0 \times 10^{-11} rad.m$

Table 3.1: Major ATF performances.

- Fast and high-resolution beam position monitors for the damping ring orbit
- Cavity BPMs
- High resolution beam size monitor as:
    - Laser wire monitors.
    - Synchrotron radiation interference beam size monitor
    - X-ray synchrotron radiation beam size monitor
    - Optical Transition Radiation beam size monitor (OTR)
    - Synchrotron radiation bunch length monitor

3.1.2 Goals of ATF2

The ATF2 facility [12][13] (see figure 3.2) was built to address two major challenges of ILC: focusing the beams to nanometer scale using an ILC-like final focus and controlling the beam position.

That first goal consists in achieving and maintaining a $37nm$ vertical beam size in a reproducible way, demonstrating in this way the compact final focus system based on local chromaticity correction. The ATF2 final focus section has been designed scaling down in energy the ILC design while keeping the chromaticity to a similar level ($\sim 1 \times 10^4$). This leads to the $37nm$ vertical beam size value.

The second goal consists in demonstrating the stabilization of the beam train trajectory at the nanometer level at the IP using ILC-like multi-bunch train structure. It will be realized thanks to the a Feedback On Nanosecond Timescales (FONT) system [14].

The achievement of the first goal has been initially planned for 2010 and the second one for 2012.

Ultimately the aim will be to achieve the two goals simultaneously to prove the linear collider beam delivery system feasibility while learning and training with the techniques and procedures involved.

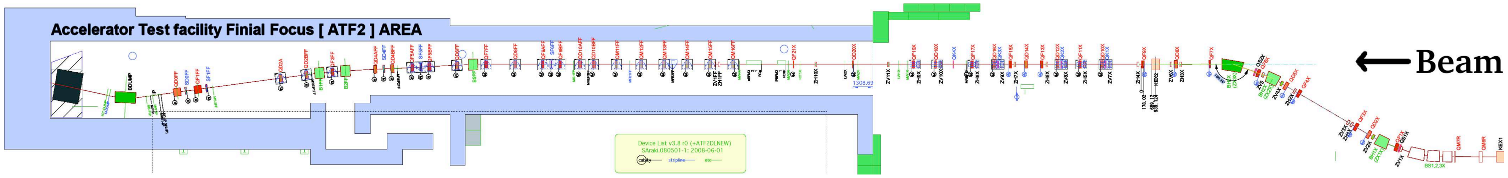

Figure 3.2: ATF2 beam line.

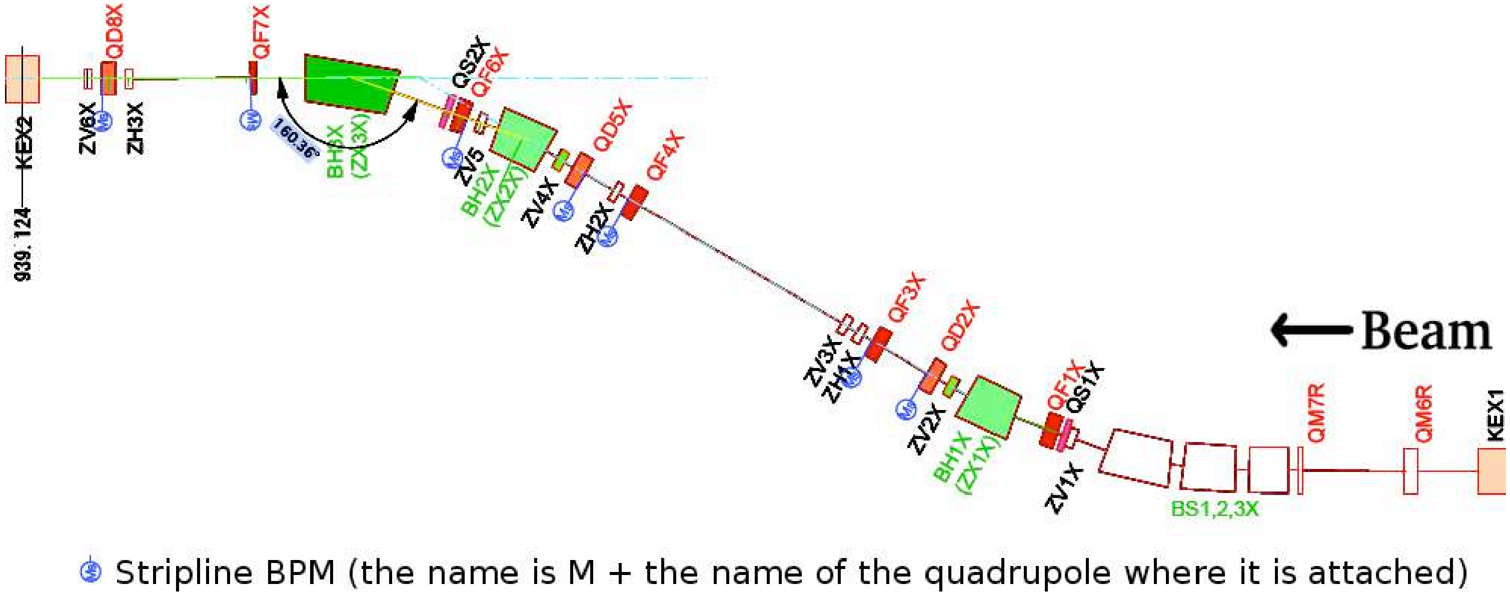

Figure 3.3: Layout of the extraction inflector.

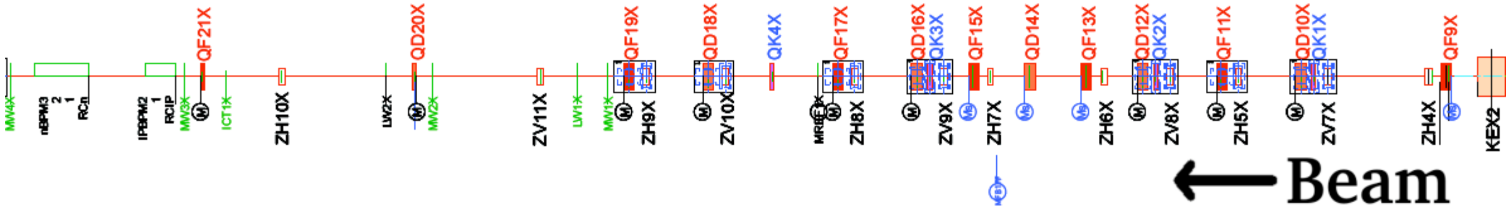

Figure 3.4: Layout of the extraction diagnostic section.

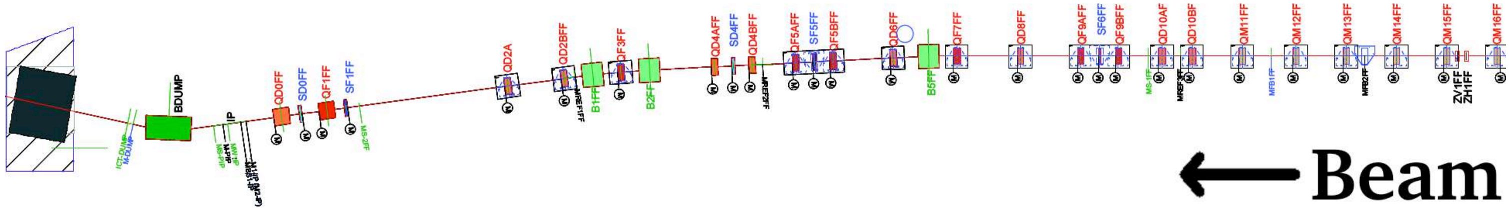

Figure 3.5: Layout of the final focus section.

3.1.3 Planning of the Commissioning

The commissioning has been planned to satisfy the first goal at the end of 2010 and the second later on, it means that during the first years of the commissioning, the understanding of the optics was the priority, including exercising the optics correction methods and the development of the instrumentation associated to these corrections. Other aspects have been developed like the ATF ring tuning, general instrumentation development and stabilization implementation, even if they had a lower priority.

As the large magnification needed to focus the beam to nanometer beam size makes the tuning very sensitive, it was decided to use different optics during the commissioning. We started with large beam sizes at IP (small magnification), and only later switched to a lower IP beam size when we considered we understood the optics enough. This way allowed solving the issues of such a strong focusing step by step.

3.2 Optics

3.2.1 The Different Sections

Extraction Inflector

The first part of the ATF2 beam line is the extraction inflector. Its optical functions are shown in figure 3.3. It has been designed to allow beam extraction while canceling the spatial and angular dispersion. It also permits the horizontal and vertical dispersion corrections (see figure 3.6).

As the kicker was already known to have jitter issues, a double kicker system was designed for mitigation of the effect. The first kicker introduces the kick needed to extract the beam. It is transported to the second kicker in a way such that the angle introduced by the first kicker becomes a pure opposite

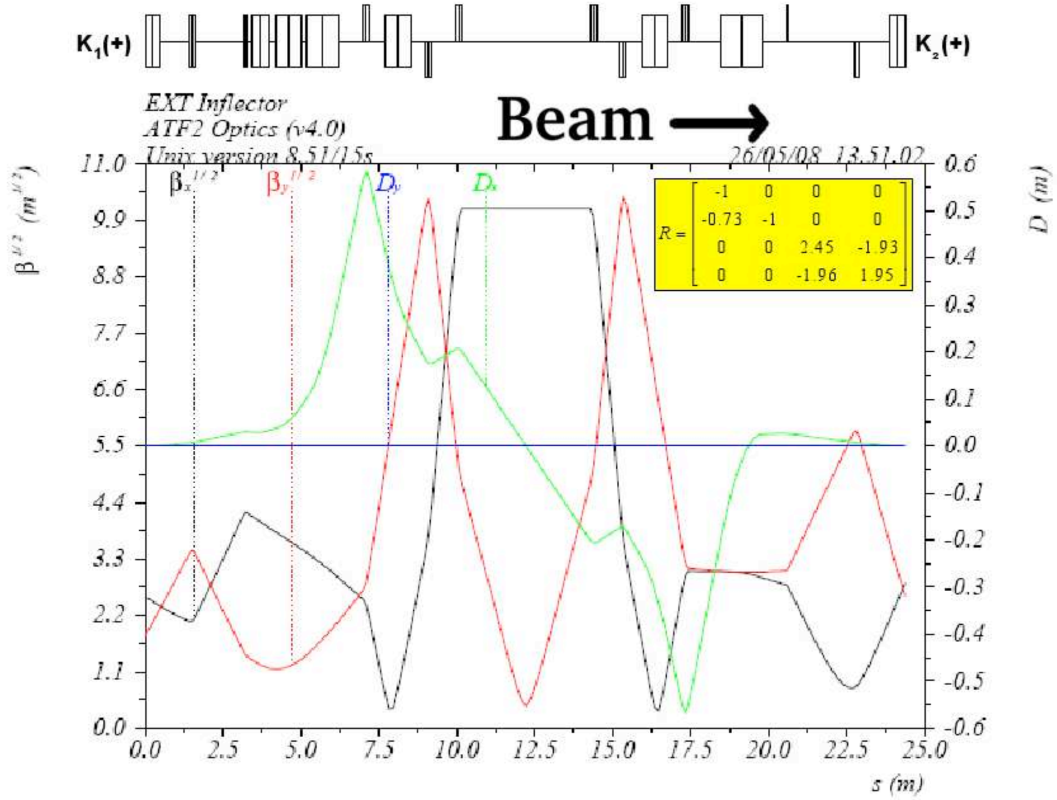

Figure 3.6: Twiss parameters of the extraction inflector with the transfer matrix between the two kickers.

angle at the second one ($R_{21} = 0$ and $R_{22} = -1$). As both kickers share the same power supply (with a delay corresponding to the time of flight of the beam), the same fluctuation is introduced by both kickers, the second canceling the fluctuation introduced by the first one.

Extraction Diagnostic Section

After the extraction inflector, the diagnostic section is used for measuring the emittance and correcting cross-plane betatron residual coupling. This section has been designed to be as close as possible to the ideal skew correction section as described in [15] (see figure 3.4 and 3.7).

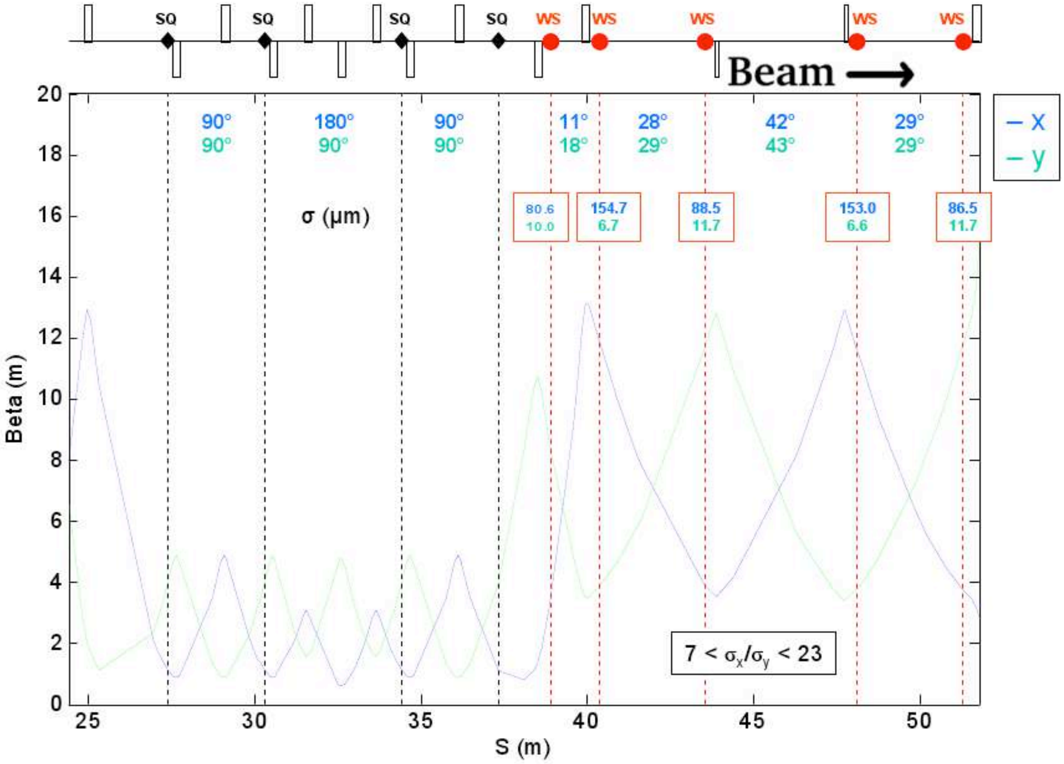

Figure 3.7: Twiss parameters of the extraction diagnostic section with the phase advances between skew quadrupoles (SQ) and wire scanners (WS).

Final Focus

The final focus (see figure 3.5) provides the focusing of the beam and compensates the chromaticity as explained in the next section. The final focus is equivalent to a telescope, but as quadrupoles focuses in one plane and defocuses in the other, at least two quadrupoles are needed to obtain the equivalent of an optics lens. The final doublet (QF1FF and QD0FF quadrupoles) enable the focusing of the beam to a small spot at the IP. Since the geometry is fixed, any adjustments of the overall magnification must be introduced upstream of the FFS, using six quadrupoles in the so-called matching section (QM16FF to QM11FF). These quadrupoles are also used to allow the matching of the beam that comes from the extraction section in the presence of focusing errors. The Twiss parameters of the final focus are presented in figure 3.8.

Unlike the extraction line, where corrector magnets are present to steer the beam, no correctors are available in that section. Instead, magnets are supported on mechanical movers allowing horizontal and vertical displacements as well as roll. That is mainly because the variations in beam trajectory from upstream are measured and corrected at the injection of the final focus section and what remains comes from displacements of the magnets induced by ground motion. In that case, it makes more sense to correct these displacements with movers than steering the beam. The movers can moreover serve to calibrate the cavity BPMs attached to each magnets.

3.2.2 The Local Chromaticity Correction

As the beam contains particles with a finite spread in their energy distribution and because particles with different energies are focused to different points along the beam line, chromatic aberrations in the final spot are present.

The initial design for the chromaticity correction took place upstream of the

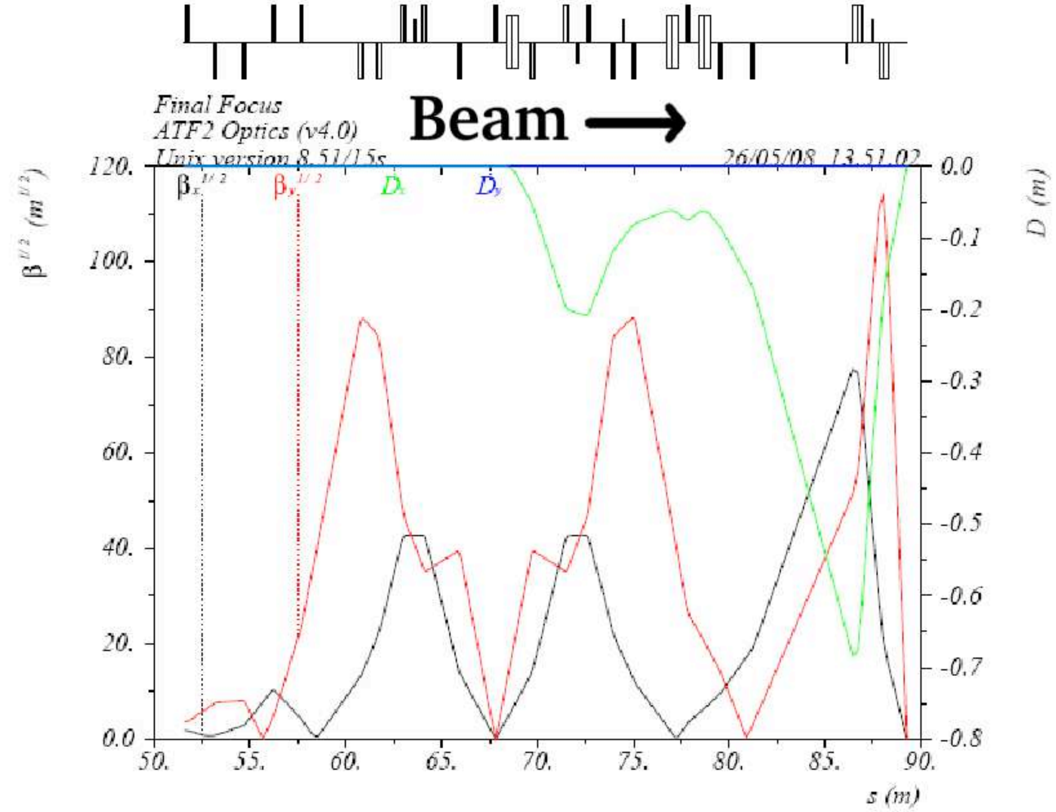

Figure 3.8: Twiss parameters of the final focus section.

final doublet where most of it is generated (non-local correction). It is based on sextupoles which produce a focusing proportional to the distance from their center. When located in a dispersive region (created by bending magnets), the additional focusing become thus proportional to the energy. This has been used to correct chromaticity. As the sextupole introduces geometric aberrations, a second sextupole with a minus identity transfer matrix (see section A.2) to the first one is added for cancellation. Due to the fact the dispersion function has the same values in both sextupoles, the chromaticity correction is doubled. That principle is used twice to correct for chromaticity in both plane as shown in the figure 3.9.

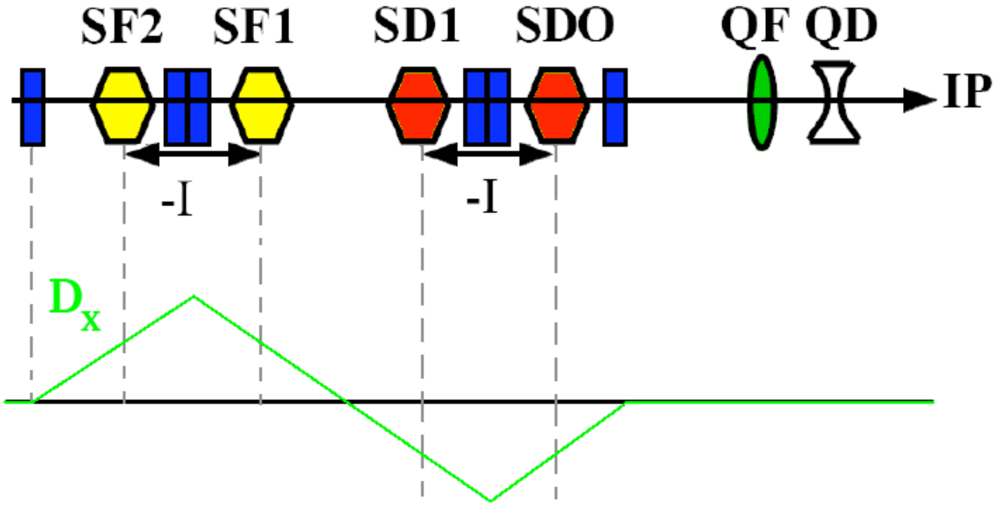

Figure 3.9: Scheme of the non-local chromaticity correction scheme.

This chromaticity correction has several limitations due to the fact that it is non-local, making this scheme very sensitive to errors in quadrupoles strengths and to the beam energy variation. A local chromaticity correction has been designed with improved properties[16] such as being much shorter and with lower 3rd order therms than the non-local correction. In that new scheme, two sextupoles interleaved with the final doublet quadrupoles and a bend upstream to generate dispersion are used to cancel the chromaticity locally. Two more sextupole upstream are required to cancel the geometric aberrations. That scheme is shown figure 3.10.

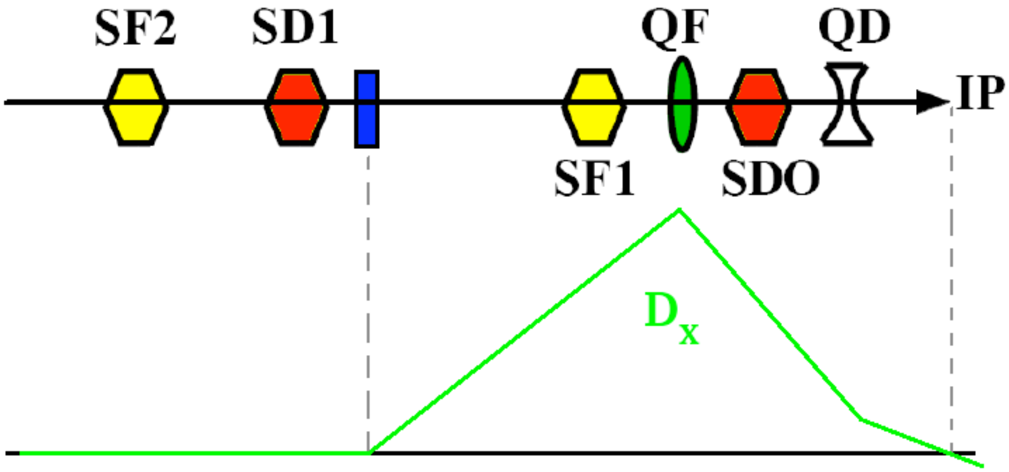

Figure 3.10: Scheme of the local chromaticity correction

The horizontal kick x' received from a quadrupole of strength K in a dispersive region (where $x = x_0 + D_x\delta$) by a particle with a δ energy variation, it can approximated as:

$$x' = K(x_0 + D_x\delta) - Kx_0\delta - KD_x\delta^2$$

The first term corresponds to the focusing of the beam, the second is the chromaticity term and the third one is the second order dispersion term.

The horizontal kick from a focusing sextupole of strength m in a dispersive region can be written:

$$x' = m[\frac{1}{2}(x^2 - y^2) + x_0D_x\delta + \frac{1}{2}D_x^2\delta^2]$$

The first term corresponds to the geometric aberration, the second one to the chromaticity and the last one to the second order dispersion. Setting the sextupole strength to $m = \frac{K}{D_x}$ corrects for the chromaticity but just for half of the second order dispersion. To correct completely for the second order, a second focal point is introduced in a non dispersive region (see figure 3.8) doubling the overall chromaticity and hence the sextupoles strength required to correct it.

The local chromaticity is shorter than the non-local one (making its realization cheaper) and is less sensitive to the beam energy variation and to the fields errors as the non linear term introduced by the sextupoles are transported on a much shorter distance.

In the ATF2 final focus a fifth sextupole and an additional bend have been used to decrease the chromaticity through the system and aberrations at the IP [16].

3.2.3 Tolerances

As a displaced quadrupole kicks the beam proportionally to its strength, displacement errors will steer the beam along the line and also, as a displaced beam in a sextupole introduces focusing, it has an effect on the beam size. The sensitivity of the beam position at the IP for all the final focus magnets has been simulated for a one micron displacement. It is shown in figure 3.11.

The sensitivity of displacements on the beam size has also been simulated, and results for one micron magnet displacements in the final focus are shown figure 3.12.

The tolerance on magnets displacements, rolls and strength errors have been simulated in a similar way for the proposal of ATF2[13], with a 2% increase in beam size as criterion. The figures 3.13, 3.14 and 3.15 show these results compared with the ones for the ILC. As one can see, the pattern in the sensitivities are very similar illustrating the near identity in the two optical

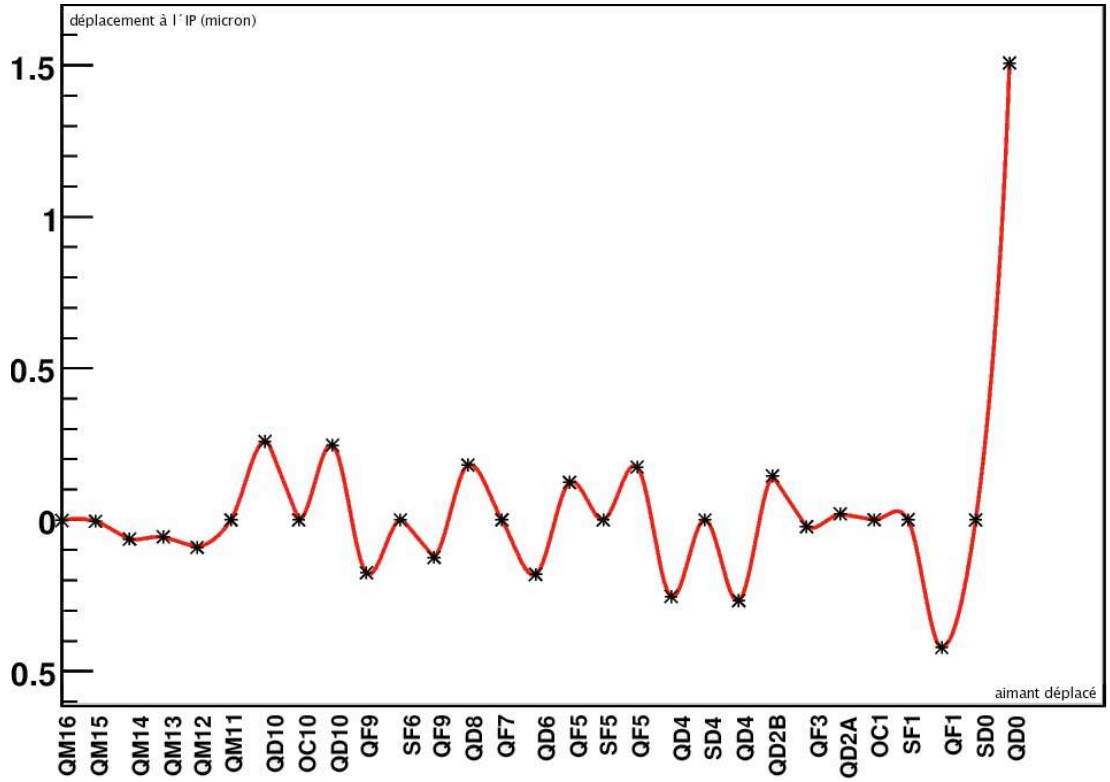

Figure 3.11: Vertical displacement (in microns) of the beam at the IP for a one micron displacement of each magnet, applied one at the time.

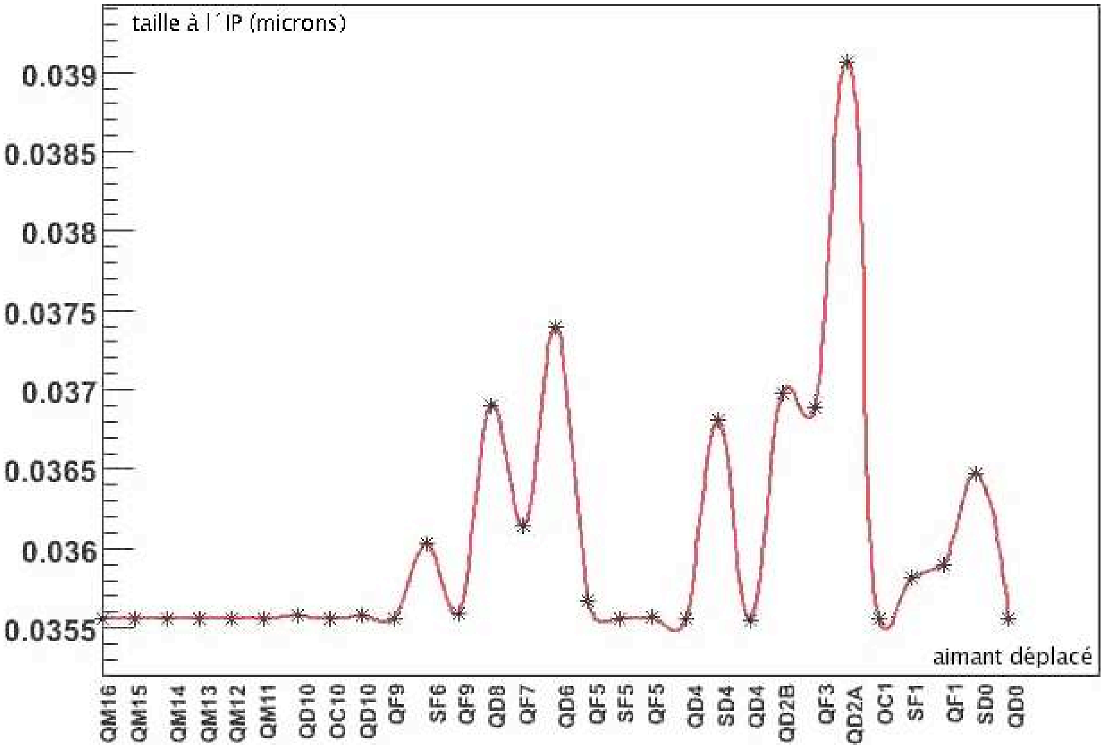

Figure 3.12: Vertical beam size (in microns) at the IP for a one micron displacement of each magnet, applied one at the time.

designs. Also comparing the figures 3.12 and 3.13, we see the results are compatible, with strict tolerances on the positions of QD8FF, QD6FF and SD4FF due to the relative beam displacement induced in the strong sextupole SD4FF, as well as QD2BFF, QF3FF, QD2AFF and SD0FF, due to the displacement induced in SD0FF (see section 9.1.1 to see why a displacement in a sextupole affects the beam size).

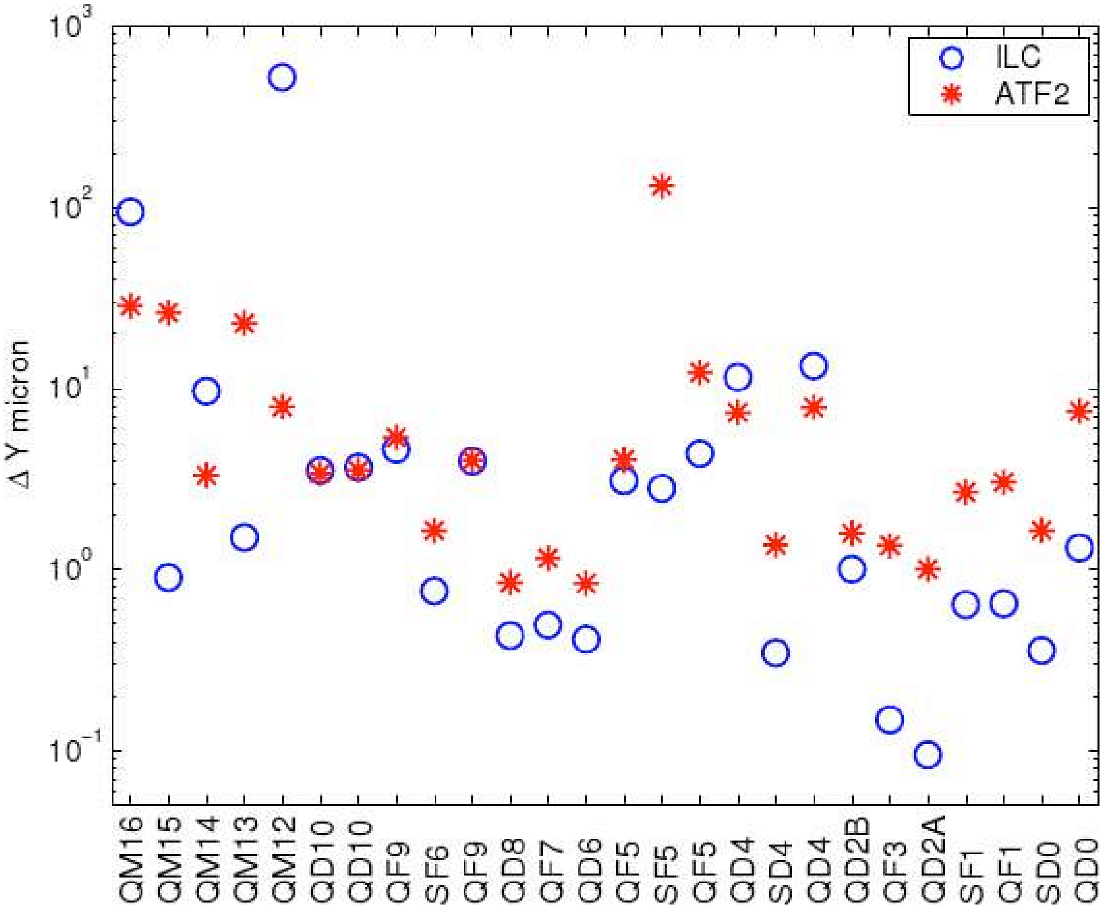

Figure 3.13: Vertical displacement of the indicated magnet giving a 2% increase of the beam size in ATF2 and ILC.

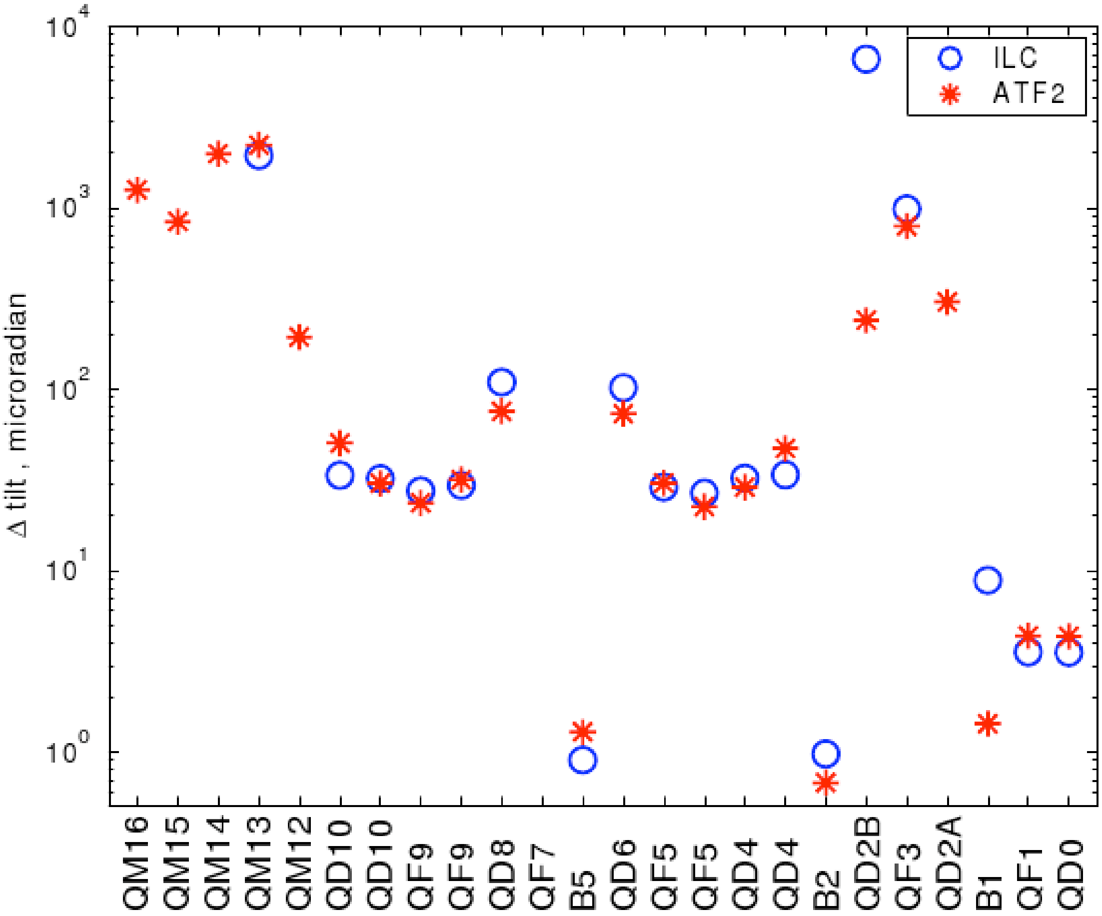

Figure 3.14: Roll of the indicated magnet giving a 2% increase of the beam size in ATF2 and ILC.

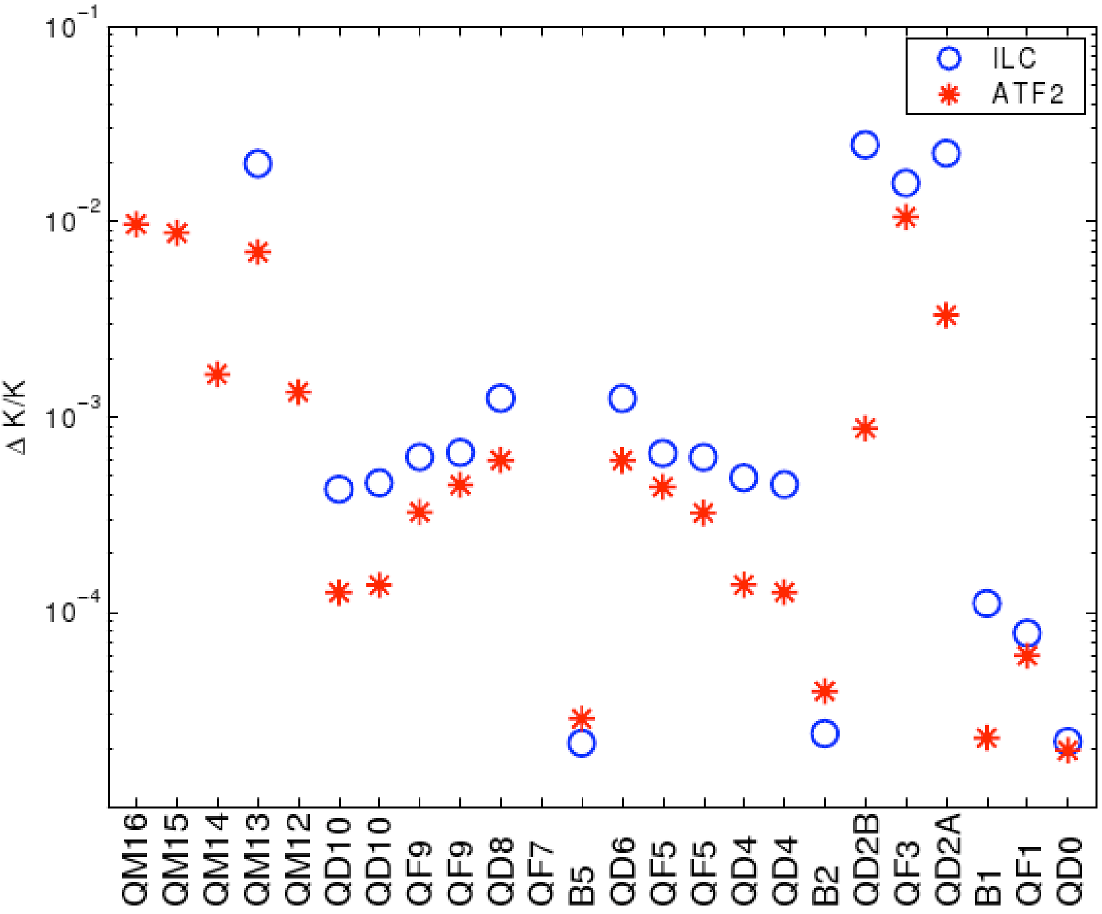

Figure 3.15: Field error of the indicated magnet giving a 2% increase of the beam size in ATF2 and ILC.

Chapter 4

THE INSTRUMENTATION AT ATF2

4.1 Beam Position and Tilt Monitors

4.1.1 Stripline BPMs

The stripline BPMs are in the extraction line of ATF2 and are detailed in section 5.1. Stripline BPMs have four electrodes to probe beam image current (see figure 5.3).

The current induced by an electrode is inversely proportional to the distance of the beam so, the difference in charge between two opposite electrodes is to first order proportional to the beam positions respect to the center of the stripline BPM.

The expected resolution of these BPMs is about $10\mu m$. A more detailed description is given in chapter 5.

4.1.2 Cavity BPMs

There are two types of cavity BPMs in ATF2: the C-band [17] (with a resonant frequency of $6.4GHz$) and the larger aperture S-band [18] ($2.9GHz$). Both shares the same principle and they are attached to quadrupoles and sextupoles in the extraction line and in the final focus.

Each cavity BPM is composed by a sensor pill-box shaped cavity and four waveguides. The cavity and the waveguides are connected by slots placed on the end plate of the cavity (see figure 4.1).

When the beam goes through the cavity with an offset, the TM_{110} mode, also

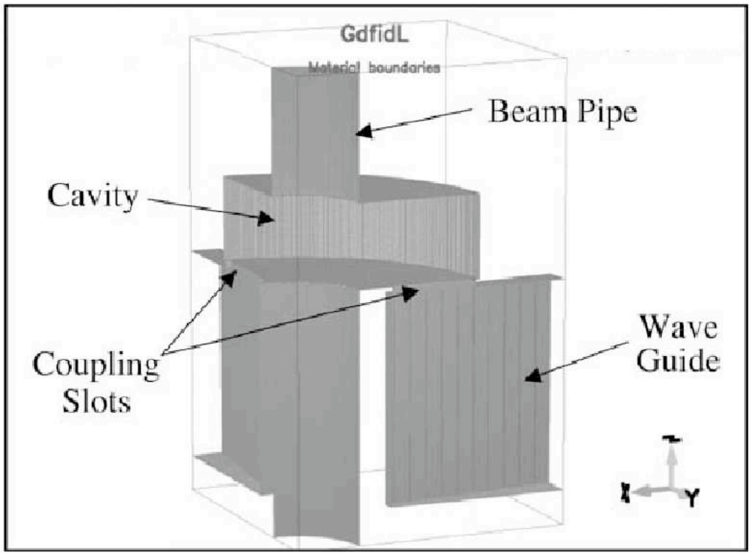

Figure 4.1: Quarter view of the inside surface of a cavity BPM.

called dipole mode, is excited proportionally to the offset [19]. That dipole mode signal in the sensor cavity is selectively fed out to the waveguides through slots via magnetic coupling (see figure 4.2). Then antennas on the waveguides pick the signal up into coaxial cables.

The signals of the waveguides are added with 180^0 relative phases to subtract residual common mode. The signals are then mixed down to $\simeq 20MHz$ and filtered to further remove the influence of the other TM modes before being digitized. The amplitude of the resulting signal is measured with careful attention to the saturation and decay.

To infer the beam position from the signal amplitude, the cavity has to be calibrated. The calibration is achieved by moving the cavity by a known amount using the mover and measuring the amplitude variation, or by introducing a trajectory bump for the cavities installed in magnets not on a mover.

The S-band cavity BPMs (see figure 4.3) are used in the final doublet due to the large apertures ($40mm$) needed in the corresponding magnets for beam

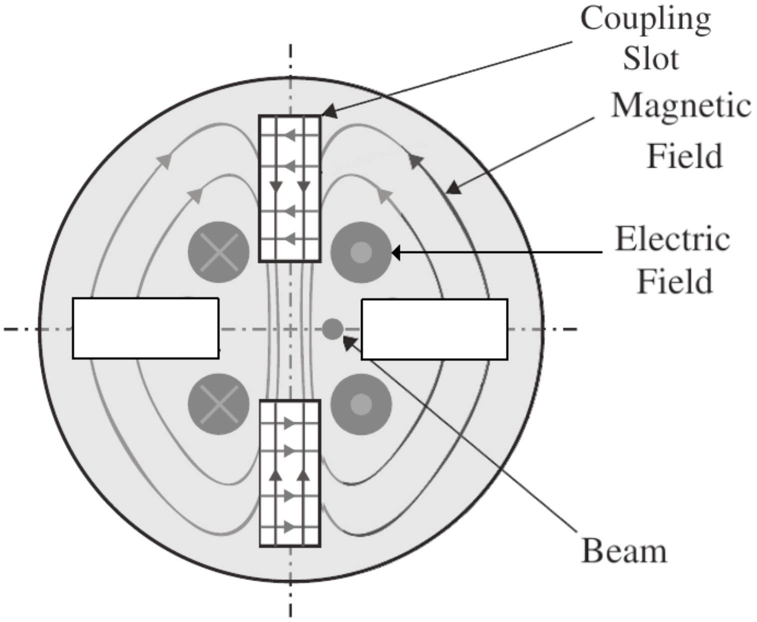

Figure 4.2: Fields of the TM_{110} mode, also called dipole mode. That mode is selectively coupled out by means of four long, narrow and radial slots. In the case of a horizontal offset of the beam, only the vertical slots induce signal in the wave-guides.

clearance and to avoid background creation by the halo hitting the vacuum chamber in that very high beta section.

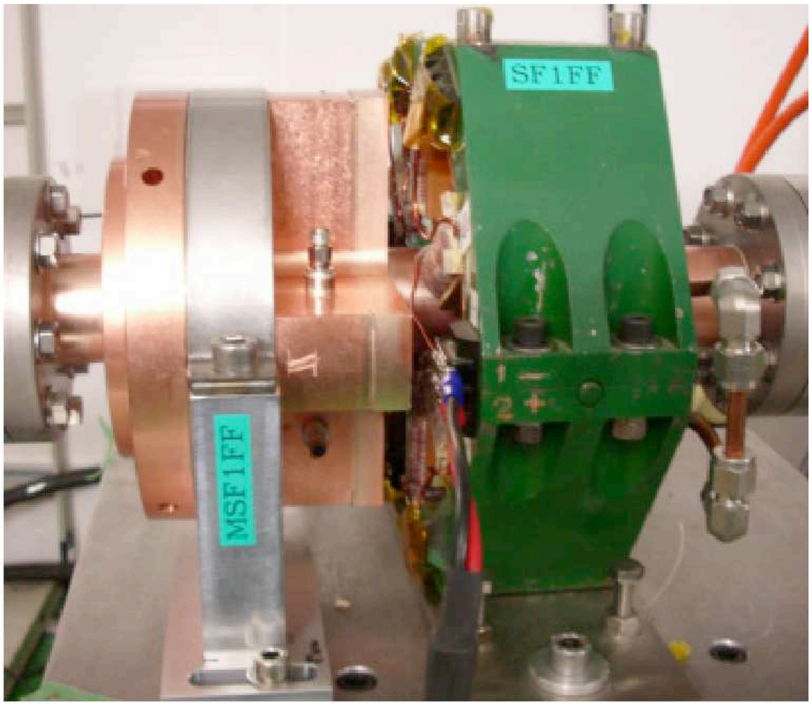

Figure 4.3: The MSF1FF S-band cavity BPM and SF1FF sextupole in assembly in the ATF2 final focus.

To avoid saturation, $20dB$ atenuators have been installed, increasing the dynamic range of the cavity from $500\mu m$ to several mm while also degrading the resolution (about $1\mu m$ instead of $30nm$).

4.1.3 Interaction Point BPM

To measure the beam jitter at IP, it is planned to install two special cavities between the final doublet and the IP. To achieve this measurement, the cavities must have a few nanometer resolutions. They have been specially designed to measure independently beam positions in X and Y directions and to have low angle sensitivity [20].

The cavityies are rectangular, with different lengths in X and Y to separate the X and Y TM_{110} modes by about $1GHz$ and allow separation of the horizontal and vertical signals.

The length of the cavity in the longitudinal direction is small ($6mm$) to reduce the influence of the large angle jitter in that section.

As it is necessary to have at least two BPMs to determine the trajectory, two IPBPMs will be grouped in one block (see figure 4.4).

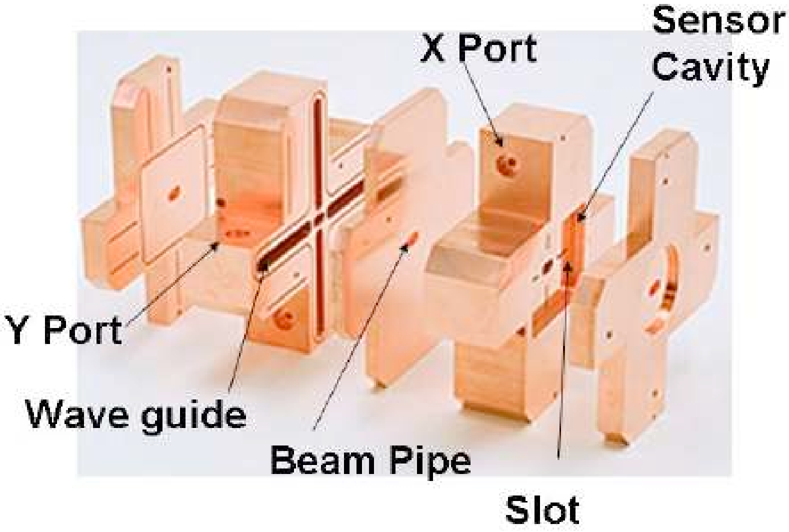

Figure 4.4: The block of 2 IPBPMs structure.

4.1.4 *Tilt Monitor*

IPBPMs will provide precise information about the position of the beam before the IP, but concerns about the angular reconstruction in the presence of systematics in the two cavities led to the design of an instrument directly measuring the horizontal and vertical angle of the beam: the tilt monitor [21].

The tilt monitor uses the monopole mode which is proportional to the tilt of the beam. Once again, the cavity is rectangular to separate the horizontal and vertical measurements and the monopole modes are selected by the waveguides. A scheme of that monitor is shown in figure 4.5.

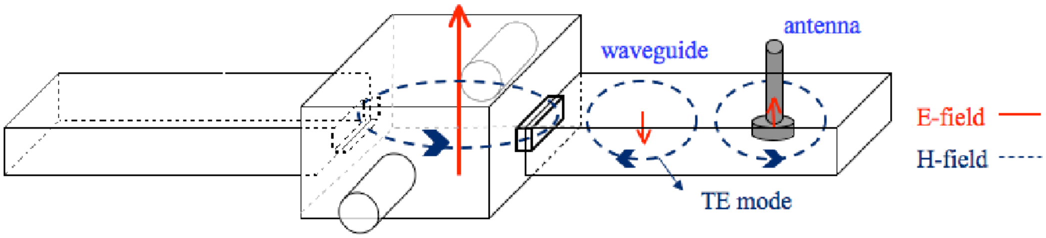

Figure 4.5: Scheme of the tilt monitor.

That monitor, after completing experimental tests in the extraction line, will be installed between the final doublet and the IP, giving complementary results to the IPBPMs. The resolution is about the same as the one expected from combinating two IPBPMs in the absence of errors ($30nrad$).

4.2 Beam Size Measurement

4.2.1 Wire-Scanners

To measure the beam size with a wire scanner, the wire is moved across the beam generating bremsstrahlung gamma rays detected downstream. To estimate the number of the photons created, we divide the beam in several slices. The number of photons $d\phi$ created per each slice is proportional to the total charge dq in the slice and to the length l crossed by that slice through the wire.

The profile is the measurement of the number of photons created ϕ, as function of the wire position y. That profile corresponds to the convolution of the charge and the longitudinal length of the wire:

$$\phi(y) = \int q(x) \times l(y-x)\mathrm{d}x = (q * l)(y)$$

As the wire is a cylinder, it is possible to find the beam size by deconvolution of the photon flux function of the wire position. The resolution of a wire scanner measurement with a wire of diameter D is about $\frac{D}{4}$[22].

There are five wire-scanners in the diagnostic section of the ATF2 extraction line. These wire-scanners move according to a 45^0 angle in the XY plane. Each wire scanner has 3 tungsten wires with different angles (90^0, 45^0 and 0^0 respectively from the horizontal direction) allowing beam size measurements respectively on Y, U (45^0) and X plane [23] (see figure 4.6). The diameter of these wires are $10\mu m$ so the resolution is about $3\mu m$. Once the collision point of the beam with the wire is found, then the scan can take from $30s$ to few min (depending on the number of measurements taken during the scan).

4.2.2 Optical Transition Radiation Monitor

As beam size measurements with wire-scanners are quite a long process and the estimation of the emittance needs a lot of such measurements, an additional instrument has been proposed: the Optical Transition Radiation (OTR) monitor.

The OTR monitor is made of a conductive foil: when the relativistic beam goes through, transition radiation is emitted with an angle equal to the angles made by the incoming particles and the generated light is collected by a microscope and acquired with a CCD camera (see figure 4.7). The system is designed for single bunch beam size measurements with a resolution of few microns. It should however be noted that this technique is not suitable for linear colliders as the target would not withstand the high energy of the beam. One unit

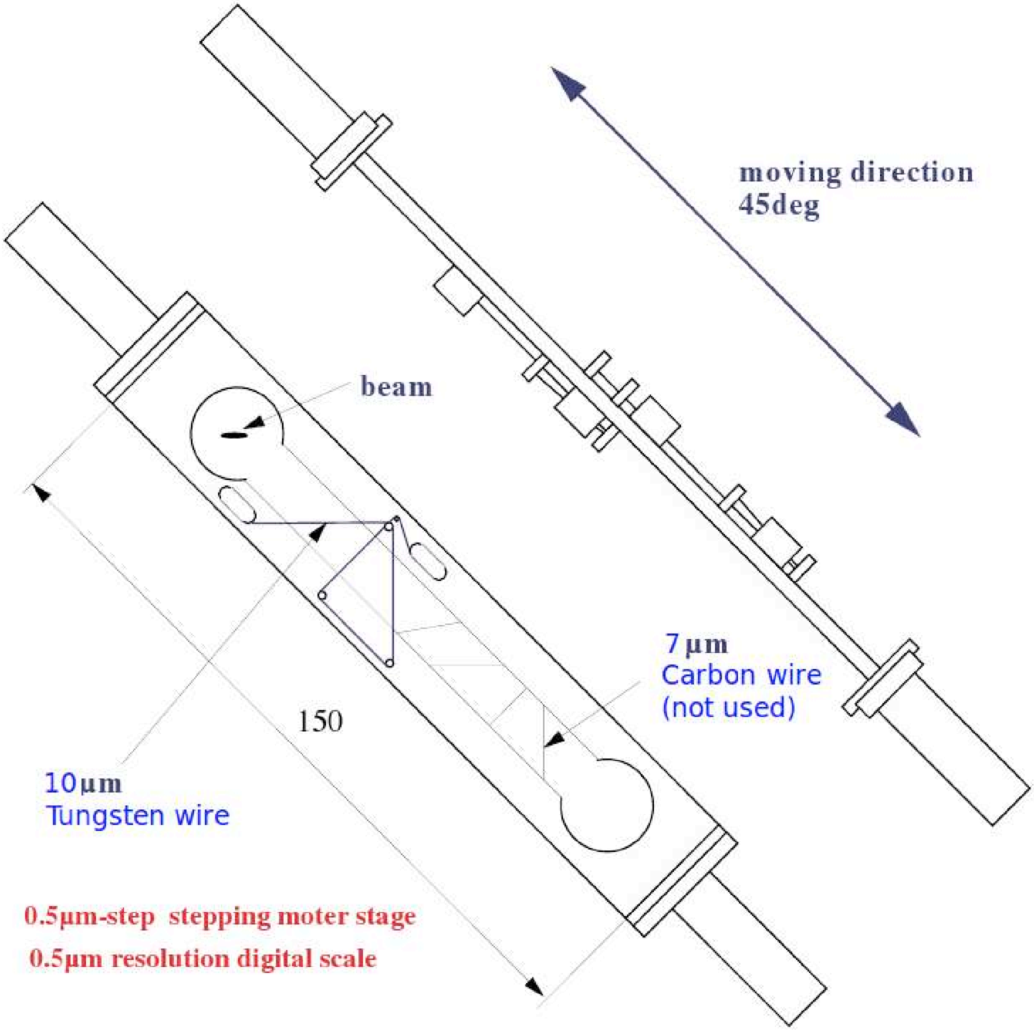

Figure 4.6: Wire-scanner in the ATF2 diagnostic section.

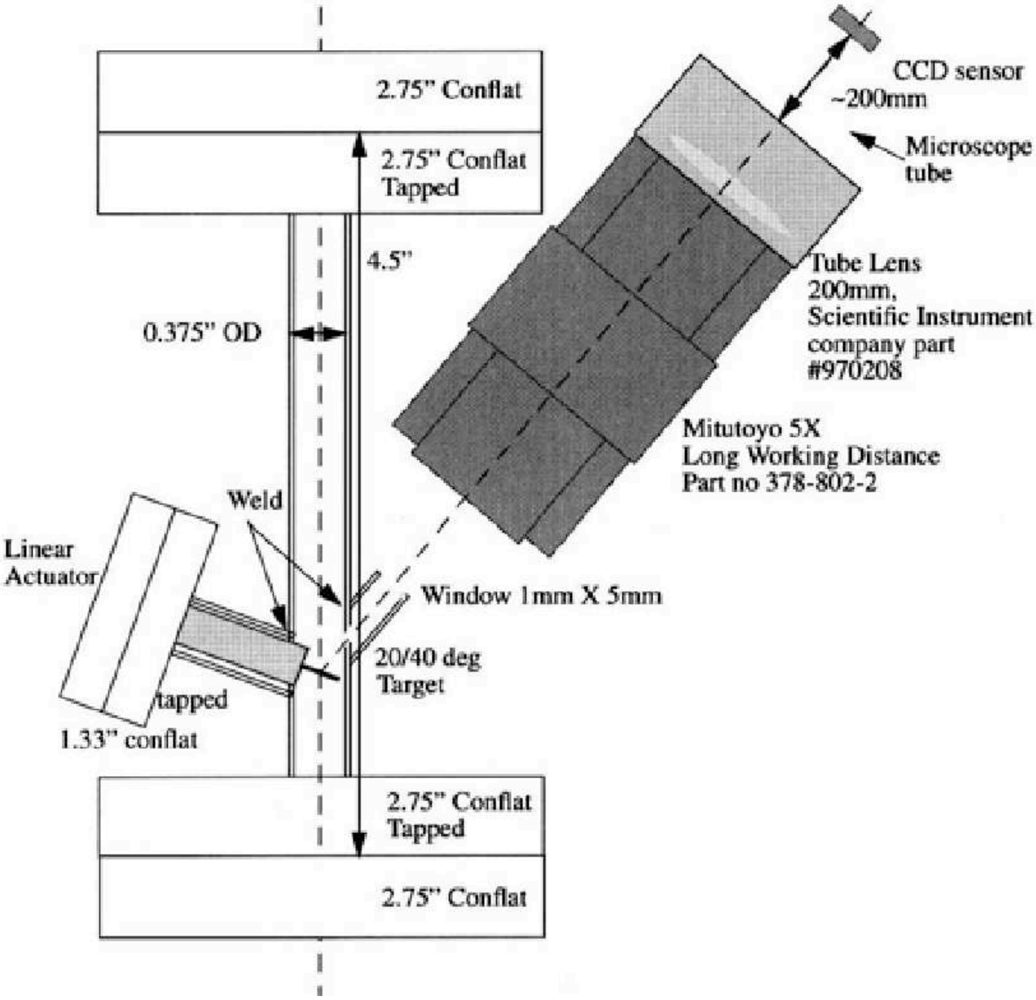

Figure 4.7: Scheme of the OTR installed in the ATF2 extraction line.

is presently installed at the beginning of the ATF2 extraction line, and four more will be installed in the diagnostic section in 2010 to allow fast emittance measurements.

4.2.3 Laser Wire

For beam sizes of a few microns as in the beam delivery system at the international linear collider (ILC) since wire scanner or OTR monitors cannot be used, as the beam would destroy them, a very intense laser, strongly focused to a few microns, is used intead. Photons from Compton scattering off the electron beam are generated along its direction [24][25]. A detector placed downstream of the collision point measures the flux of theses scattered photons, as shown in figure 4.8.

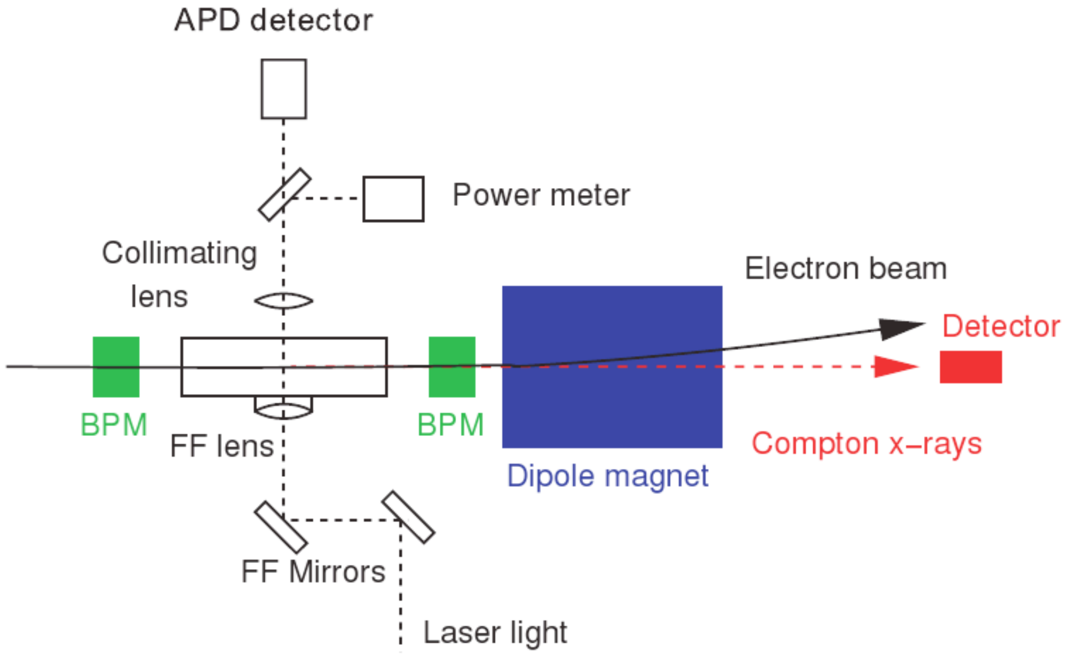

Figure 4.8: Schematics of the laser wire apparatus.

Even if laser wires have several advantages compared to conventional ones, like it is non invasive (it does not disrupt the beam) and it is usable with beams of a few micron in beam size, the measurements have several specific issues, such as the focusing of the laser beam at the appropriate beam location and timing issues (powerful lasers usually have very short lengths: the one used for the present laser wire experiment has a pulse length of $150ps$).

4.2.4 "Shintake" Monitor

Unlike a linear collider, where the beam sizes can be deduced and optimized using several effects resulting from the collisions of the two beams, ATF2 has only one beam. That's why a direct measurement of the beam size is needed.

The "Shintake" monitor is a nanometer scale beam size monitor allowing to probe the electron beam by its interaction with an interference fringe pattern formed by split laser beams [26] (see figure 4.9). It has been successfully used previously at the Final Focus Test Beam (FFTB) experiment at SLAC[27].

The photons of the fringe pattern interact with the beam by inverse Compton scattering effect, producing gamma rays in the electron propagation direction. The number of photons created is proportional to the photon density at the beam position. Scanning the phase of the laser fringe or moving the beam produces a modulation of the gamma ray flux depending on the electron beam size.

Four laser crossing angles can be used in the system installed at ATF2 (174^0, 30^0, 8^0 and 2^0), allowing to measure a wide range of different vertical beam sizes. The expected resolution function of the beam size and the laser crossing angle [28] is displayed in figure 4.10

The range of measurable vertical beam sizes goes from $25nm$ up to $6\mu m$. For larger beam sizes a 10 μm tugsten wire-scanner has been installed in the interaction chamber. In addition a system with $10\mu m$ tungsten and 5 μm carbon

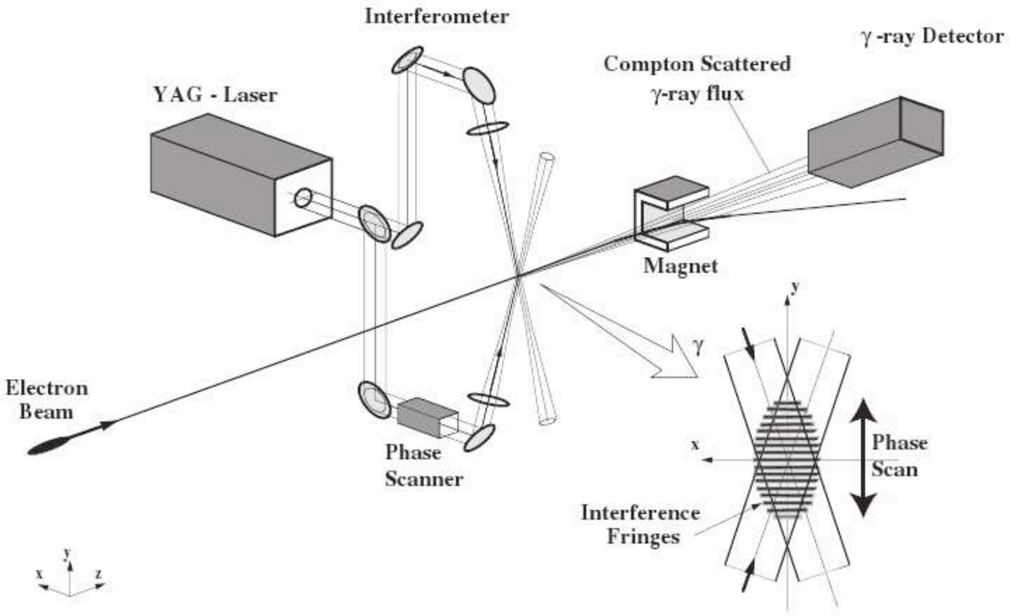

Figure 4.9: Schematics of the "Shintake" monitor.

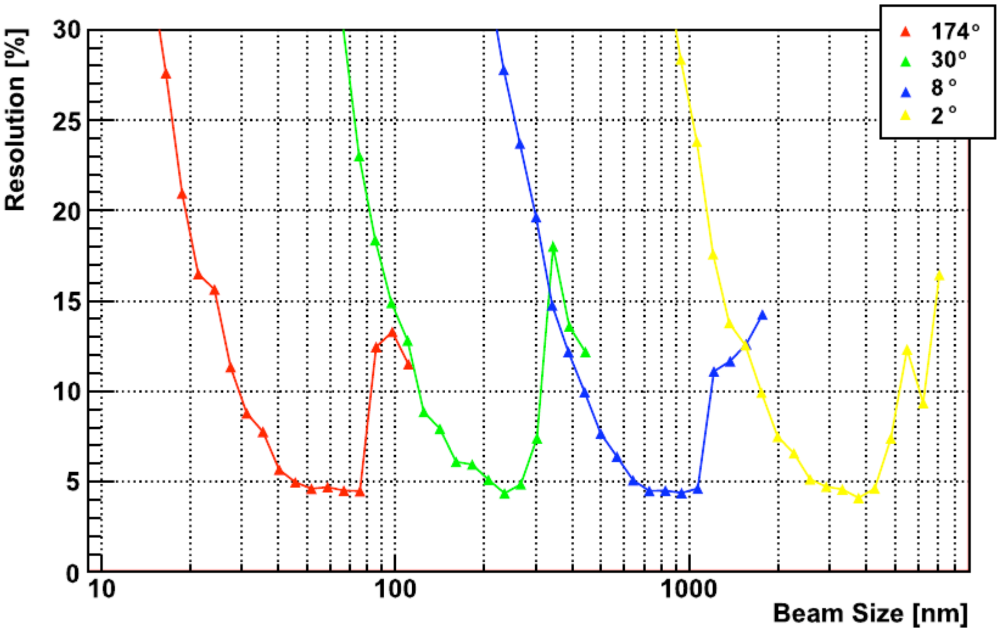

Figure 4.10: Expected resolution curves of beam size measurement in different crossing angles.

wires is also available at a location $40cm$ downstream.

Chapter 5

WORK DONE ON STRIPLINE BPMS ELECTRONICS

In the early stage of the commissioning, as we started looking at the BPMs measurements in the extraction line, several problems were found:

- for some BPMs, huge measured displacements (even bigger than vacuum chamber for MQM4X) (see figure 5.1).

- very large beam position jitter measured by striplines (at that moment, cavity BPMs were not available) due to intensity dependence (see figure 5.2).

- offsets between the centers of the stripline BPMs and the magnets to which they are fixed changed from week to week by much more than the Beam Based Alignment (BBA) estimated resolutions (see figure 5.1). The section 6.2.1 describes the BBA procedure used to obtain such offset measurements.

- the last three stripline BPMs which used newer electronics (see table 5.1) do not have these problems.

These observations, associated with the fact the striplines were the only BPMs available at the beginning of the commissioning, made us suspect an electronics problem. That is why we studied and tried to fix the electronics.

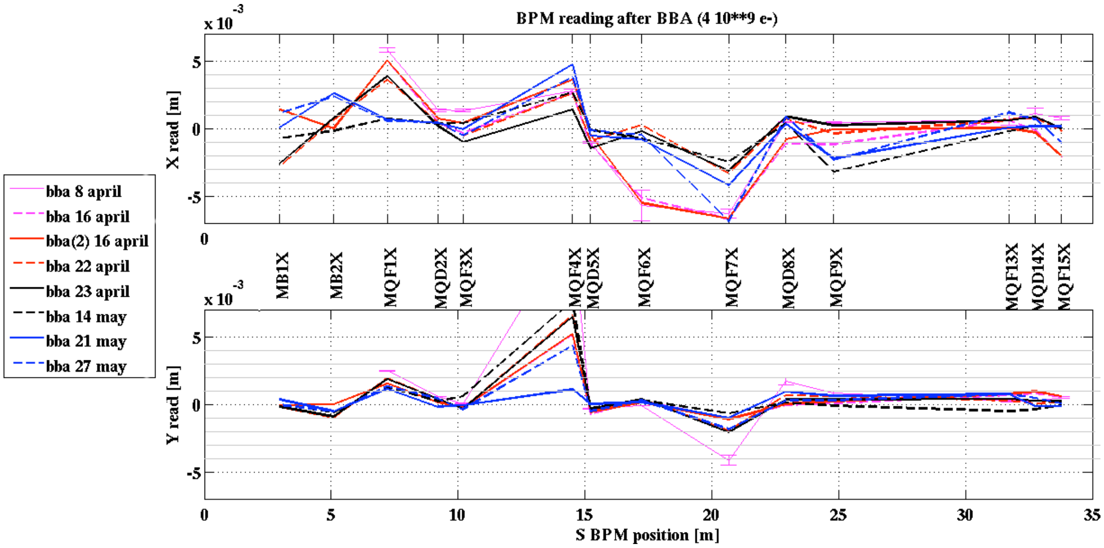

(a) Orbit after several beam based alignment

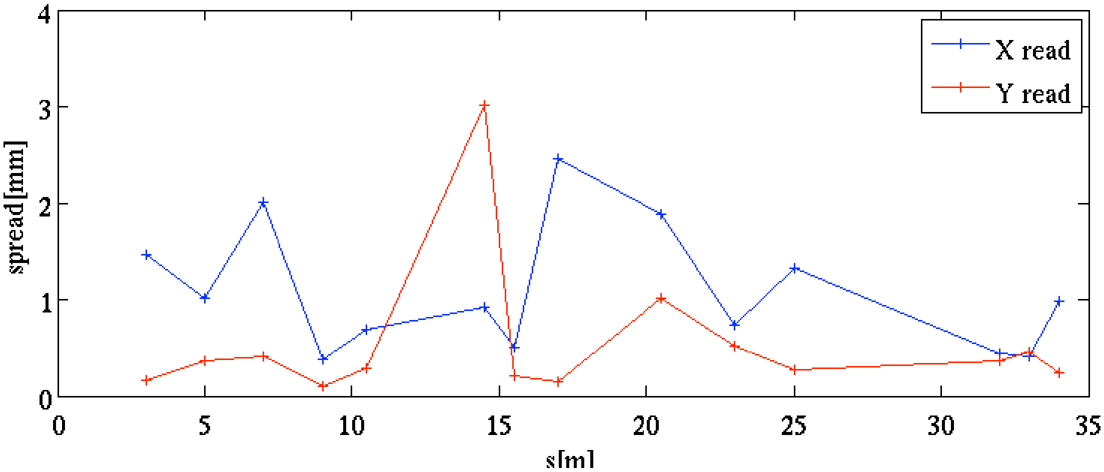

(b) Spread of the orbit after several beam based alignment

Figure 5.1: Orbits (a) and spread (b) of the offset between BPMs and magnet centers after several beam based alignment implementations. As the BPMs are fixed, the BPM reading value after BBA is supposed to be stable within the precision of the method (pink error bars in (a)).

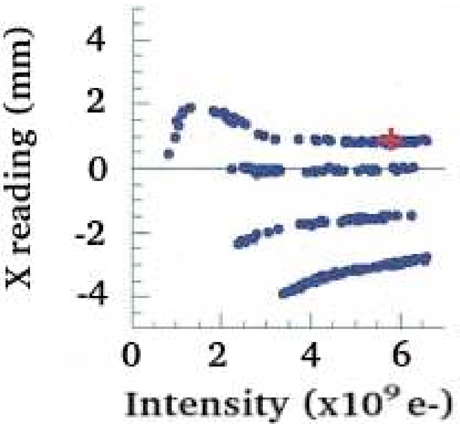

(a) X readings of MQF1X

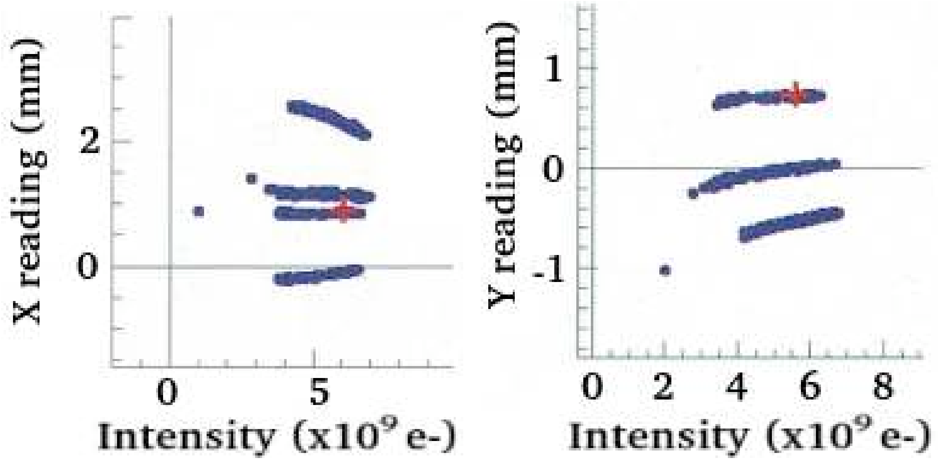

(b) X readings of MQF2X (c) Y readings of MQF2X

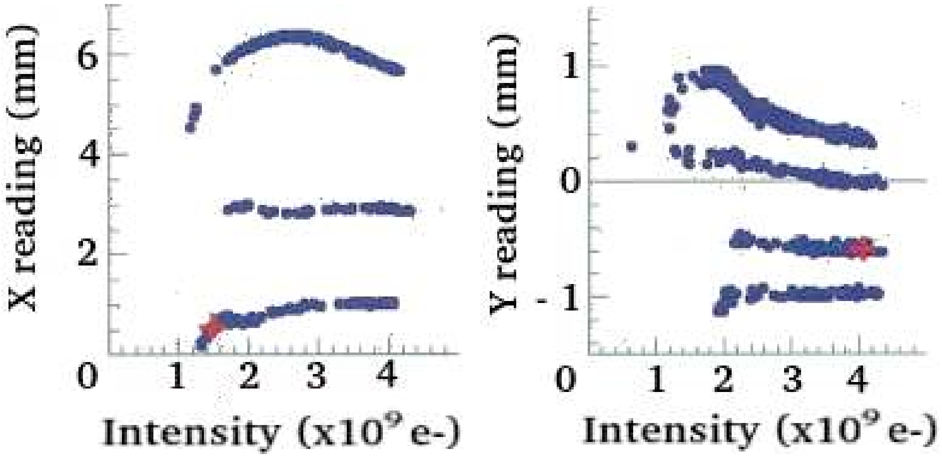

(d) X readings of MQF3X (e) Y readings of MQF3X

Figure 5.2: Beam position measured by the indicated stipline BPM function of the intensity of the beam for different beam positions in the stripline. As this behavior was not observed in other BPMs, it is created by the striplines or their electronics and not by a beam trajectory which depends on the intensity.

5.1 Description of the Stripline BPMs and Electronics

5.1.1 Stripline BPMs

Description

Stripline BPMs have 4 electrodes, 2 in the horizontal and 2 in the vertical planes (see figure 5.3). Both extremities of each electrode act as a current source when the beam goes through due to wall currents. When the electron beam arrives, it creates a positive current that propagates in both directions. The first half of the signal is collected at port 1 whereas the second is canceled by half of the negative current produced at the other extremity (since the beam is relativistic and move as quickly as the signal). The second half of the negative signal goes back to port 1 and is collected after $\frac{2l}{c}$ where l is the length of the stripline.

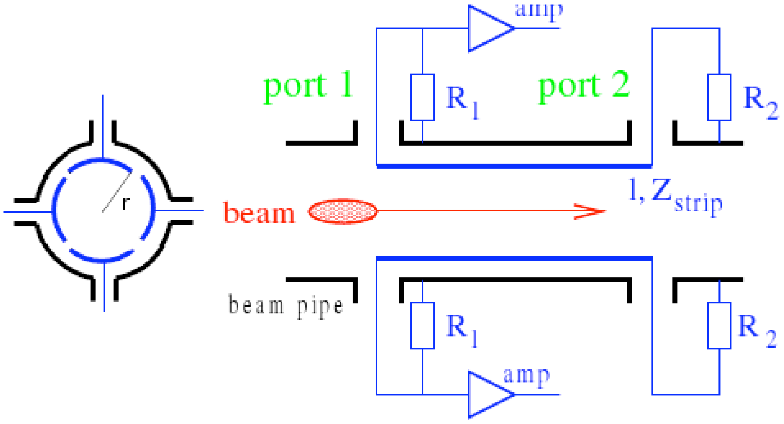

Figure 5.3: Transverse and longitudinal scheme of a stripline BPM.

All the striplines BPMs are located in the ATF2 extraction line (see figure 5.4). As they are $4cm$ long, except for the last 4 BPMs (MQF9X, MQF13FF to MQF15FF) which are $12cm$ long (see table 5.1), the time between the two pulses is $260ps$. As the typical bunch length is $8mm$, each induced pulses is $26ps$

long (see figure 5.5).

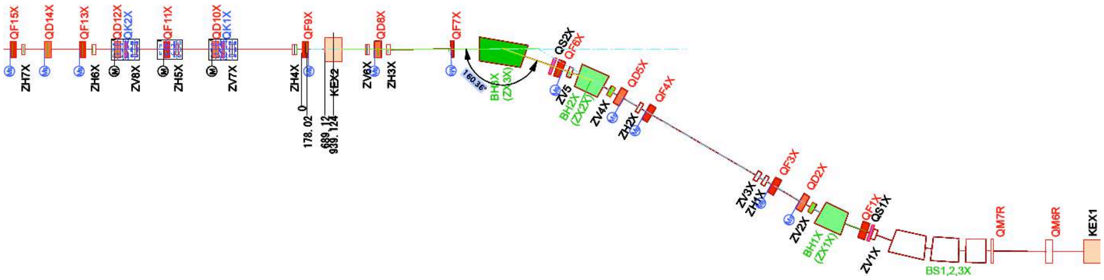

Figure 5.4: Schematic of the ATF2 extraction line with the stripline BPM locations.

BPM name	length	diameter	remarks
MQF1X	$4cm$	small	
MQD2X			
MQF3X		big	
MQF4X			bad connection at one electrode
MQD5X			backward
MQF6X		small	backward
MQF7X		big	
MQD8X		small	
MQF9X	$12cm$		backward
MQF13X			new electronics [29]
MQD14X			new electronics [29]
MQF15X			new electronics [29]

Table 5.1: Characteristics of the stripline BPMs

Frequency Analysis

The Fourier transform of the signal $V(\omega)$ induced by an infinitely short bunch is:

$$V(\omega) = \frac{\alpha}{2\pi} \cdot \sin\left(\frac{\omega l}{c}\right) \cdot e^{i\left(\frac{\pi}{2} - \frac{\omega l}{c}\right)}$$

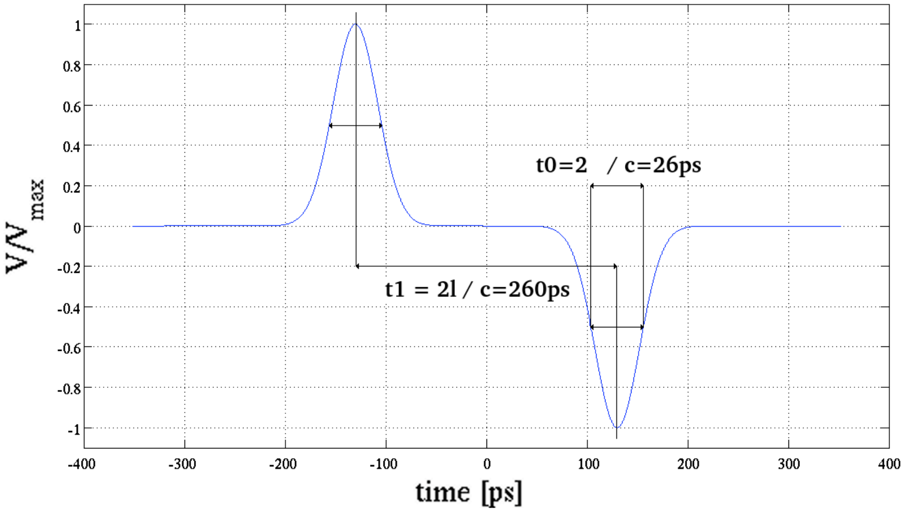

Figure 5.5: Shape of the signal at the output of a stripline BPM.

The first maximum amplitude is obtained at $f = \frac{c}{4l} = 1,88GHz$, but, unfortunately, at the time when the electronics circuit was built, "cheap" amplifiers were not able to work at that frequency. The amplifier used could not accept signal at higher frequency than $100MHz$, which means the amplitude of the signal in the range of acceptance of the amplifier is much lower than if the electronics was working at higher frequency and, as we will see section 5.4.1, the noise is at low frequency, the signal over noise ratio is much smaller too.

In figure 5.6 is the comparison of this spectrum with a more realistic one induced by a Gaussian beam with a full width at half maximum of $26ps$. We can see a modulation due to the Gaussian shape of the beam, but the frequency of the first maximum amplitude is the same as well as the behavior at low frequency: $V(f) \propto \frac{fl}{c}$ for $f \ll \frac{c}{2\pi l}$.

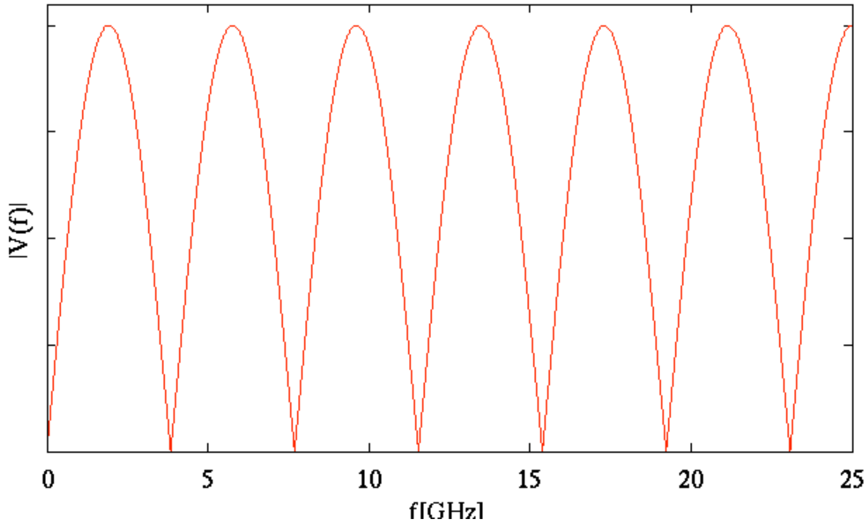

(a) Signal Fourier transformation with a punctual beam

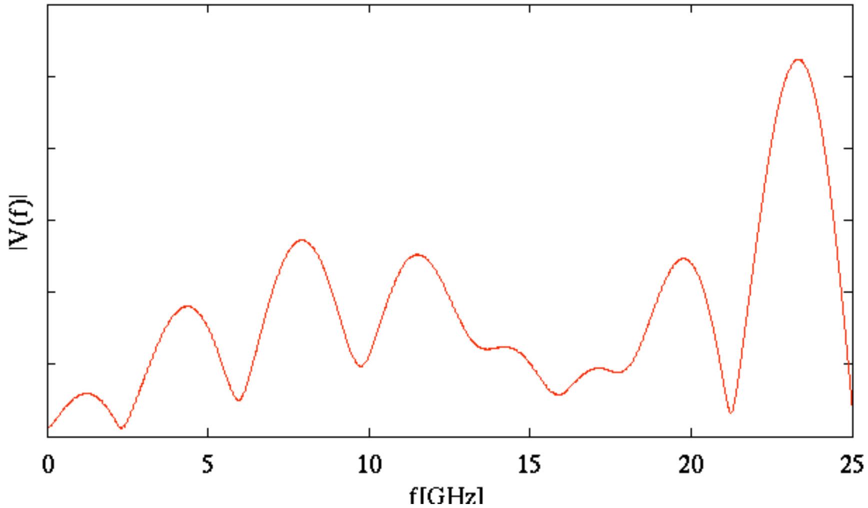

(b) Signal Fourier transformation with a realistic beam

Figure 5.6: Frequency response of the striplines (arbitrary vertical scales).

Noise Considerations

As the signal amplitude induced on each electrode (A_1 and A_2 in the horizontal plane) is inversely proportional to the beam distance, we have at first order approximation:

$$X_{beam} - X_{center} \propto A_2 - A_1 \tag{5.1}$$

Also, as the amplitude is proportional to the beam intensity, to have an intensity independent signal, one takes:

$$\Delta X_{meas} = X_{beam} - X_{center} \propto \frac{A_2 - A_1}{A_2 + A_1} \tag{5.2}$$

That last formula is used for ATF2 striplines BPMs. If we consider a beam with a displacement δ compared with the center of a BPM of radius R, with measured amplitude A when the beam is at the center, we obtain, when the beam is displaced by δ from this center:

$$\begin{aligned}
\frac{A_2-A_1}{A_2+A_1} &= \frac{\frac{A}{R-\delta}-\frac{A}{R+\delta}}{\frac{A}{R-\delta}+\frac{A}{R+\delta}} \\
&= \frac{(1+\frac{\delta}{R})-(1-\frac{\delta}{R})}{(1+\frac{\delta}{R})+(1-\frac{\delta}{R})} \quad \text{Taylor series 1st order}(\tfrac{\delta}{R} \ll 1) \\
&= \frac{\delta}{R}
\end{aligned}$$

The quantity in equation 5.2 is thus proportional to the displacement, as expected ($\Delta X_{meas} = R\frac{A_2-A_1}{A_2+A_1}$) if that displacement is small compared to the aperture ($\frac{\delta}{R} \ll 1$).

If now we consider the noise at the electrodes N_1 and N_2, we get:

$$\frac{\Delta X_{meas}}{R} = \frac{A_2 + N_2 - A_1 - N_1}{A_2 + N_2 + A_1 + N_1} \sim \frac{2\frac{\delta}{R} + \frac{N_2-N_1}{A}}{2 + \frac{N_2+N_1}{A}}$$

Considering the noise has an amplitude N small compared to the measurement ($\frac{N}{A} \ll 1$) we obtain:

$$\frac{\Delta X_{meas}}{R} \sim \frac{2\frac{\delta}{R} + \frac{\sqrt{2}N}{A}}{2} = \frac{\delta}{R} + \frac{N}{\sqrt{2}A}$$

So the resolution r, defined as the measured displacement due to the noise, is:

$$r = R\frac{N}{\sqrt{2}A} \tag{5.3}$$

The radius of the striplines is about a few tens of millimeters, to have stripline resolutions of tens of microns the amplitude measurement at each electrode must be reliable at $\sim 1‰ (\frac{N}{A} \sim 0.001)$.

To measure the amplitude of the signal, each electrode is connected to a head amplifier (Head-amp) circuit and then to a clipping circuit. The signal obtained (negative part of the signal) is then integrated and measured with an ADC.

5.1.2 Head-Amp Circuit

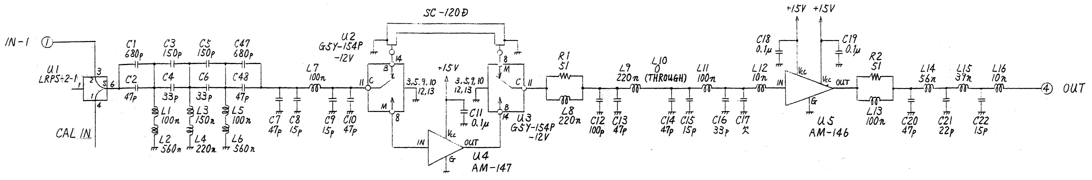

Figure 5.7: Head-amp electronics of stripline BPMs.

The head amp circuit (see figure 5.7) has the function to filter and to amplify the electrodes signals within the dynamic range of the clipping circuit.

Before the first amplifier, we have the dominant pass band filter with first a Butterworth high-pass filter of seven stages with $f_c = 10MHz$, then a Butterworth low-pass filter of three stages with $f_c = 50MHz$. At the output of each amplifier, there is anti-aliasing (low pass) filter.

The first amplifier with a gain of $17dB$ can be by-passed to lower the overall amplification in the case of multi-bunch operation.

5.1.3 Clipping Circuit

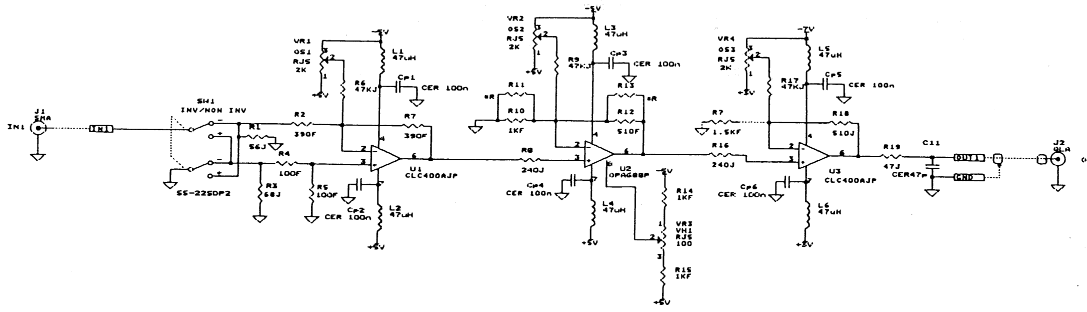

Figure 5.8: Clipping circuit electronics of stripline BPMs.

The clipping circuit includes a switch to reverse the polarity if the attached BPM is mounted backward (in that case the signal is reversed and the switch sets it back), an inverter amplifier, an amplifier which imposes a maximum output voltage (a bit like a diode), and then another inverter amplifier (see figure 5.8).

The three amplifiers each have potentiometers which allow to control the negative tension of the power supply, and thus the DC offsets at their outputs. There is a fourth potentiometer to define the maximum voltage limit. This defines the clipping voltage.

5.2 Check of the Electronics

A pulser able to create a signal comparable to the stripline signal (see figure 5.5), with a controllable attenuation from 0 to $63dB$ was used for the electronics check. The four channels (one per electrode) of both circuits for each stripline BPMs have been checked:

- the output level of each board and the signal shape has been checked with an oscilloscope to ensure that no amplifier has been damaged.
- the inverter switch position has been verified to be coherent with the direction of the corresponding stripline.
- the high pass filter was bypassed on all head-amp circuit except for MQF4X. The result was a signal 5 times lower, so the filter was skipped there too.

It was found that the polarity switch were not set correctly for the backward stripline BPMs and that the preamplifier circuit of MQF4X was different from the others due to the fact it had a lower gain. However, that did not explain the overall behavior, so it was decided to try to re-tune the clipping circuit.

5.3 Tuning of the Clipping Circuit

The tuning procedure of the clipping circuit consists in adjusting the four potentiometers which control the output offsets of the three amplifiers and the clipping level for each channel.

5.3.1 Tuning of the Amplifier Offsets

It is important to have no offset at the output of the circuit since after the clipping circuit, the signal is integrated over a time much longer than the pulse induced by the beam. That is because the ADC is common to all striplines, and they are spread over $20m$, which correspond to $66ns$ whereas the signal is $0.26ns$ long and with amplitude around $1V$. If we want the contribution of the signal to be ten times higher than the offset, it means that the offset must be $0.1 \times \frac{0.26}{66} = 4 \times 10^{-4}$ lower than the signal, so below $0.4mV$.

The offset of each amplifier has been tuned down to $0.2mV$ using a DC voltmeter, but most of them actually were already below $0.4mV$ before the tuning.

5.3.2 Tuning of the Clipping Level

The offset of the amplifier acting like a diode must also be tuned to adjust the clipping level. We saw the signal has to be as high as possible, so the tuning of the clipping level was made to minimize the positive part of signal and avoid cutting the negative part, which both would result in a decrease in integrated signal. To make a precise tuning, the amplitude of the pulse generated by the pulser has been decreased by ten $(0.1V)$ and the clipping level increased until the overshoot was clearly visible before setting it to minimize it.

The initial settings were close to one obtained by the new tuning and no noticeable improvement in the striplines measurements resulted from that tuning.

5.4 Study of the Calibration Procedure

As the tuning of the circuit was not the source of the problem, another idea was tested. The kicker system radiates low frequencies (compared to a BPM signal) and this could affect the measurement by adding DC components to signal readout on each electrode. We will see first what the noise amplitude is at different stages of the electronics and what is the noise influence on the calibration of the BPMs.

5.4.1 Kicker Noise Effects

The kicker noise has been measured at three different representative striplines (MQF1X, MQF2X, MQF9X), before and after the head amp circuit. This measurement has been made without beam but with the kicker firing at its usual strength. A numeric oscilloscope was used to see the frequency spectrum of the noise.

The noise was found to be reproducible over several hours, different for each electrode, and with frequencies between 1 and $2MHz$ as shown in figure 5.9 and 5.10. At that frequency the signal is amplified by the head-amp circuit from $2mV$ peak to peak amplitude to $40mV$, which corresponds to $13dB$ amplification ($34dB$ amplification by the amplifiers and $-20dB$ attenuation from the high pass filter at $10MHz$).

As the signal level is about $1V$, that means we will have an offset of about $40 \times 10^{-3} \times R \simeq 2mm$ by kicker noise (according to equation 5.3). This is consistent with the order of magnitude of the spread in positions measured by each stripline after beam based alignment (see figure 5.1).

The readings after BBA should be comparable within the corresponding expected beam based alignment resolution, as the BPMs are fixed compared to the magnets. Few times a run period, it was needed to change significantly the kicker strength (of $\sim 10\%$) to optimize the extraction when the conditions in the ring changed. It changed the amplitude of the noise collected by the striplines and can explain a fraction of the spread of the post-BBA BPM readings.

5.4.2 Stability of the Calibration

To compensate for the amplifiers' non-linearities, the integrated signal measured by the ADC is corrected by the control system according to a polynomial function obtain through calibrations with the pulser. Various signal amplitude are provided using the tunable attenuation Att and, the output V of the ADC is measured. The curve is fitted by a 4^{th} order polynomial:

$$V_{fit}(Att) = aV^4 + bV^3 + cV^2 + dV + e = V_{ref} * 10^{-\frac{Att - Att_{ref}}{20}}$$

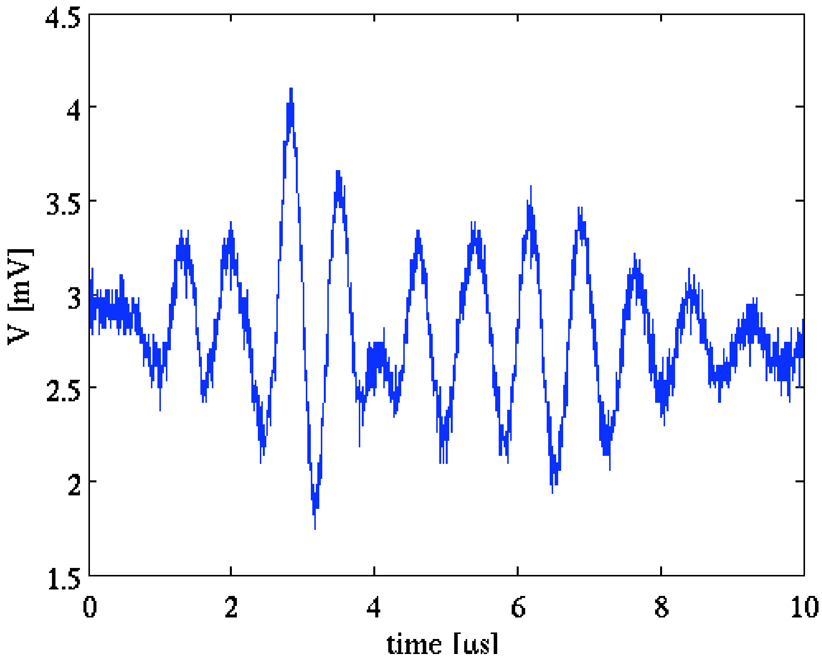

(a) signal before head amp circuit

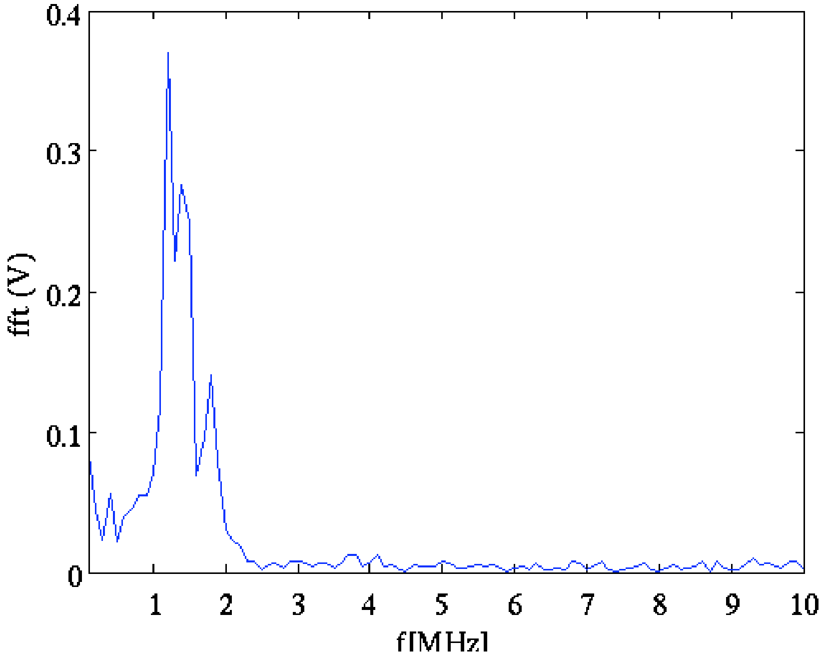

(b) FFT of signal before head amp circuit

Figure 5.9: Kicker induced signal at MQF1X and its FFT before the head amp circuit.

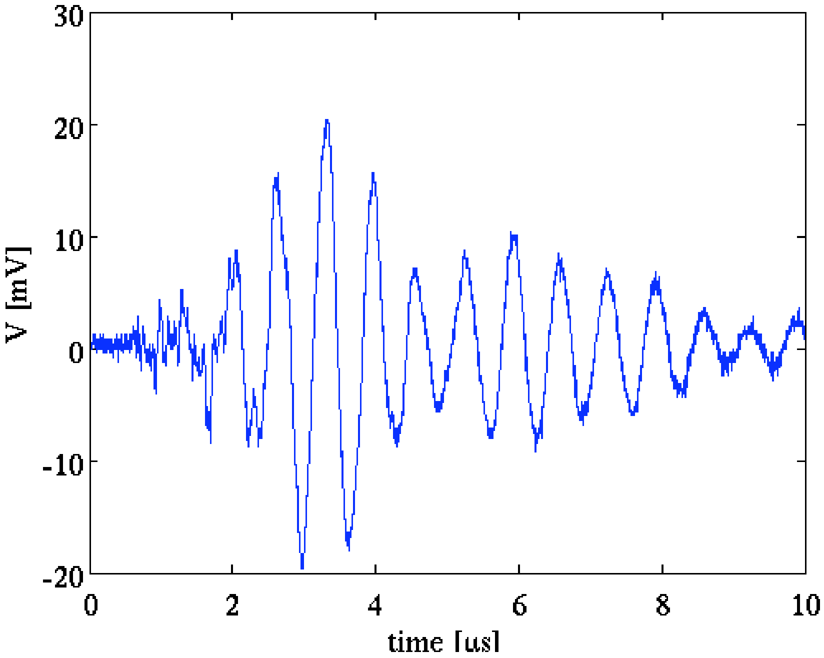

Figure 5.10: Kicker induced signal at MQF1X and after the head amp circuit.

The calibration has always been made with the kicker switched off. When we compare the polynomial fit obtained without the kicker to measurements with the kicker switched on, we saw differences at the level of 10%. This could lead to the $\simeq 5mm$ offsets observed. Figure 5.11, where the relative error from using the fit with polynomial coefficients obtained calibrating MQF1X with the kicker switched off with measurements kicker off (in cyan and blue) and kicker on (in red).

However, as the kicker noise is stable from a measurement to other one, it should not have any influence on relative measurements (pulse to pulse orbit variation). Instead, to see the influence on relative measurements, one should look at the spread of the ADC counts. The figure 5.12 display the relative spread of the ADC counts ($\frac{\sqrt{<ADC^2>}}{<ADC>}$) function of the attenuation. Around an attenuation of $20dB$, which corresponds roughly to a beam signal, we can see

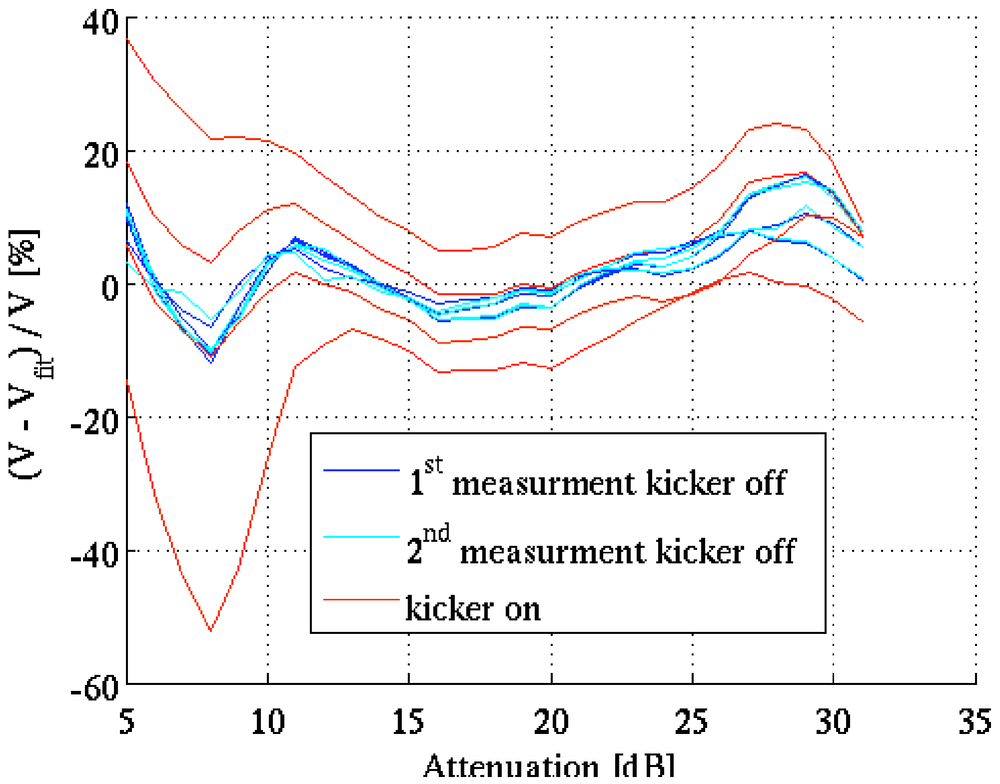

Figure 5.11: Fractional differences between the signal on each of the four electrodes of MQF1X and the fitted polynomials obtained during the calibration without the kicker. The blue curves correspond to the residuals when using the same measurements as for the calibration. The cyan curves correspond to the residuals for a different measurement in the same conditions. The red curves are the residuals while firing the kicker.

error source	effect	quantification
kicker noise and timing changes	long term non reproducibility of measurements	$2mm$
kicker noise and fit of ADC counts	absolute measurement error	$5mm$
electronics noise	relative measurement error	$150\mu m$

Table 5.2: Stripline errors sum-up.

the relative spread is about $3‰$which induces a spread in resolution of relative measurement of $150\mu m$. This value does not change when the kicker is switched on, as expected for a reproducible noise and must come from other sources (amplifiers noise, ADC).

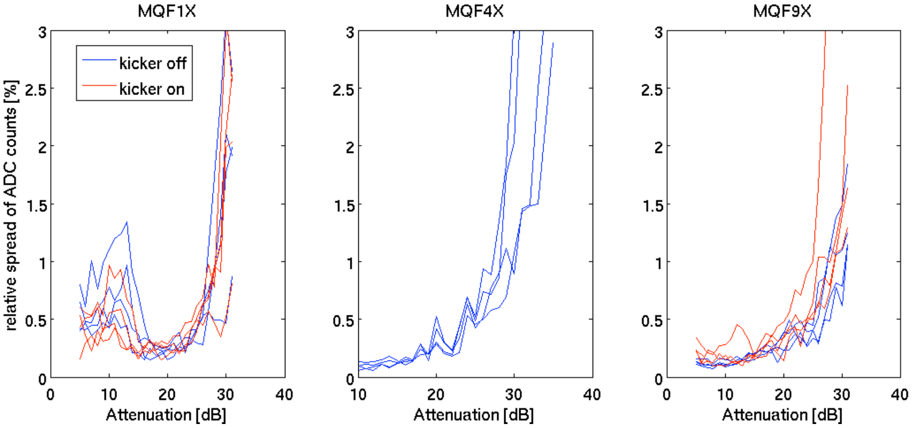

Figure 5.12: Relative spread of the ADC counts function of the attenuation for MQF1X, MQF4X and MQF9X.

The table 5.2 sums up the noise origins and their consequences.

5.5 Improvements

As the current state of the stripline is not satisfactory, several option have been considered. An additional low pass filter has been tried to remove the kicker noise, but it modified the beam signal far too much to be useful. Also the kicker itself is planned to be changed by a fast kicker, but it is still under testing, and will not replace the actual one before next year.

The solution retained has been to replace the electronics with a faster one (around $1GHz$), running at higher frequency, so the useful signal will be larger, and one will be able to filter the kicker noise out.

Chapter 6

PROCEDURE TO ACHIEVE A VERTICAL BEAM SIZE OF 37 NM

6.1 Overview of the Tuning Procedure

The tuning of ATF2 is very challenging, with restrictive tolerances and various tuning procedures needed to reach the nominal beam size. All the errors to be corrected are: the misalignment of the magnets, the strength errors, the matching errors between the design Twiss parameter at the injection of the extraction line and the one provided by the ring.

The order of the corrections matters. The first step is fixing the trajectory, but firstly the beam based alignment (BBA) had to be done previously in order to get the misalignment of the BPMs respect to the magnet centers. As the BPMs are fixed to the magnets, the BBA is needed only once. Then the dispersion, the coupling and the beta functions are measured and corrected in the matching section at the beginning of the final focus.

Due to the design introducing a large magnification between the extraction line and the final focus, waist position, dispersion and coupling errors are easily generated. There are also higher order aberrations of the beam at the IP caused by the sextupoles. All these aberrations are corrected by using sextupoles movers.

6.2 Trajectory Correction

6.2.1 Beam Based Alignment

The goal of the Beam Based Alignment (BBA) is to determine the position of the center of the BPM (called electrical center) with respect to the magnetic center of the magnet where it is attached. This offset is added to the measurements of the BPM so as to give the position of the beam with respect to the center of the magnet.

The BBA consists in getting the measurement of the position in a downstream BPM when the beam goes through the center of the magnet. This center is determined by a scan of the beam position in that magnet for different strengths. That scan of the beam position in the magnet can be done either with an upstream corrector, or with a mover (if the magnet is attached to a mover).

The kick induced by a quadrupole is proportional to the distance from the center, the kick induced by a sextupole is proportional to this distance in the vertical plane and to the square of this distance in the horizontal plane; all kicks being proportional to their strengths. The position in the downstream BPM function of the displacement in the quadrupole is a line. Its slope is proportional to the quadrupole strength. The horizontal beam position in the downstream BPM function of the horizontal beam position in the sextupole is a parabola that has the quadratic coefficient proportional to the sextupole strength.

As the center of the quadrupole and sextupole magnets has a zero field whatever their strengths are (in an ideal case), the position of the beam in the downstream BPM will be the same whatever the strength of the magnet is. The figure 6.1 shows typical measurements at a downstream BPM in the case the horizontal or vertical beam position is scanned in a quadrupole and a

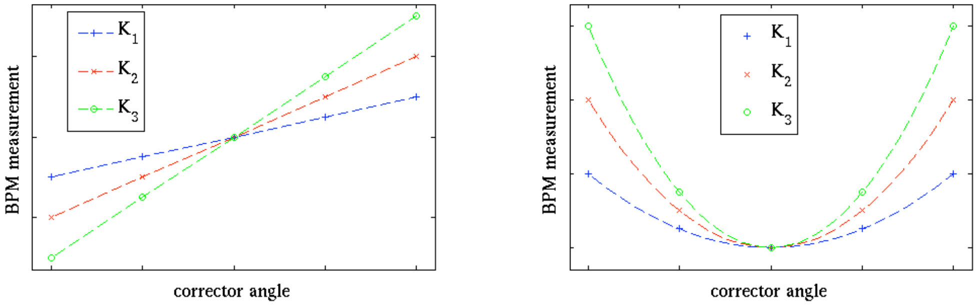

(a) BBA for a quadrupole or vertical BBA in a sextupole

(b) horizontal BBA for a sextupole

Figure 6.1: Typical measurements at a downstream BPM during a position scan in a quadrupole or in a sextupole vertically (figure (a)) or in a sextupole horizontally (figure (b)) for different strengths (K_1, K_2 and K_3).

sextupole.

Any downstream BPM or upstream corrector magnet cannot be used. As the angle introduced by the corrector must be converted to position in the magnet, the betatron phase advance (see section A.1) between the corrector and the magnet must be non-zero. The angle introduced by the magnet must also be converted to position at the downstream BPM, so the phase advance between the BPM and the magnet must be non-zero too.

For a quadrupole, two scans with different quadrupole strength are enough to determine the position of the intersection of the line fitted for each strength. As the readings of the BPM attached to the quadrupole is logged during the scan, the beam position corresponding to that point can be calculated.

For a sextupole, one scan can be enough in the horizontal plane as the beam goes through the center of the sextupole at the parabola minimum. The beam position in the BPM attached to the sextupole at that point can also be obtained from the data taken by this BPM during the scan.

6.2.2 Trajectory Steering

Once the readings of all the BPMs have been corrected by the BBA, getting the beam to go as close as possible to the center of all magnets is equivalent to minimizing the spread in the measured trajectory. That is done using corrector magnets and quadrupole movers. In section 8.2 a detailed description is presented to find the strengths of the correctors and the displacements of the quadrupoles needed for such a correction.

6.3 Corrections in the Extraction Line

6.3.1 Dispersion Correction

The dispersion has to be corrected in the extraction line since it is hard to correct it very precisely in the ATF ring. A large dispersion makes the beam large, making subsequent corrections more difficult.

The dispersion measurement is made by recording trajectories with different beam energies. The dispersion is the ratio of the trajectory variation over the energy variation. The beam energy can be changed varying the ring cavity frequency or reconstructing the natural energy fluctuation from bunch to bunch.

These two methods have been implemented and are compared in section 8.4. The correction of the horizontal dispersion changing quadrupole strengths and the correction of the vertical one using skew quadrupoles or correctors will be described. Figure 6.2 shows a comparison between the measured dispersion (varying the ring cavity frequency), the design dispersion and the estimation of result of the calculated corrections.

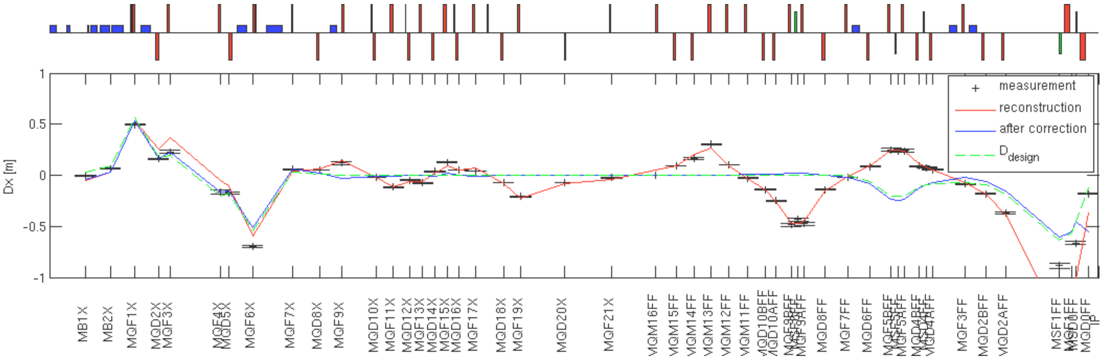

Figure 6.2: Comparison of the measured dispersion (varying the ring cavity frequency), the design dispersion and the estimation of result of the calculated corrections.

6.3.2 Coupling Correction

As the vertical dispersion correction using skew quadrupoles may add some residual coupling to the beam, the coupling correction is made afterwards. There are several methods used to measure the coupling [30]:

- using wire-scanners measurements of the horizontal, vertical, and tilted sizes (resp. σ_x, σ_y and σ_u) of the beam at different positions along the beam line,
- measuring σ_x, σ_y and σ_u at one position during a scan of the strength of a skew quadrupole.,
- for cross check, sometimes the σ_x, σ_y and σ_u measurements during the skew quadrupole scan are made at several positions along the beam line.

Once the coupling has been measured, the value of the strengths of the skew quadrupoles in that section can be set to correct for it downstream. That determination can be done with the formalism described in chapter 9 or using an optics code to propagate back the opposite of the measured correlations and fit the skew quadrupole strengths.

However, the coupling measurements are not yet precise enough to allow a real reconstruction. Instead, the vertical beam size is usally just minimised during the skew quadrupole scans.

6.3.3 Beta Matching

In the same way as skew quadrupole scans allow to measure the coupling, upright quadrupole scans can be used to measure the emittance of the beam and the Twiss parameters. As described above, the measurement can be done either at several positions along the beam line, or through a quadrupole scan (an example of such a scan is shown in figure 6.3).

An optics code is used to fit the strengths of the matching quadrupoles, placed at the beginning of the final focus, to recover the desired Twiss functions downstream. It is especially important to check that we are close enough to the goal values of β_x^* and β_y^* before starting the next steps as it has a very strong influence on the beam size at the IP.

6.4 Corrections in the Final Focus

The optics corrections in the ATF2 final focus are made by displacing sextupoles because, once the corrections in the extraction line have been done, the sextupoles misalignments are the main source of aberrations at the IP. As these sextupoles are close to $\frac{\pi}{2}$ phase advance from the IP, only one phase of the aberrations can be corrected. This means corrections in the extraction line must be done very carefully.

6.4.1 Waist Position Correction

A horizontal displacement of a sextupole creates a quadrupole field and a dipole field proportional to the displacement (see section 9.1.1). Using a combi-

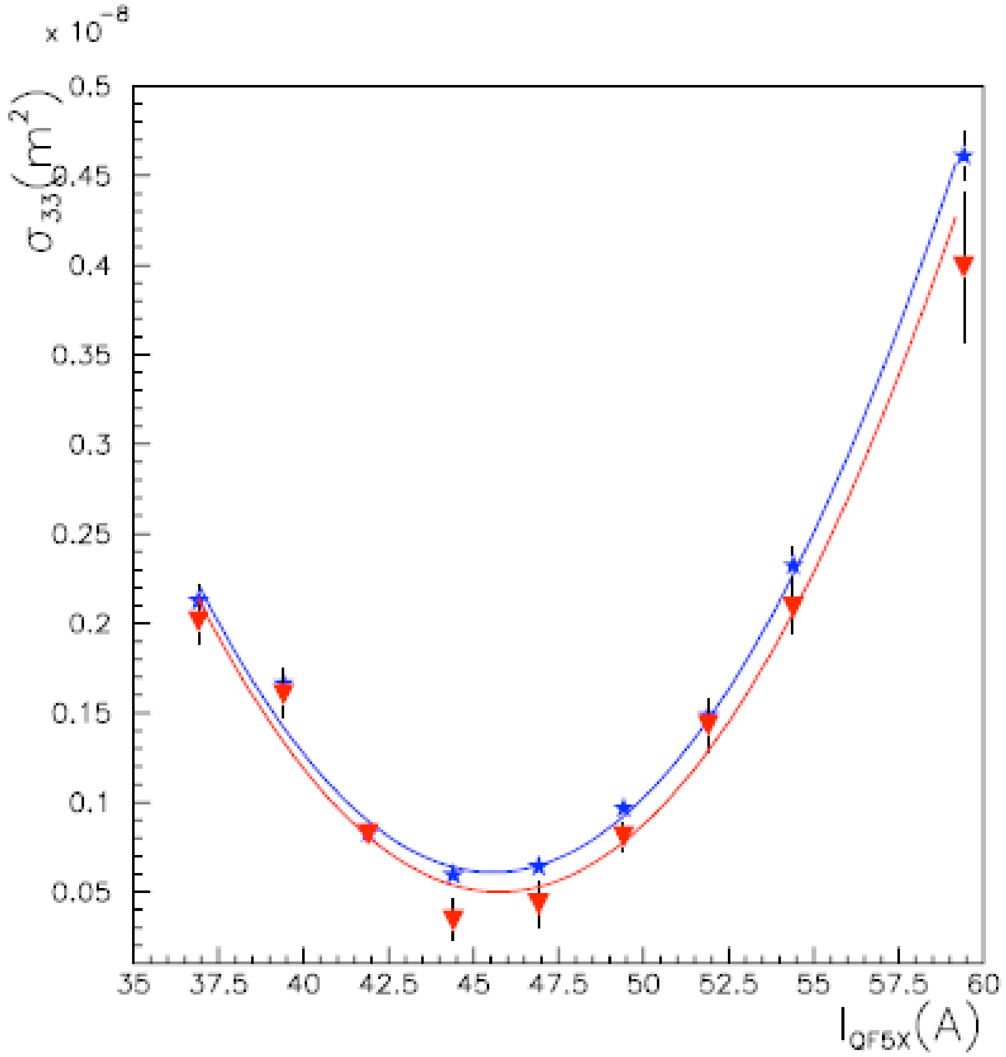

Figure 6.3: Square of the vertical beam size as a function of QF5X intensity. Blue stars correspond to the measured beam size, red triangles are after correction of dispersion effects.

nation of several sextupoles horizontal displacements, (or quadrupoles strength variations) it is possible to obtain an independent variation of the horizontal and vertical waist positions (see section 9.1.2). The square of the beam size at the IP depends quadratically on the waist position and the minimum is obtained when the waist is exactly at the IP. The waist position correction consists in setting the sextupoles at the positions where both horizontal and vertical waists are at the IP.

6.4.2 Dispersion Correction

The dispersion can be measured either directly with the BPMs or infered from beam size measurements during beam energy variations.

For the horizontal dispersion correction, quadrupole strengths in dispersive regions must be varied, which can be achieved with real quadrupoles or moving horizontally sextupoles.

For the vertical dispersion correction, as there are no skew quadrupoles in the ATF2 final focus, vertical displacement of the sextupoles or rolls of the quadrupoles must be used.

In the case the dispersion is corrected looking at the beam size, the principle is still to determine a combination of sextupoles displacements acting exclusively on horizontal or vertical dispersion, to scan this combination monitoring the beam size and to set the sextupole displacements at the value where the beam size is minimum.

6.4.3 Coupling Correction

As the magnets are all at the same phase in the final focus (except for the five matching quadrupoles), the coupling introduced by the vertical displacement of the sextupoles and the quadrupoles rotations are at the same phase.

The SF6FF sextupole is in a dispersion free region, so a coupling correction using only vertical displacement of that sextupole is possible since it will not introduce vertical dispersion. Combining movements of this sextupoles and of the ones in the dispersive region of the final focus thus allows controlling the dispersion and coupling independently at the IP.

6.4.4 Other Higher Order Aberration Corrections

Adding upright and skew quadrupole fields changes the transfer matrices between the sextupoles and breaks the symmetries introduced in the design. As these symmetries were introduced to cancel different high order chromatic effects, the misalignments of the sextupoles will introduce higher order aberrations. Knobs of sextupoles moves can be computed to correct such aberrations, for exemple $< x'x'y >$ and $< x'Ey >$.

6.5 Overview of the 2009 ATF Commissioning Runs

The ATF2 construction was completed in December 2008. The first objective was to pass the radiation inspection and make basic hardware and software checks. Only a few ATF2 magnets were switched on at that time to allow a very simple transport of the beam to the dump and the main effort was to minimize the beam losses.

During the second run period from February to March 2009, a configuration with large β^* ($\beta_x^* = \beta_y^* = 8cm$) using all magnets except the sextupoles was used [31]. With such high β values ($20\times$ bigger horizontally and $800\times$ bigger vertically than the design) the chromaticity was low enough not to require using the sextupoles. The corresponding beam size at the IP was $\sigma_x^* = 12.5\mu m$ and $\sigma_y^* \simeq 1 - 2\mu m$ allowing the first horizontal beam size measurements with the Shintake monitor in laser wire mode [32]. In that high β configuration, the beam is much smaller in the final doublet, reducing the background and making these measurements easier.

The third run period from April to May 2009 was focused on the tuning of the extraction line as detailed in the sections 6.2 and 6.3. The vertical β function at the IP was decreased to $\beta_y^* = 1cm$ corresponding to $\sigma_y^* \simeq 0.5\mu m$. This value was chosen because it was the smallest value for which the sextupoles were not needed and because it allowed the commissioning of the Shintake monitor in the 2^0 and 8^0 interference mode. As the cavity BPMs had stability issues and as there were still troubles with the stripline BPMs, the orbit correction and the dispersion correction were very difficult. In such conditions, the overall tuning procedure took even longer as the beam was for instance steered during quadrupoles scans. Development of the cavity BPMs, first optics checks (see section 8.1) as well as the first investigations on the stripline BPMs (see chapter 5) were performed in this period.

The autumn runs from October to December 2009 used the same optics as the previous run because the tuning was considered not to be totally successful yet and because the Shintake monitor had not yet succeed to make measurements in interference mode. After a lot of fixes and upgrades in software and hardware, the cavity BPMs started to work nicely and the Shintake successfully measured the beam size at the IP in interference mode fo the first time. As a result, the dispersion correction became much more precise (see section 8.4.2), the first automated trajectory correction (see section 8.2) and preliminary tests of final focus corrections could also be performed.

Chapter 7

THE ATF2 FLIGHT SIMULATOR

The ATF2 Flight Simulator [33] is an on line modeling tool which contains a constantly updated model of the ATF ring and of the ATF2 beam line. It can be used by optics specialists to develop applications for tuning and also allows non-specialists to use them.

One of the goals of the ATF2 collaboration is to implement an international collaboration in the field of accelerator physics, similar to what exists in particle physics. The challenge is that international collaborators, with varying availability to be in the control room and with different level of knowledge of the control systems, have to cooperate to implement algorithms to achieve very challenging goals. The ATF2 Flight Simulator is a project to provise a documented and collaborative tool to make simulations or to control the real machine in a unified framework, complementary to the present control system.

All the software tools developed in the context of this thesis were implemented within the Flight Simulator.

7.1 Principle

7.1.1 Present Control System

The ATF2 control system was based on EPICS and V-SYSTEM control system with VME, CAMAC and PC-based controllers running respectively on GNU/Linux and VMS operating system. For homogeneity and to reduce license costs, it has been migrated to EPICS on GNU/Linux progressively last year. The user interface is made in Tcl/Tk, with tools to manually set the power supplies (to control, for example, magnet strengths), save the machine status, go back to a previous saved status. A gateway to the optics code SAD [34] is used to obtain a model of the ATF ring and of ATF2 beam line, to support different measurement and tuning tasks, e.g.:

- Gun and klystron timing and power adjustments,
- Kicker controls,
- Individual magnet and multi magnet knobs settings,
- View and save BPM measurements,
- Wire scanners and screen monitor measurements,
- Ring tune measurements,
- Ring beta function measurements.

The development and maintenance are subcontracted to a local company which can sometimes lead to communication problems, due to laguage skill limitations. Off-line development is moreover not easy. The present control system has for the moment insuficient automated applications and the large number of controls and menus take long to get familiarized with.

Nevertheless, this control system can control and monitor everything, from the laser gun timing up to the post-IP wire scanner.

7.1.2 The ATF2 Flight Simulator Concept

The ATF2 Flight Simulator can be used in two modes: simulation and production (using the real machine). The mode is defined at the start and both modes are designed to be equivalent for the user. This allows off-line development and tests using user-defined errors followed by very fast implementation on the real machine.

The ATF2 Flight Simulator also includes the possibilities interfacing with the user's favorite tracking or optics codes, such as MAD, SAD, PLACET [35], ... in addition to the built-in Lucretia program [36].

The ATF ring and the ATF2 extraction line and final focus are included, but as Lucretia doesn't compute periodic solutions, the ring is seen as a usual beam line, and only the last turn is simulated.

Developers are urged to use Matlab's graphical interface possibilities to create tools usable by non-specialists.

7.1.3 Architecture

The ATF2 Flight Simulator is a framework including (as shown figure 7.1):

- EPICS Input-Output Controllers (IOC) of supported devices,
- An ATF IOC module to connect with some of the native V-SYSTEM controllers,
- A module to maintain the model synchronized with the hardware,
- Parsers to export this model to various optics and tracking codes,
- The Lucretia accelerator toolbox [37] with some modified functions to use EPICS Chanel Access,
- A client communicating with the server,
- A socket server to allow additional codes to send commands and receive answer from the server.

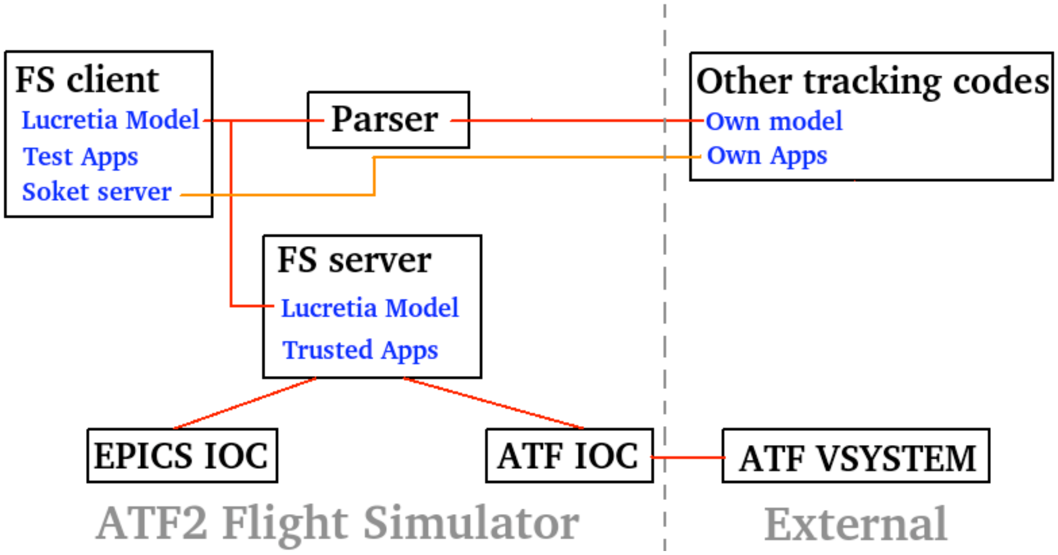

Figure 7.1: Scheme of the ATF2 Flight Simulator.

The EPICS part updates (in real time in production mode) a database of the hardware settings, associating a Process Variable (PV) to each one. When the PV value is changed, the hardware setting is changed accordingly. The Flight Simulator server, that needs to be run on the same sub-network as the EPICS in production mode, makes the correspondence between the EPICS database and the Lucretia model, and it has full access to these variables. This means the Trusted Applications which are run from the server will not need any confirmations to change hardware settings. On the other hand, as the Flight Simulator client does not need to be on the same sub-network and as it sends the hardware change requests to the server, access must be previously granted.

Lucretia, the server and the client are written in Matlab, as well as the applications developed within the ATF2 Flight Simulator framework. The Flight Simulator includes several security systems to prevent unauthorized access or exceed hardware limits.

The structures used in Lucretia, such as magnet positions and BPM readings are read from the control system in production mode, whereas these variables are set according to the results of a continuously updated Lucretia tracking in simulation mode.

In simulation mode, the Flight Simulator runs a simulated version of the EPICS IOC which makes the simulation mode look very close to the production mode.

7.2 Built-in Abilities

7.2.1 The Flight Simulator Server

The Flight Simulator server opens two windows (see figure 7.2) and a Lucretia command line (within Matlab) when it starts.

The first window, gives access to:

- The simulation settings (if started in simulation mode),
- The EPICS Control Server (ECS button), which allows access to FS functions through EPICS Process Variable channels for external programs,
- Some tools to control the clients (IP allowed, list of connected clients, disconnect selected client ...),
- The repetition rate of the simulated machine or refreshing data from the real machine,
- A selection of the lattice formats to save,
- A BPM tool allowing introducing BPM corrections such as intensity dependence, electrical offsets or scales factors,

- The trusted applications.

The second window shows the client requests and the power supplies involved. The access has to be given to a client when changing hardware settings.

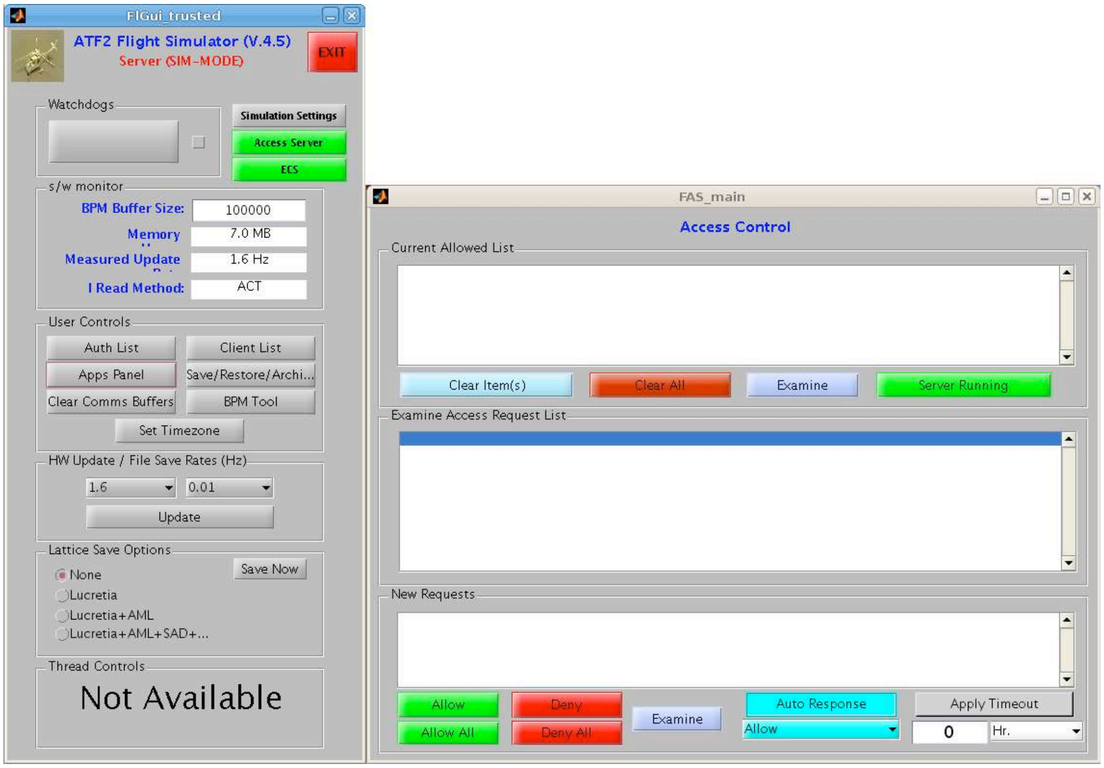

BPM Buffer Size: 100000
Memory: 7.0 MB
Measured Update: 1.6 Hz
I Read Method: ACT

HW Update / File Save Rates (Hz): 1.6 0.01

Lattice Save Options:
● None
○ Lucretia
○ Lucretia+AML
○ Lucretia+AML+SAD+...

Thread Controls: Not Available

Auto Response: Allow
Apply Timeout: 0 Hr.

Figure 7.2: The Flight Simulator server.

7.2.2 *The Flight Simulator Client*

The client side of the Flight Simulator opens a window (see figure 7.3) and a Lucretia command line (within Matlab) when it starts.

It allows to:

- Start any of the Test Applications,

ATF-steering_correction-Placet

☐ Auto Update Lattice

Update Rate: 2.0

Measured Rate: 2.6 Hz

Local Lattice Save Options
- ● None
- ○ Lucretia
- ○ Lucretia + AML
- ○ Lucretia + AML + SAD

Figure 7.3: The Flight Simulator client.

- Select the frequency of the lattice updateing from the server and the output format,
- Access the BPM tool described previously,
- Access the Beam-line Viewer tool which allows to plot Twiss parameters and beam size along selected areas of the accelerator.

7.2.3 Security and Other Issues

Security

The Flight Simulator has been built with security systems implemented at several levels.

The first layer of security is guaranteed by the ATF network being fire-walled from the KEK network in such a way that there is no direct access to/from internet. The KEK network is itself fire-walled and a VPN connection is needed to get access from outside. This prevents anyone evil-minded to have access to the ATF control system.

The second layer comes from the EPICS IOC, which has been configured in such a way that the commands allowing changes the machine settings can only come from the Flight Simulator computer.

The third layer is implemented in the Flight Simulator itself. When a Test application needs to change any hardware setting, an authorization has to be given. As mentioned before, on the Flight Simulator server, that request is displayed and, as long as the access is not granted, the requesting process is paused. For convenience, access to several PVs can be requested at once. The Trusted applications do not go through this procedure, but they are verified before being installed on the Flight Simulator trusted computer.

Other issues

As we saw, the Flight Simulator is a framework composed of multiple pieces of software interacting with multiple pieces of evolving hardwares. As it is mainly maintained by a single person, from a laboratory abroad, it is more often difficult to make the production server work in his absence.

A related concern is about the general use of the Flight Simulator. Since the ATF staff is used to work with the present control system and to interact with the company in charge when developing applications, there has been little local participation in the Flight Simulator development and usage, which raise concerns about its sustainability.

7.3 Developed Tools

A large set of tools has been developed and are now available. The most advanced and used applications developed by the collaboration are listed below, followed by a comprehensive description of the tools developed during this thesis:

- The Twiss Graphical User Interface (GUI) uses MAD [38] to compute the periodic solution of the Twiss function for the ring and propagate it through the ATF2 beam line.
- The Beam Based Alignment (BBA) tool uses movers or correctors to find the magnetic center of the quadrupoles or sextupoles.
- The Dispersion tool gets BPMs measurements for various ring frequency changes to compute dispersion corrections in ATF2.
- The Coupling Correction tool gives the skew squads strength needed to correct coupling in ATF2 based on wire scanner measurements during skew quadrupoles scans.
- The Multi-Knobs tool computes sextupole displacement knobs to adjust the beam size.
- Outside of the Flight Simulator, the calibration of the non-mover cavity BPMs uses the EPICS Control Server to get the transfer matrices between the correctors and the movers.

7.3.1 Transfer Matrix Checks

The goal of the transfer matrix check tool is to measure the R_{12}, R_{32}, R_{14} and R_{34} transfer matrix elements between the correctors and the downstream BPMs and to compare them with the on-line model of the ATF2 Flight Simulator. It was developed to help to diagnose problems with the model compared to the real machine, but it was found useful to check the BPM calibration too.

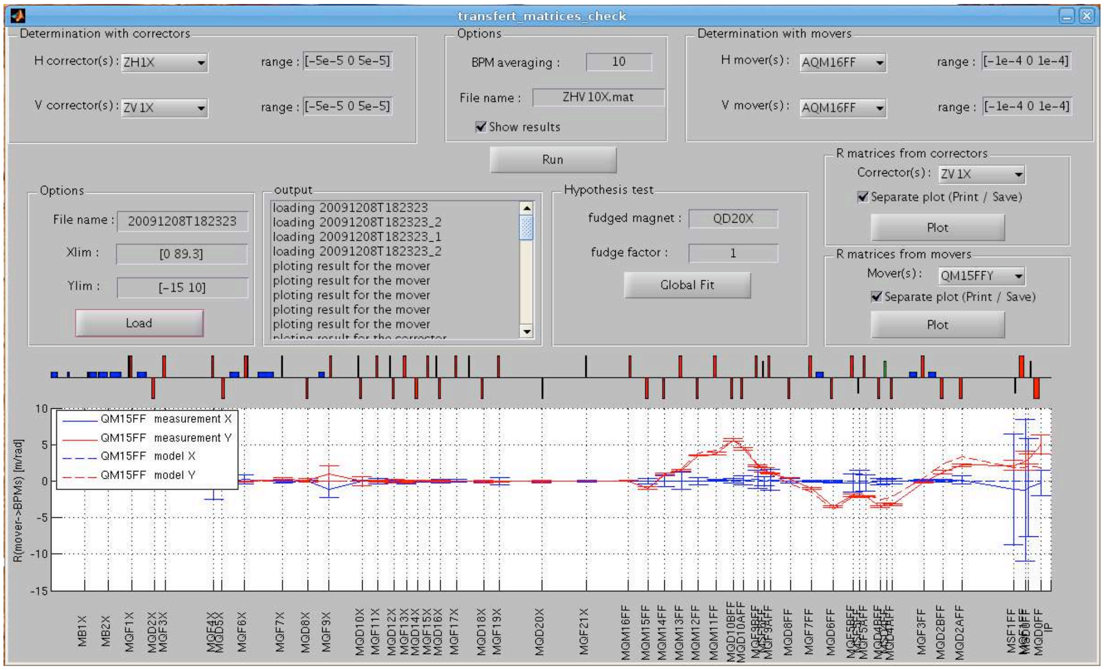

H corrector(s) : ZH1X range : [-5e-5 0 5e-5]

V corrector(s) : ZV1X range : [-5e-5 0 5e-5]

BPM averaging : 10

File name : ZHV10X.mat

☑ Show results

H mover(s) : AQM16FF range : [-1e-4 0 1e-4]

V mover(s) : AQM16FF range : [-1e-4 0 1e-4]

File name : 20091208T182323

Xlim : [0 89.3]

Ylim : [-15 10]

```
loading 20091208T182323
loading 20091208T182323_2
loading 20091208T182323_1
loading 20091208T182323_2
ploting result for the mover
ploting result for the mover
ploting result for the mover
ploting result for the mover
ploting result for the mover
ploting result for the corrector
```

fudged magnet : QD20X

fudge factor : 1

Corrector(s) : ZV1X

☑ Separate plot (Print / Save)

Mover(s) : QM15FFY

☑ Separate plot (Print / Save)

Figure 7.4: The Transfer Matrix Check tool.

As one can see from the figure 7.4, it is composed of 3 areas:

- The top one, which is for data acquisition, allows to select the corrector(s) or the mover(s) which one wants to use, with respectively the corresponding angles or displacements introduced at each step and even how many BPM readings are recorded at each step. Pressing the Run button, the correctors changes successively all the angles and movers displacements by the specified amount and results are saved.

- The middle one, which can be run off-line, displays options and the output of the current process. Once the file has been loaded, the corrector or mover, from which the transfer matrices are displayed, can be selected, as well as the plot range. It is also possible to choose to select a separate plot for printing or saving figures. It includes also a possibility to apply a coefficient (fudge factor) to a selected magnet in the model to test hypothesis of a given element causing an observed mismatch between the model and the measurements.

- The one in the bottom, used when the Plot button is pressed and the Separate plot option is deactivated, shows for each BPM the horizontal results in blue (R_{12} for an horizontal corrector or mover displacement or R_{14} for an vertical corrector or mover displacement) and vertical in red (R_{32} for an horizontal corrector or mover displacement or R_{34} for an vertical corrector or mover displacement). The dashed lines in the same colors represent the corresponding model predictions.

7.3.2 Trajectory Correction

The Trajectory Correction tool allows automatized steering to a reference trajectory specified by the user. The Graphical User Interface (GUI) is shown figure 7.5.

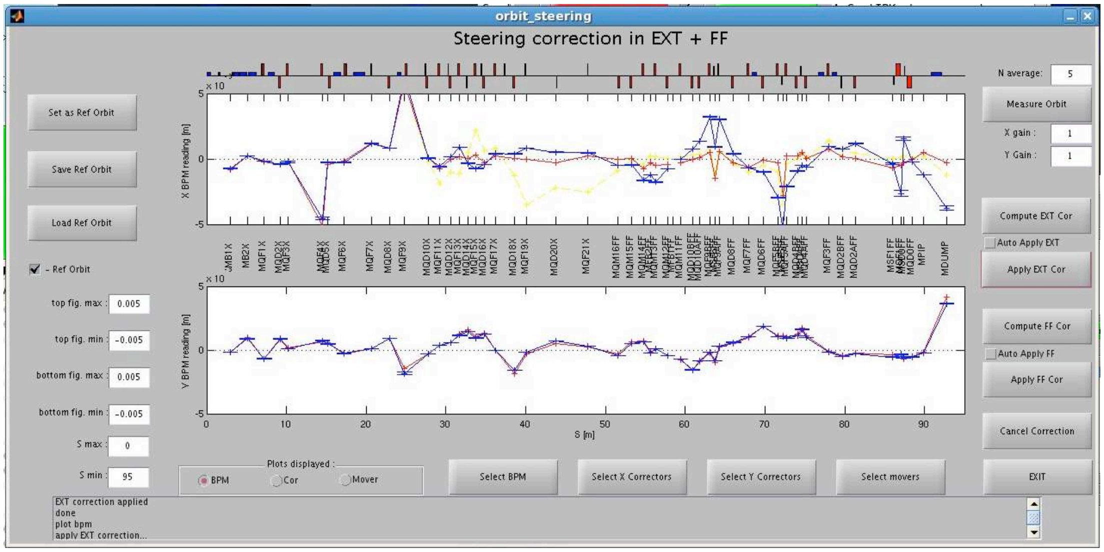

N average: 5

X gain : 1

Y Gain : 1

☑ - Ref Orbit

top fig. max : 0.005

top fig. min : -0.005

bottom fig. max : 0.005

bottom fig. min : -0.005

S max : 0

S min : 95

Plots displayed : ● BPM ○ Cor ○ Mover

EXT correction applied
done
plot bpm
apply EXT correction...

Figure 7.5: The Trajectory Correction tool.

The current trajectory can be set as reference and saved or loaded from previous measurements. It is also possible to select the BPMs, the correctors and the movers to use. The usual steps for the correction are:

- Measuring the trajectory (with a customizable average number of pulses). It is displayed in blue.

- Computing a correction (in the Extraction line using the correctors or in the final focus using the movers). The estimated trajectory after correction is displayed in red. The difference between the measured and the reference orbit is multiplied by the gain value, which can be changed in case of iterated corrections.

- Applying the correction. The trajectory before correction is displayed in yellow and the measurement after correction is a blue line.

Before applying the correction, one can look at the correctors' and movers' present values in blue and at the prediction for the correction in red, looking for saturations. One can also come back to the status before every correction thanks to the cancel correction button.

7.3.3 Trajectory Reconstruction and Dispersion Measurement

The trajectory Reconstruction and Dispersion Measurement tool allows the reconstruction of the ($x\ x'\ y\ y'\ \frac{\Delta E}{E}$) parameters at a selected point by fitting a selected set of BPM measurements (see section 8.3.1). From the energy variation reconstructed and the measurement at selected BPMs, the dispersion can then also be fitted at the selected point and propagated along all the line.

This tool is also composed of 3 sections as shown figure 7.6:

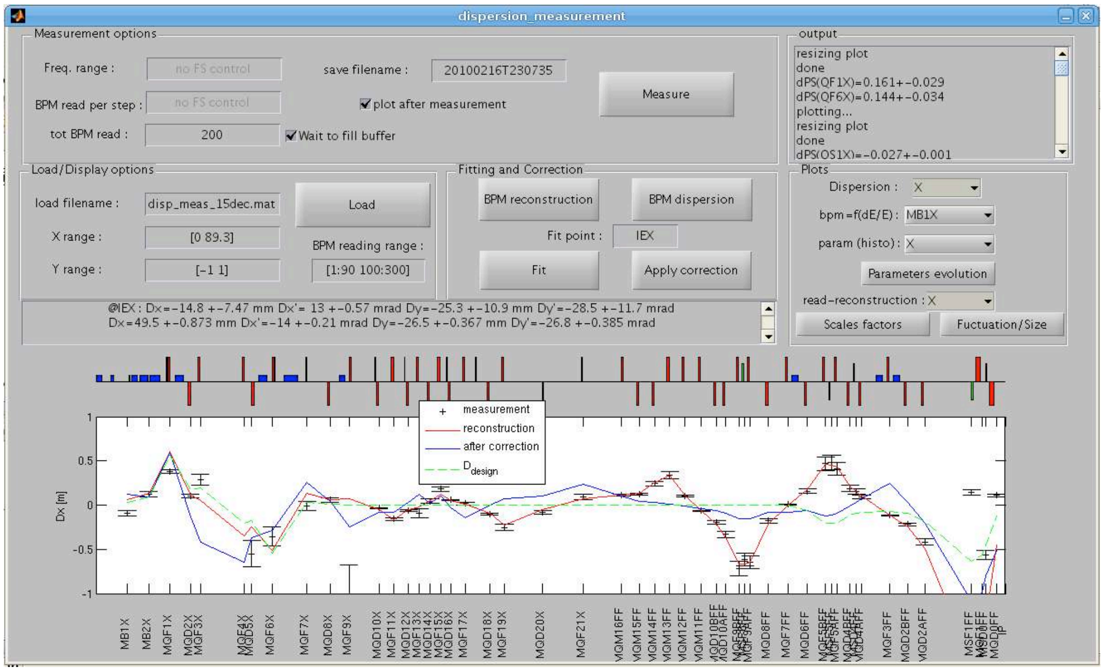

Freq. range : no FS control

BPM read per step : no FS control

tot BPM read : 200

save filename : 20100216T230735

☑ plot after measurement

☑ Wait to fill buffer

```
resizing plot
done
dPS(QF1X)=0.161+-0.029
dPS(QF6X)=0.144+-0.034
plotting...
resizing plot
done
dPS(OS1X)=-0.027+-0.001
```

load filename : disp_meas_15dec.mat

X range : [0 89.3]

Y range : [-1 1]

BPM reading range : [1:90 100:300]

Fit point : IEX

Dispersion : X

bpm=f(dE/E) : MB1X

param (histo) : X

read-reconstruction : X

```
@IEX : Dx=-14.8 +-7.47 mm Dx'= 13 +-0.57 mrad Dy=-25.3 +-10.9 mm Dy'=-28.5 +-11.7 mrad
Dx=49.5 +-0.873 mm Dx'=-14 +-0.21 mrad Dy=-26.5 +-0.367 mm Dy'=-26.8 +-0.385 mrad
```

Figure 7.6: The Trajectory Reconstruction and Dispersion Measurement tool.

- The top zone is for data acquisition. As the ring frequency cannot be controlled yet by the flight simulator, only the number of BPM readings to save and the file name can be chosen. The output of the current process is also displayed here.

- The middle zone is for the analysis of the data measured. The specified file can be loaded giving access to the selection of the BPMs utilized for the trajectory reconstruction and for the dispersion fit. Now it is possible to launch the fit of the parameters and of the dispersion at the given fit point with the fit button. Dispersion correction is also computed and can be applied with the button "apply correction".

- The bottom zone controls the displaying of plots showing the results. Several can be selected as:

- The propagation of the fitted dispersion (in red) with individual measurement in black, the design dispersion in green and the estimated dispersion after correction in blue.
- For the selected BPM, the correlation plot of the measurement function of the reconstructed energy variation.
- The histogram of the selected parameter.
- The evolution of the reconstructed parameters.
- The spread of the residuals corresponding to the readings minus the fitted trajectories are displayed in red and compared with the BPM resolutions (in blue) and with the spread of the measurement (in green).
- An evaluation of the BPMs scales factors.
- The amplitude of the fluctuations compared to the beam size

Chapter 8

EXPERIMENTAL RESULTS

8.1 Transfer Matrix Measurements

The knowledge of the transfer matrices are the basis of any beam orbit related work. At the beginning of the commissioning, the first step was to check if the modeled and experimental transfer matrices matched.

The procedure to verify that match is easy to implement as it consists in measuring the orbit variation when a kick is introduced. This kick can be produced by using a corrector magnet, by changing a bit the strength of a dipole magnet or even by displacing a quadrupole mounted to a magnet mover. The R_{12}, R_{32}, R_{14} and R_{34} elements of the transfer matrices between the point of the kick and the BPMs represent the ratios of the resulting displacements measured in the BPMs downstream over the introduced kick angle (see section A.2):

$$\begin{aligned}
R_{12}(\textbf{kick} \rightarrow \textbf{BPM}) &= \frac{X_{\text{before}}(\text{BPM})-X_{\text{after}}(\text{BPM})}{X'_{\text{before}}(\text{kick})-X'_{\text{after}}(\text{kick})} \\
R_{14}(\textbf{kick} \rightarrow \textbf{BPM}) &= \frac{X_{\text{before}}(\text{BPM})-X_{\text{after}}(\text{BPM})}{Y'_{\text{before}}(\text{kick})-Y'_{\text{after}}(\text{kick})} \\
R_{32}(\textbf{kick} \rightarrow \textbf{BPM}) &= \frac{Y_{\text{before}}(\text{BPM})-Y_{\text{after}}(\text{BPM})}{X'_{\text{before}}(\text{kick})-X'_{\text{after}}(\text{kick})} \\
R_{34}(\textbf{kick} \rightarrow \textbf{BPM}) &= \frac{Y_{\text{before}}(\text{BPM})-Y_{\text{after}}(\text{BPM})}{Y'_{\text{before}}(\text{kick})-Y'_{\text{after}}(\text{kick})}
\end{aligned} \tag{8.1}$$

The horizontal and vertical measurements are synchronized for all the BPMs. We average over 10 pulses using the following quality cuts to get a good precision to exclude bad experimental measurements with:

- intensities lower than the half of the average intensity,
- very large ($> 5cm$) or exactly zero readings,

- horizontal and vertical positions beyond three standard deviations of the distribution.

Instead of only comparing the measurement with and without a kick, the measurement is done for a positive, a null and a negative kick, to detect systematic errors like beam loss somewhere in the beam line. The fit of the slope of the position function of the angle induced and the spread of the measurements permits to estimate respectively the transfer matrix elements and their uncertainties.

The figure 8.1 displays the results of the comparison between the measured transfer matrices elements, obtained using ZH4X and ZV8X correctors and the equivalent matrix elements obtained from the model. As explained in chapter 4, the cavity BPMs are much more precise than the stripline BPMs and consequently the error bars on the stripline BPMs measurements are larger than on the cavity BPMs. As MS1FF, MQF1FF, MS0FF and MQD0FF (the four S-band BPMs attached to the final doublet magnets) were not working we can ignore the measurements at these BPMs. An example of the same kind of comparison is displayed figure 8.2 for a vertical displacement of the QM15FF quadrupole. The measurement represents the ratio between the measured displacement at each downstream BPM and the displacement of QM15FF. As the MQM15FF BPM is attached to that quadrupole, the displacement measured in MQM15FF must be the opposite to the displacement of the quadrupole, so we expect a ratio of -1.

The measurement procedure and the display of the result have been integrated into a Flight Simulator application, allowing making the measurements, to save the data for further analysis, to load them, to display the results (see fig. 8.3 and section 7.3.1).

As these measurements are very quick to get (three minutes for a corrector

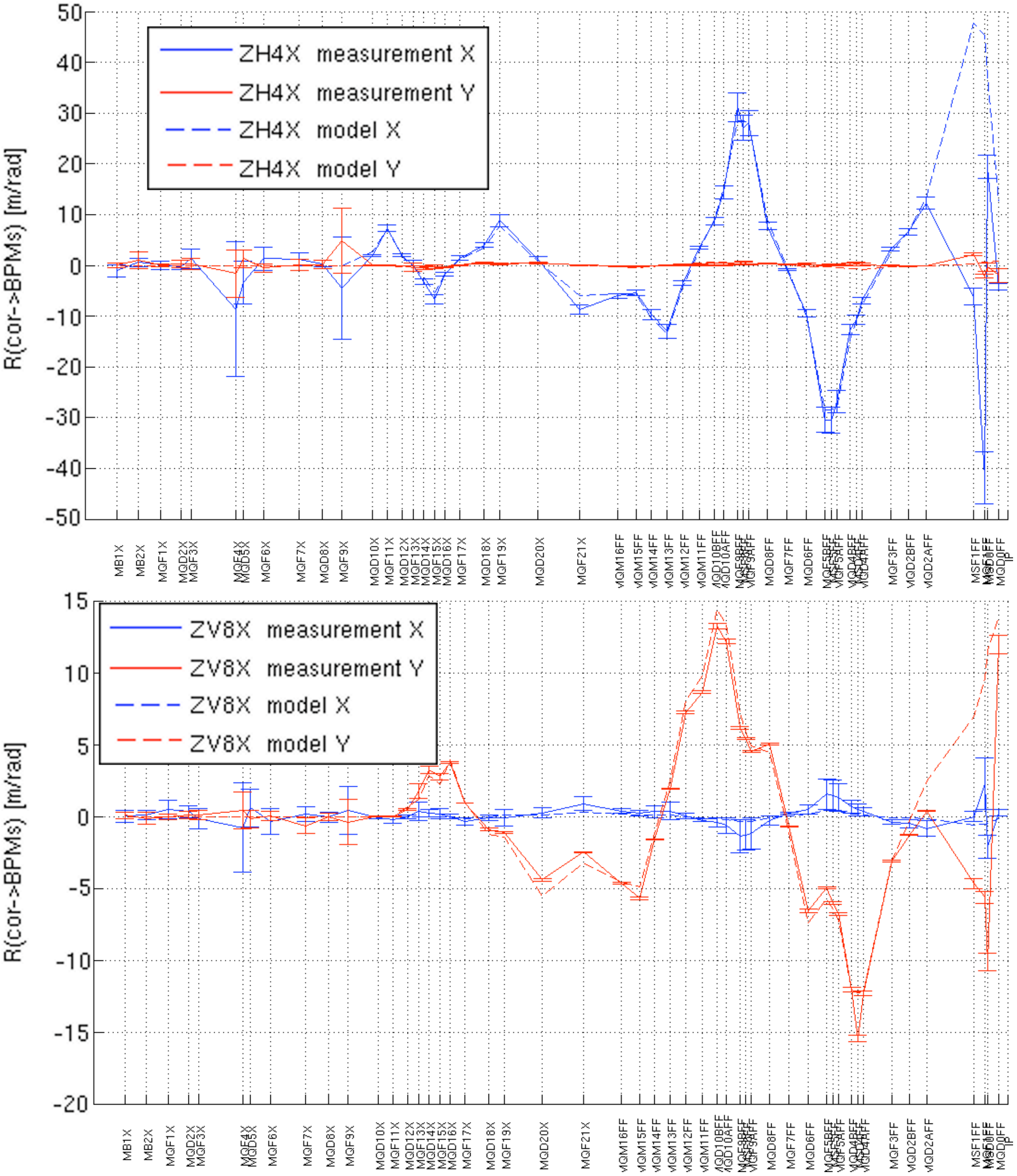

Figure 8.1: Comparison of measured transfer matrices between ZH4X and ZV8X correctors and all BPMs with the optics model reconstructed from the currents of the magnets.

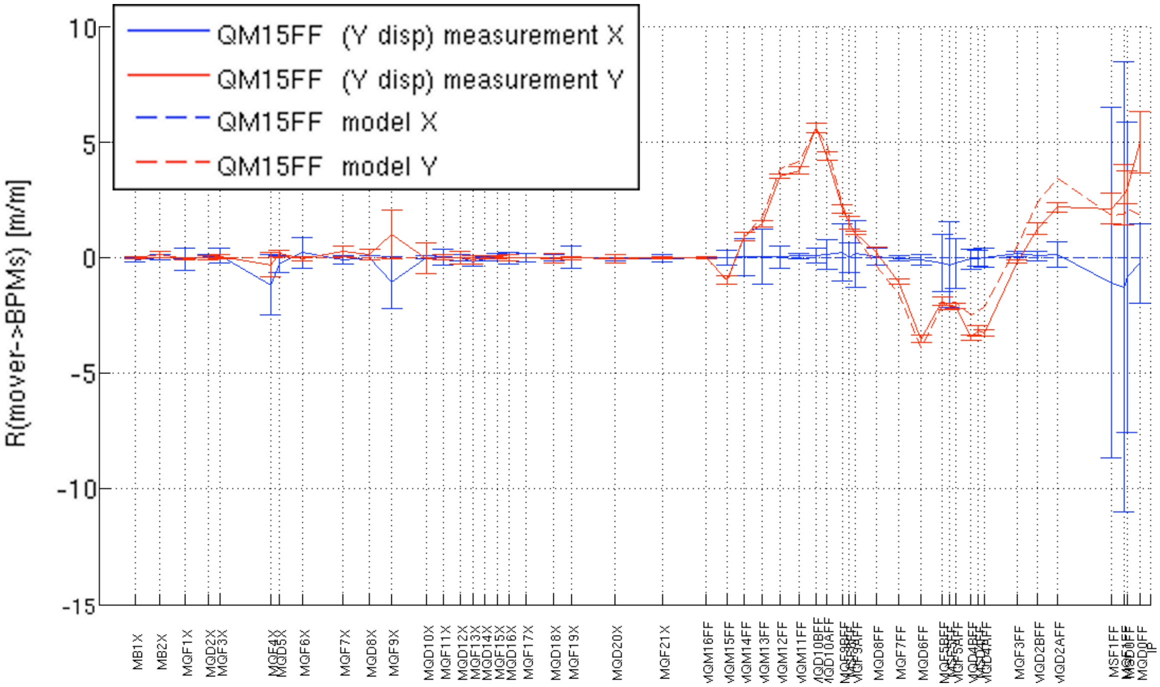

Figure 8.2: Comparison between the displacement measured in all BPM, normalized to the vertical displacement of the QM15FF mover, and the model prediction.

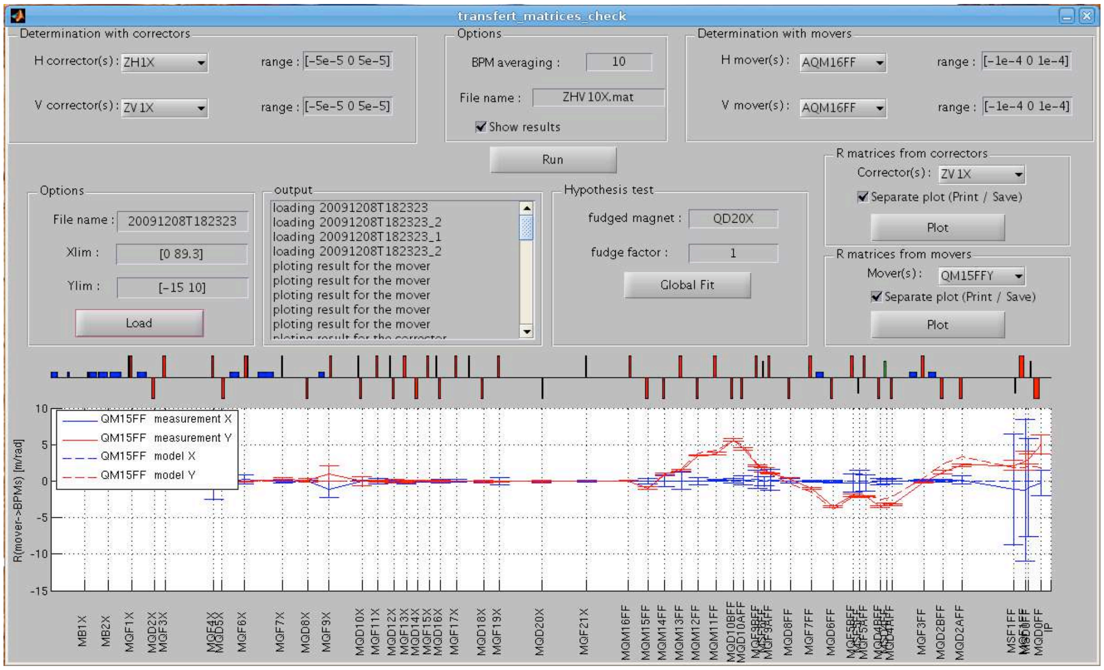

H corrector(s) : ZH1X range : [-5e-5 0 5e-5]

V corrector(s) : ZV1X range : [-5e-5 0 5e-5]

BPM averaging : 10

File name : ZHV10X.mat

☑ Show results

H mover(s) : AQM16FF range : [-1e-4 0 1e-4]

V mover(s) : AQM16FF range : [-1e-4 0 1e-4]

Corrector(s) : ZV1X

☑ Separate plot (Print / Save)

File name : 20091208T182323

Xlim : [0 89.3]

Ylim : [-15 10]

```
loading 20091208T182323
loading 20091208T182323_2
loading 20091208T182323_1
loading 20091208T182323_2
ploting result for the mover
ploting result for the mover
ploting result for the mover
ploting result for the mover
ploting result for the mover
```

fudged magnet : QD20X

fudge factor : 1

Mover(s) : QM15FFY

☑ Separate plot (Print / Save)

Figure 8.3: The transfer matrix diagnostic tool interface in the Flight Simulator environment.

or a mover), this tool has been extensively used to check the model of the beam line. This tool helped to:

- Determine the coordinate system of all BPMs, correctors and movers. At the beginning of commissioning (February 2009), as all these subsystems had just been integrated into the Flight Simulator, discrepancies existed between the different orientations used, resulting in a number of sign errors in the measured transfer matrices.

- To figure out why there were sometimes discrepancies between the measurements and the model when correctors were used at the very beginning of the beam line. It was later understood (in October 2009) that the Flight Simulator should use DAC (magnets intensity set values) instead of ADC (read-back of these intensities) to get the currents as the latter are much less precise for the old magnet power supplies in the extraction line.

- Check the modeling of the beam line and the cavity BPMs calibrations at the beginning of each optics tuning shift.

- Determine the sections where the transfer matrices were good enough to be used by other tools (steering correction, orbit reconstruction).

This tool has been used successfully for basic testing of the optics. As this tool uses the linear optics formalism, the effects of the sextupoles are not included, hence introducing some level of systematic error at the end of the final focus.

A sextupole can be approximated as a quadrupole with a strength proportional to the distance from the center so, to implement in the future the sextupole effect, we can simply use the readings of the BPM attached to that sextupole to infer the equivalent quadrupole strength for that beam position.

When discrepancies between the model and the measurements are found, our tool includes the possibility to test different hypotheses for quadrupoles strength errors. Nevertheless, it is an cumbersome procedure because multiple successive tests with different quadrupole and level of errors are needed. Automation of that procedure would make it more convenient.

A future possible prospect would be to get a quantitative measurement of errors in the transfer matrices which, combined with tolerance determinations for the algorithms which use these transfer matrices, would give clear criteria on the validity of the modeling. It could also be extended to diagnose sextupole's alignment and strength as well as quadrupole roll errors when the cavity BPMs will work at their design resolutions.

8.2 Static Trajectory Correction

Once we are confident with the transfer matrices, we can try to correct the trajectory to the reference trajectory determined by BBA. Up to now, the validity of the transfer matrices has been checked essentially qualitatively

8.2.1 Principle of the Average Trajectory Correction

Due to the mismatch at the injection and the misalignment of the magnets (resulting in kicks and relative displacements), the beam does not go through the magnet centers. That can cause distortion of the beam phase space and even halo creation which can become a source of background near the IP when there are high order multi-polar magnetic fields. To avoid that, the beam trajectory must be corrected to minimize displacement compared to a reference determined by Beam Based Alignment. That implies the use of corrector magnets and quadrupole movers to steer the beam.

By definition of the transfer matrices between a corrector and a BPM (equation A.3) we have:

$$\begin{pmatrix} \Delta x(BPM) \\ \Delta y(BPM) \end{pmatrix} = \begin{pmatrix} R_{12}(\text{cor} \rightarrow \text{BPM}) & R_{14}(\text{cor} \rightarrow \text{BPM}) \\ R_{32}(\text{cor} \rightarrow \text{BPM}) & R_{34}(\text{cor} \rightarrow \text{BPM}) \end{pmatrix} \times \begin{pmatrix} \theta_x(\text{cor}) \\ \theta_y(\text{cor}) \end{pmatrix} \tag{8.2}$$

The result of the expansion of this relation to all n correctors and m BPMs is shown equation 8.3.

Let's call M this big matrix which gives the displacements in the BPMs function of the angles of the correctors. That equation takes into account the coupling (R_{14} and R_{23} terms). $R_{kl}(i \rightarrow j) = 0$ when $s(\text{cor}_i) > s(\text{BPM}_j)$ since a corrector has no influence on the orbit upstream.

$$\text{with } R_{kl}(i \rightarrow j) = \begin{cases} R_{kl}(\mathbf{cor}_i \rightarrow \mathbf{BPM}_j) \text{ if } s(\mathbf{cor}_i) < s(\mathbf{BPM}_j) \\ 0 \text{ otherwise} \end{cases}$$

$$\begin{pmatrix} \Delta x(\mathbf{BPM}_1) \\ \vdots \\ \Delta x(\mathbf{BPM}_m) \\ \Delta y(\mathbf{BPM}_1) \\ \vdots \\ \Delta y(\mathbf{BPM}_m) \end{pmatrix} = \begin{pmatrix} R_{12}(1 \rightarrow 1) & \cdots & R_{12}(n \rightarrow 1) & R_{14}(1 \rightarrow 1) & \cdots & R_{14}(n \rightarrow 1) \\ & \vdots & & & \vdots & \\ R_{12}(1 \rightarrow m) & \cdots & R_{12}(n \rightarrow m) & R_{14}(1 \rightarrow m) & \cdots & R_{14}(n \rightarrow m) \\ R_{32}(1 \rightarrow 1) & \cdots & R_{32}(n \rightarrow 1) & R_{34}(1 \rightarrow 1) & \cdots & R_{34}(n \rightarrow 1) \\ & \vdots & & & \vdots & \\ R_{32}(1 \rightarrow m) & \cdots & R_{32}(n \rightarrow m) & R_{34}(1 \rightarrow m) & \cdots & R_{34}(n \rightarrow m) \end{pmatrix} \times \begin{pmatrix} \theta_x(\mathbf{cor}_1) \\ \vdots \\ \theta_x(\mathbf{cor}_n) \\ \theta_y(\mathbf{cor}_1) \\ \vdots \\ \theta_y(\mathbf{cor}_n) \end{pmatrix} \quad (8.3)$$

Finding the correction of the trajectory corresponds to figuring out the value of the angle introduced at the correctors and the displacement of the quadrupole on movers to displace the orbit at each BPM by an amount as close as possible of :

$$\begin{aligned} -\Delta x(\mathbf{BPM}) &= X_{\text{ref}}(BPM) - X_{\text{measured}}(BPM) \\ -\Delta y(\mathbf{BPM}) &= Y_{\text{ref}}(BPM) - Y_{\text{measured}}(BPM) \end{aligned}$$

That is equivalent to solving the inverse problem of the equation 8.3 for the opposite displacement observed. A proportional factor $\alpha \leqslant 1$ can also be added to optimize the convergence when the algorithm is used iteratively in presence of large errors.

$$\begin{pmatrix} \theta_x(\mathbf{cor}_1) \\ \vdots \\ \theta_x(\mathbf{cor}_n) \\ \theta_y(\mathbf{cor}_1) \\ \vdots \\ \theta_y(\mathbf{cor}_n) \end{pmatrix}_{\text{correction}} = M^{-1} \cdot \begin{pmatrix} -\alpha\Delta x(\mathbf{BPM}_1) \\ \vdots \\ -\alpha\Delta x(\mathbf{BPM}_m) \\ -\alpha\Delta y(\mathbf{BPM}_1) \\ \vdots \\ -\alpha\Delta y(\mathbf{BPM}_m) \end{pmatrix} \tag{8.4}$$

This solution is found by least square minimization. The expected orbit variation after correction is:

$$\begin{pmatrix} -\Delta x(\mathbf{BPM}_1) \\ \vdots \\ -\Delta x(\mathbf{BPM}_m) \\ -\Delta y(\mathbf{BPM}_1) \\ \vdots \\ -\Delta y(\mathbf{BPM}_m) \end{pmatrix}_{\text{expected}} = M \cdot \begin{pmatrix} \theta_x(\mathbf{cor}_1) \\ \vdots \\ \theta_x(\mathbf{cor}_n) \\ \theta_y(\mathbf{cor}_1) \\ \vdots \\ \theta_y(\mathbf{cor}_n) \end{pmatrix}_{\text{correction}} \tag{8.5}$$

Quadrupoles on movers can also be used since the kick θ_x induced by the displacement Δx_{quad} of a quadrupole of strength K and of length L is $\theta_x = KL\Delta x_{quad}$.

A difficulty in the implementation of this algorithm is dealing with the maximum angles available from the correctors (due to maximum currents or other limitations) or the quadrupole on movers (due to maximum displacements).

One way to deal with that is to iterate the following algorithm:

1. compute the solution.
2. look for the first corrector above the limit.
3. subtract from the measured trajectory the effect of setting that corrector at its limit.
4. set that corrector at its limit and remove it from further computations.

8.2.2 Simulation Results

For the simulations of the algorithm performances, errors are introduced on several parameters (see table 8.1).

Error Type	Level
x/y/z Post-Survey	$200\mu m$
Roll Post-Survey	$300\mu rad$
BPM - Magnet alignment (post-BBA, if BBA not simulated) (x, y)	10 um
Relative Magnetic field strength (dB/B)	1e-4
C/S - band BPM nominal resolution (x, y)	100 nm
Stripline BPM nominal resolution (x, y)	10 um
IP BPM nominal resolution (x, y)	2 nm
Corrector magnet pulse-pulse relative field jitter	1e-4

Table 8.1: Table of the set of errors parameters take into account in the simulation

These errors have been agreed by the collaboration to be realistic and to be uses in everyone's simulations,in order to get comparable results.

To determine the trajectory, ten pulses are averaged and three steps in the correction are made. These are:

1. Correction in the extraction line (using only correctors and BPM in the extraction line).

2. Correction in the final focus using the last correctors of the extraction line and the BPMs of the final focus.

3. Correction of the final focus using the movers

The second step is needed to adjust the launch into the final focus and thus limit the displacements of the movers in the third step.

In figure 8.4 are displayed the correction's results obtained from 100 different random settings using the nominal optics and the standard errors agreed upon (see table 8.1). The value on the abscissa is the root mean square of the orbit displacement ($\mathrm{RMS}_X = \sqrt{\sum^{\mathrm{BPM}} \frac{\Delta X^2}{N_{BPM}}}$) in the specified section (extraction line, final focus or the entire line). The color is blue before any correction, green after the correction in the extraction line (step 1) and red after all the corrections.

The algorithm seems to be very efficient, but the mismatch in the injection into the extraction line from the ring is not taken into account.

The BPM errors were then increased by a factor 50 and the magnets strength errors up to 5% to test the performance of the algorithm, with very large errors as those expected at the first stage of the commissioning. To get the same kind of results as before, five iterations of each correction step were needed. The results for such large errors and using the nominal optics are displayed in figure 8.5.

Finally, as the very beginning of the commissioning was performed using a large β optics (see section 6.5), the algorithm has been tested in that configu-

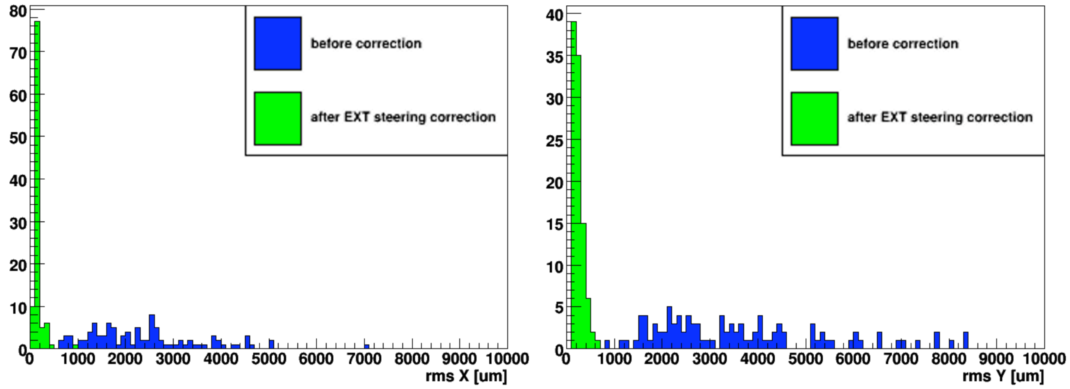

(a) RMS of horizontal displacement in EXT (b) RMS of vertical displacement in EXT

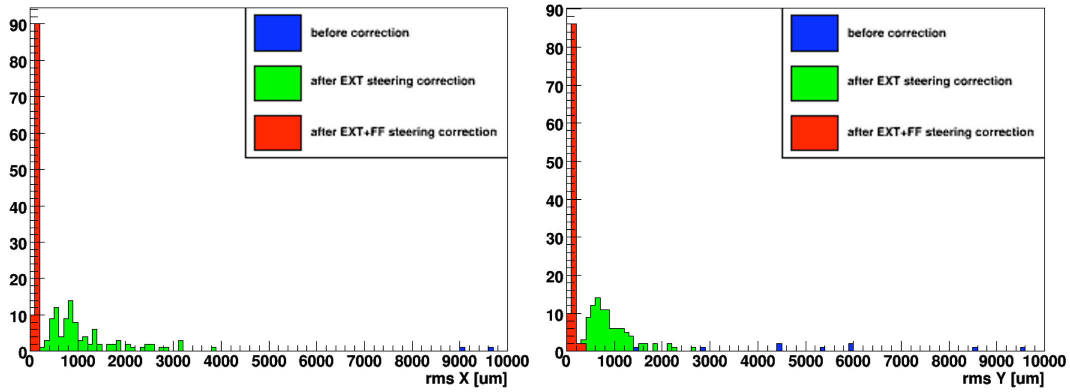

(c) RMS of horizontal displacement in FF (d) RMS of vertical displacement in FF

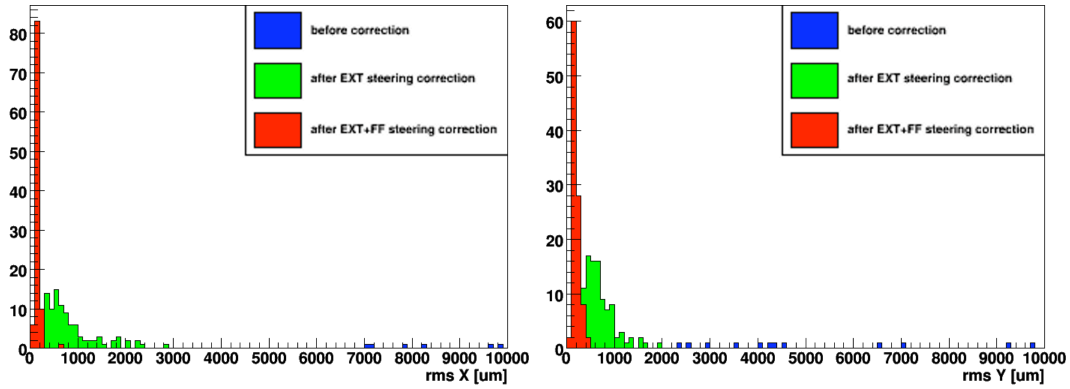

(e) RMS of horizontal displacement all line long (f) RMS of vertical displacement all line long

Figure 8.4: Result of the steering algorithm with nominal errors and optics.

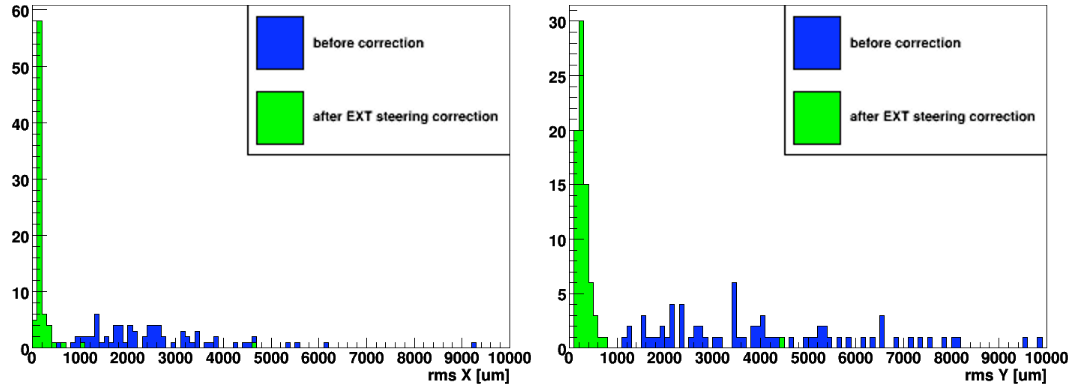

(a) RMS of horizontal displacement in EXT (b) RMS of vertical displacement in EXT

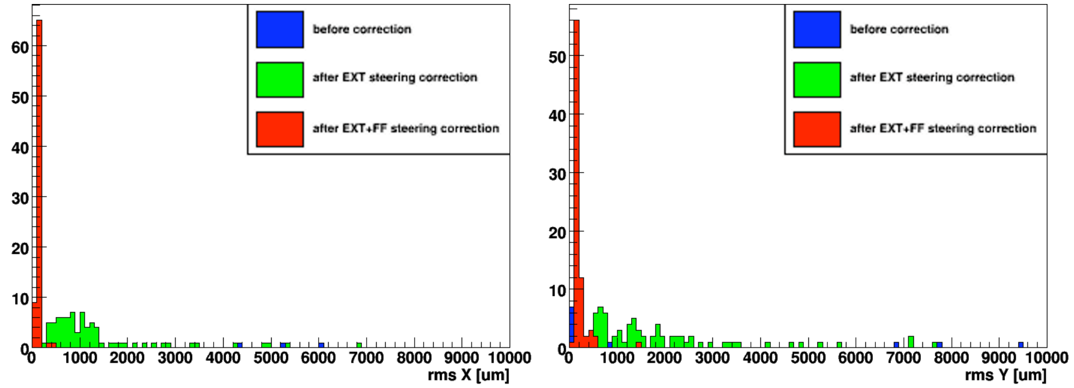

(c) RMS of horizontal displacement in FF (d) RMS of vertical displacement in FF

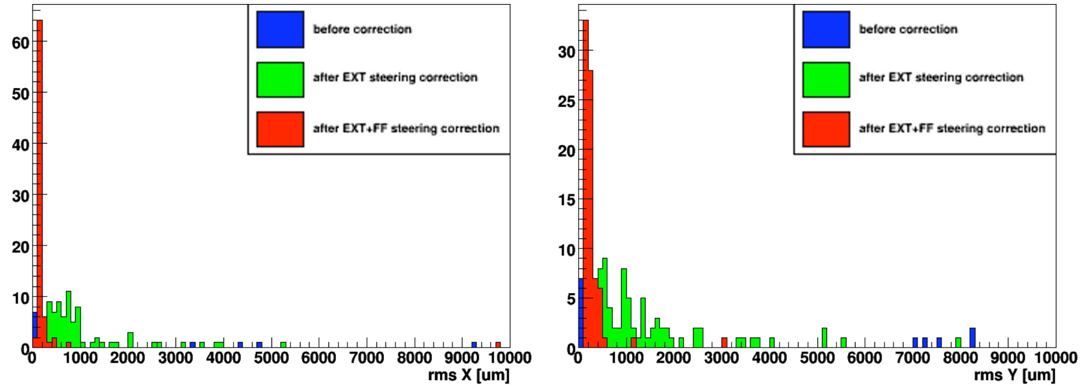

(e) RMS of horizontal displacement all line long (f) RMS of vertical displacement all line long

Figure 8.5: Result of the steering algorithm with large errors and nominal optics.

ration with the large errors. Five iterations were made at each correction step and the results are displayed in figure 8.6.

The performance in simulation is summarized in table 8.2 and compared to the experimental results presented in the next section.

optical config.	error level	iterations	RMS [mm]			
			EXT X	EXT Y	FF X	FF Y
nominal	nominal	1	0.2	0.3	0.2	0.2
	large	5	0.2	0.3	0.2	0.2
high β	large	5	0.5	0.5	0.2	0.2
high β	experimental	5 for EXT 1 for FF (Y only)	0.4	0.2	0.6	0.15

Table 8.2: Simulation results of the steering algorithm in the EXT and FFS for different error levels and optical configurations. Results of the experimental correction presented in section 8.2.3 are given for comparison purpose. As the experimental EXT correction was done downstream of MQF11X, only the BPMs downstream have been included in the corresponding RMS calculations. Sextupoles BPMs were also excluded as the BBA has not yet been done for these BPMs. The S-band BPMs in the final doublet were excluded as well because they were not working.

8.2.3 Experimental Correction

As soon as BPMs became available, and after transfer matrices had been successfully checked, our algorithm for steering corrections could be tested at ATF2. Very promising first results were obtained, even if sometimes, when several corrector settings were changed at the same time, one of them got an unexpected value.

For instance, when correctors are not properly set, one can observe very different orbit compared to the expected one. In such cases, the correction was canceled and applied again. The origin of the problem was not yet, fixed at the

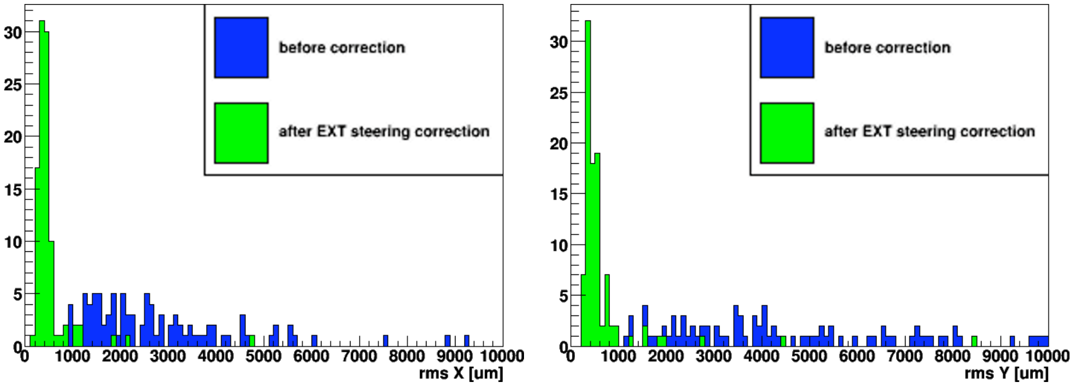

(a) RMS of horizontal displacement in EXT (b) RMS of vertical displacement in EXT

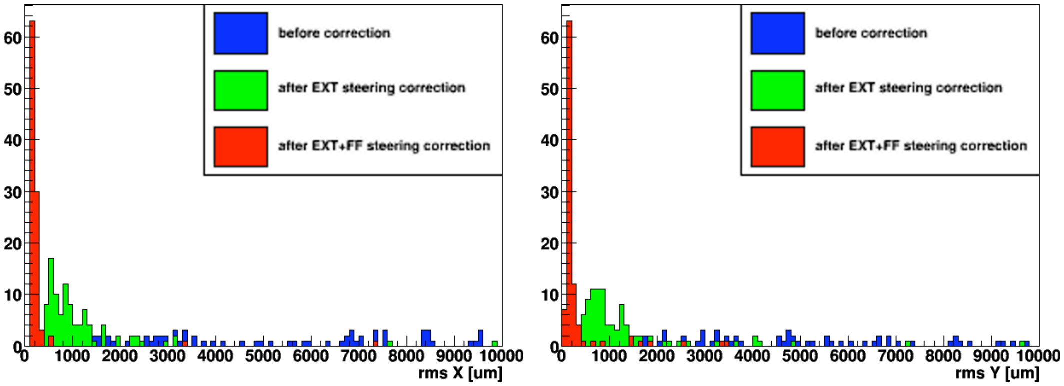

(c) RMS of horizontal displacement in FF (d) RMS of vertical displacement in FF

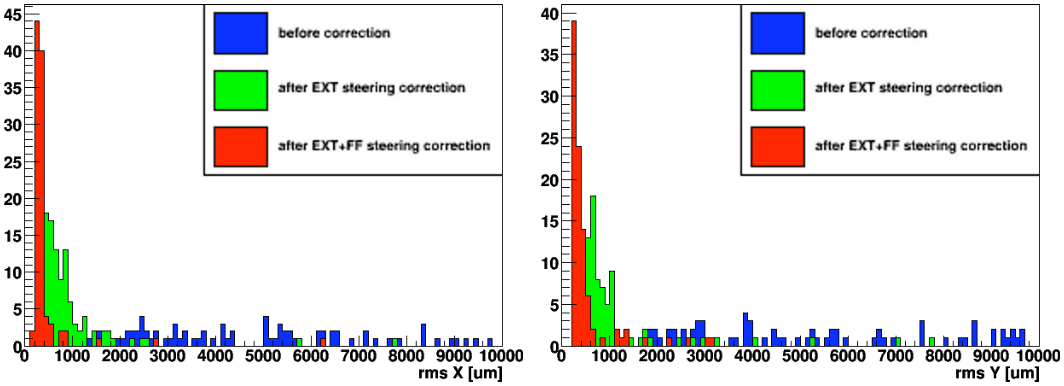

(e) RMS of horizontal displacement all line long (f) RMS of vertical displacement all line long

Figure 8.6: Result of the steering algorithm with large errors and high beta optics.

time of this writing. It may result from communication problems between the Flight Simulator and EPICS which control the corrector power supplies.

The figures from 8.7 to 8.12 show the evolution of the orbit during the experimental corrections. As the model transfer matrices were not correct at the very beginning of the line, the steering started from MQ11X BPM. Also, as no reference trajectory had been recorded through careful beam based alignment, the reference trajectory used was the orbit passing through the geometric centers of the BPMs. The alignment of the BPMs with respect to the magnets was good to a few hundred microns, except for BPMs attached to the sextupoles, so these sextupole BPMs as well as the four S-band cavity BPMs at the end of the beam line (which were not yet operational) were not used for the correction.

The steering in the extraction line worked very well in these first tests, even if some iterations were needed due to some scale errors on the non-mover cavity BPMs. In the final focus section, the horizontal correction was bad, limited by the range of the movers; some additional steering with upstream correctors could have helped. This horizontal correction was not applied but the vertical steering which showed no saturation problem was successful (see figure 8.12).

The RMS of the displacements after correction was decreased down to $0.5mm$ in horizontal and $0.2mm$ in vertical, which is very close to the expectations from simulations without mover corrections for horizontal and with full correction for the vertical (see table 8.2).

8.3 Trajectory Fluctuation Reconstruction

Cavity BPMs are expected to have (using attenuators to increase their dynamic range) below $1\mu m$ pulse to pulse resolution while the beam fluctuation amplitude is aimed to be around $\frac{1}{10}$ of the beam size. As the beam size is above $10\mu m$ in most of the BPMs, it is possible to reconstruct the pulse to pulse fluctuation of the beam trajectory.

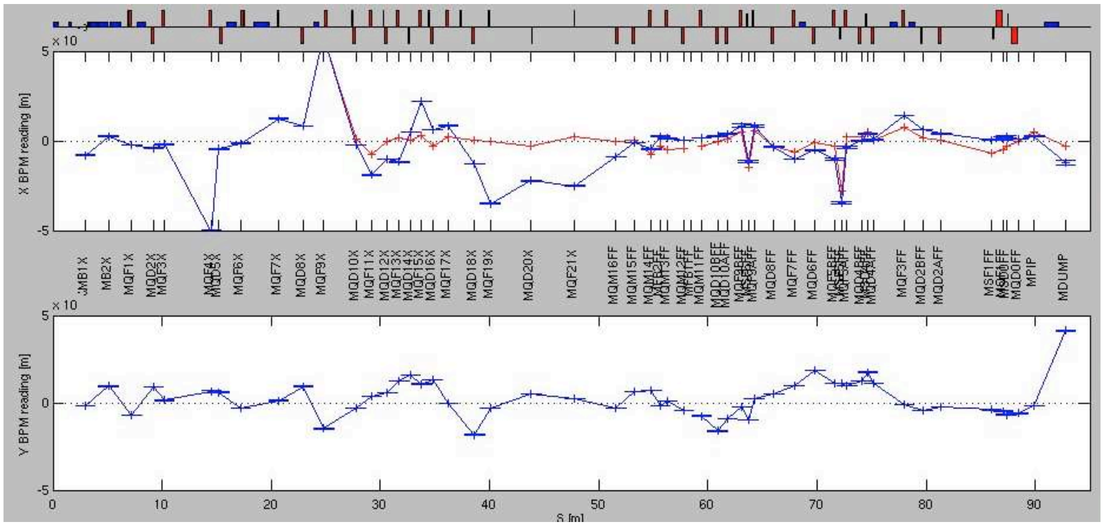

(a) orbit before 1st correction

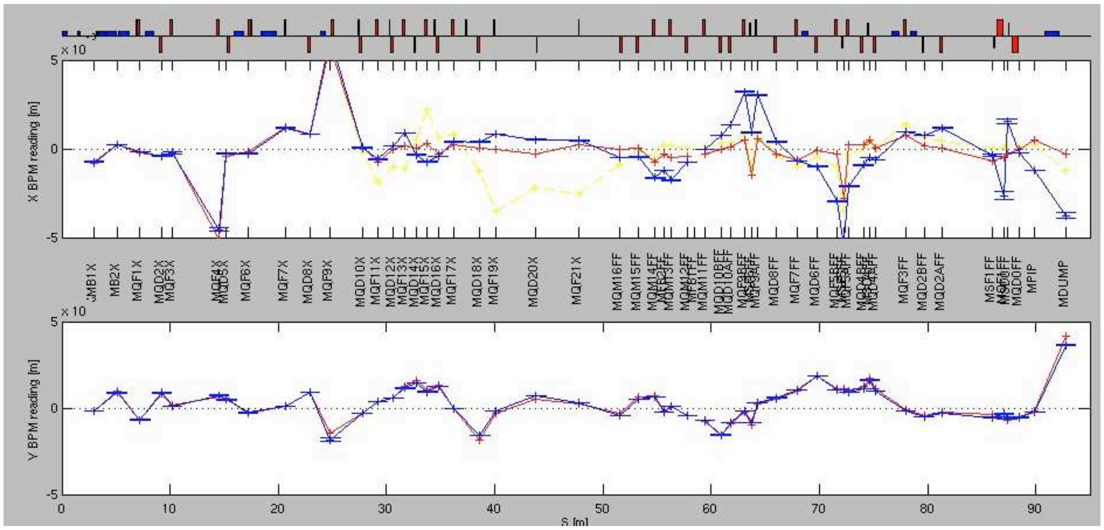

(b) orbit after 1st correction

Figure 8.7: Result of first experimental horizontal steering (in blue: orbit reading, in red: predicted orbit after correction, in yellow: orbit before correction).

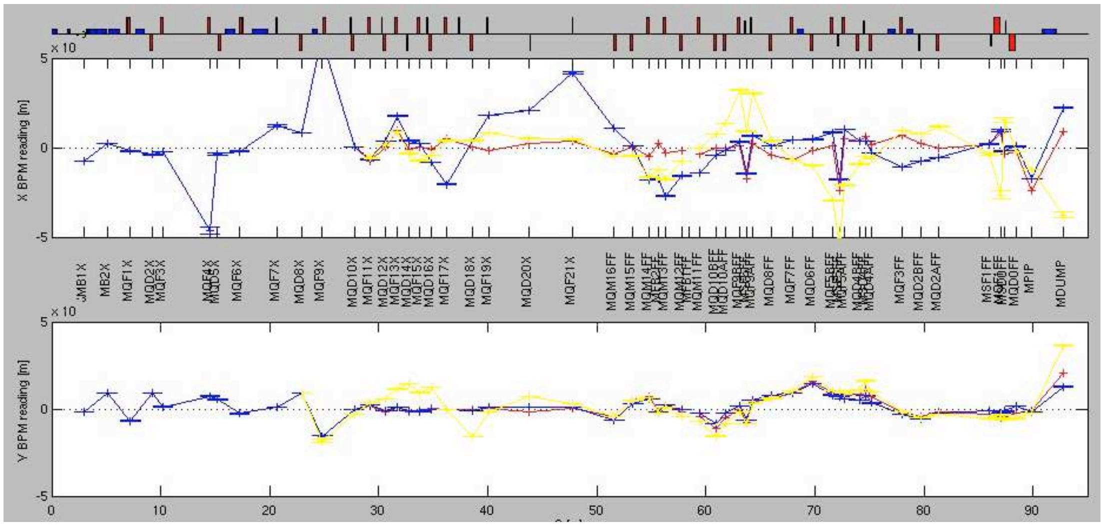

Figure 8.8: Result of the second experimental steering. Vertical correction is really nice, but a problem appeared in the horizontal plane. The correction was kept to test the ability to recover.

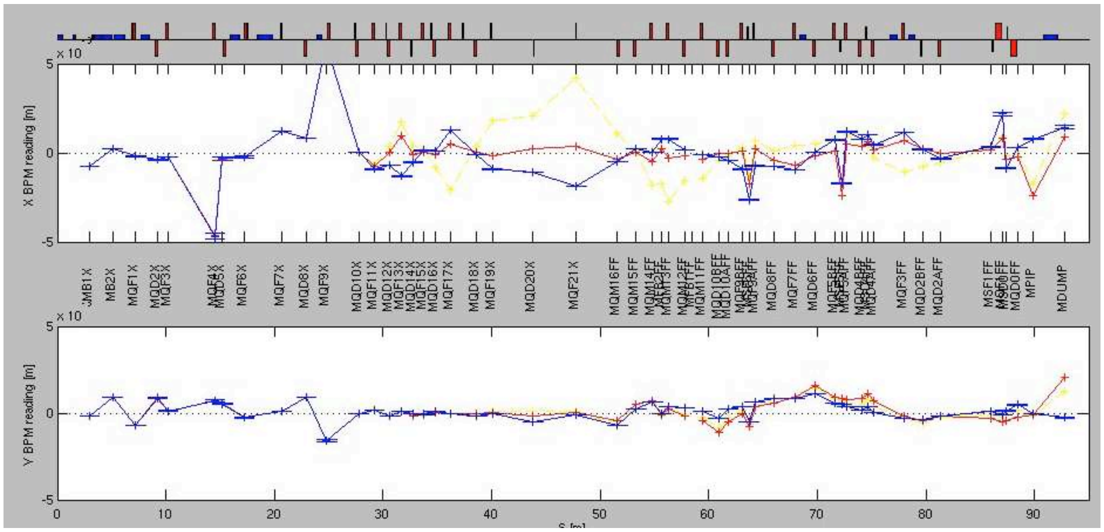

Figure 8.9: Results of the third experimental steering (horizontal). The result is very good in the final focus, the discrepancies in the extraction line are due to poorly known scale factors in non-mover cavity BPMs, which had not yet been properly calibrated.

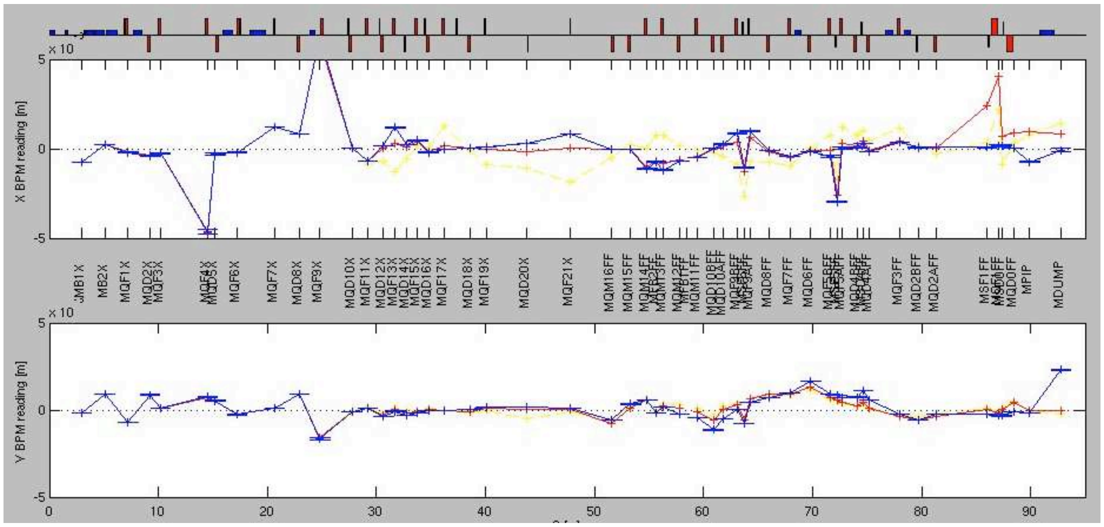

Figure 8.10: Result of the fourth experimental steering. There is still overcorrection in the extraction line, but it is converging.

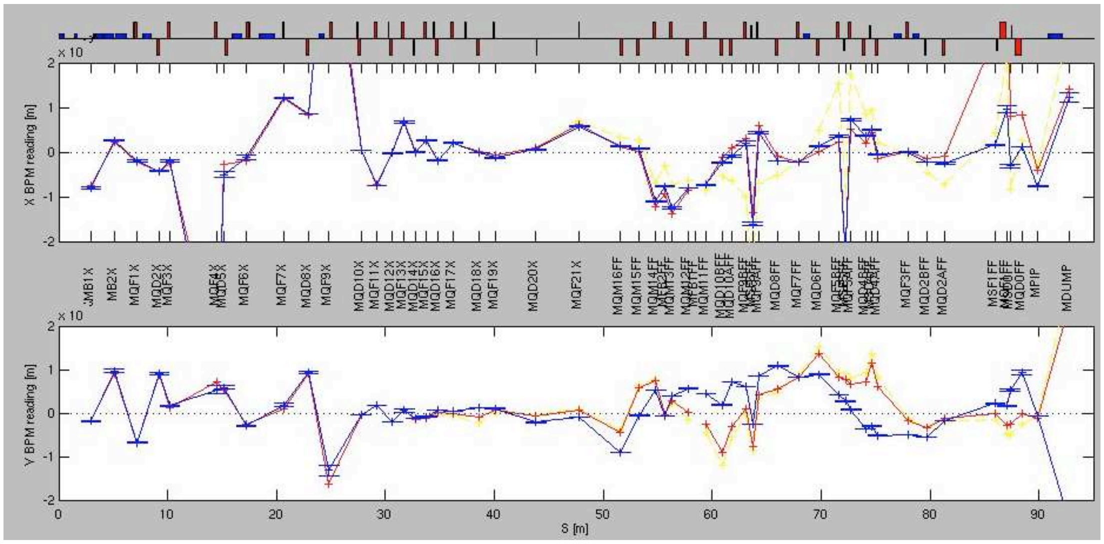

Figure 8.11: Result of the fifth experimental steering (scale changed). The horizontal plane is perfectly corrected but problems appeared in the vertical one, however without making the overall orbit worse.

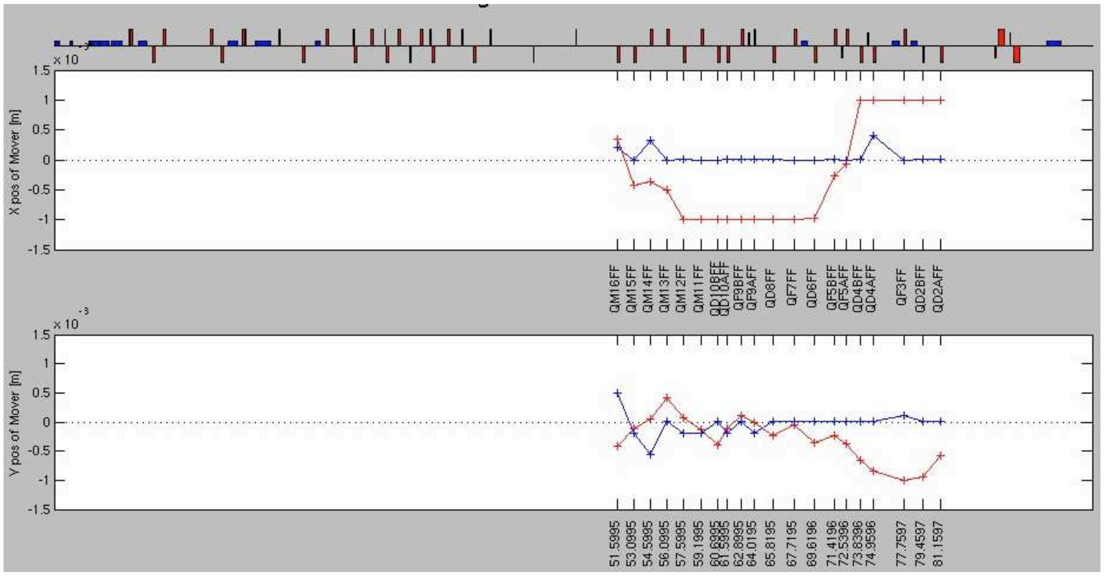

(a) mover displacements for final focus correction (blue=present status, red= after correction)

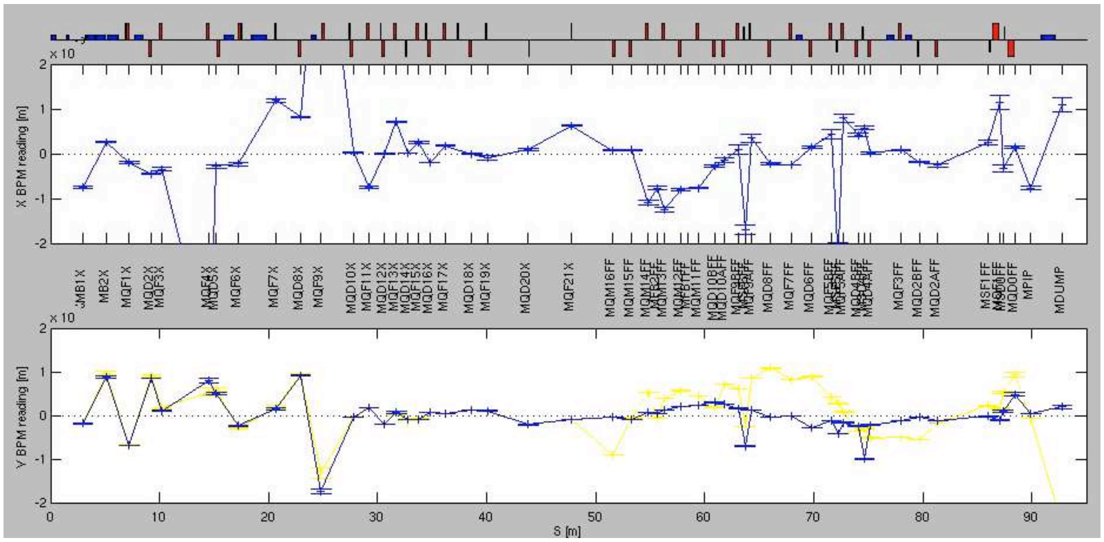

(b) orbit after final focus correction

Figure 8.12: Result of the final focus steering. The horizontal correction was saturating, it was not applied, but the vertical correction was efficient and corresponded to the expected one.

8.3.1 Principle of Pulse to Pulse Trajectory Fluctuation Reconstruction

When magnet settings are not changed, the transfer matrices are constant and the observed beam jitter is only due to the injection jitter, which can be described by the five parameters Δx, Δxp, Δy, Δyp and $\frac{\Delta E}{E}$ at a reference position. Presently, we can only measure Δx and Δy at each BPM.

From equation A.3 we have:

$$\begin{pmatrix} \Delta x(BPM) \\ \Delta y(BPM) \end{pmatrix} = \begin{pmatrix} R_{11} & R_{12} & R_{13} & R_{14} & R_{16} \\ R_{31} & R_{32} & R_{33} & R_{34} & R_{36} \end{pmatrix} \times \begin{pmatrix} \Delta x(\mathbf{ref}) \\ \Delta xp(\mathbf{ref}) \\ \Delta y(\mathbf{ref}) \\ \Delta yp(\mathbf{ref}) \\ \frac{\Delta E}{E}(\mathbf{ref}) \end{pmatrix} \tag{8.6}$$

If all the BPMs are not at the same phase, the M matrix which gives all the displacements in the BPMs function of the parameters at the reference point is not degenerate and can be written:

$$\begin{pmatrix} \Delta x(\mathbf{BPM}_1) \\ \vdots \\ \Delta x(\mathbf{BPM}_n) \\ \Delta y(\mathbf{BPM}_1) \\ \vdots \\ \Delta y(\mathbf{BPM}_n) \end{pmatrix} = \begin{pmatrix} R_{11}(\mathbf{ref} \to \mathbf{BPM}_1) & \cdots & R_{16}(\mathbf{ref} \to \mathbf{BPM}_1) \\ \vdots & & \vdots \\ R_{11}(\mathbf{ref} \to \mathbf{BPM}_n) & \cdots & R_{16}(\mathbf{ref} \to \mathbf{BPM}_n) \\ R_{31}(\mathbf{ref} \to \mathbf{BPM}_1) & \cdots & R_{36}(\mathbf{ref} \to \mathbf{BPM}_1) \\ \vdots & & \vdots \\ R_{31}(\mathbf{ref} \to \mathbf{BPM}_n) & \cdots & R_{36}(\mathbf{ref} \to \mathbf{BPM}_n) \end{pmatrix} \times \begin{pmatrix} \Delta x \\ \Delta xp \\ \Delta y \\ \Delta yp \\ \frac{\Delta E}{E} \end{pmatrix}_{\mathrm{ref}} \tag{8.7}$$

Reconstructing the trajectory fluctuations is equivalent to determining the parameters at the reference point, inverting equation 8.7, and propagating these parameters along all the beam line.

To make this reconstruction as precise as possible, the resolution of each BPM must be taken into account in the least square minimization, because there is no statistics when doing pulse by pulse measurements.

8.3.2 BPMs Noise Level Measurements

Each BPM measurement is affected by noise, mainly from the electronics. To measure BPM resolutions, a large set of measured trajectories can be used, looking for correlations between the different BPMs [39]. The noise at one BPM is by definition uncorrelated with that of other BPMs, unlike the beam positions, which are usually correlated because they are related by the transfer matrices. Hence, one can write:

$$X_{\mathrm{BPM\,1}}(\mathrm{pulse}_i) = \sum_{j=2}^{m} (\delta_j \cdot X_{\mathrm{BPM\,j}}(\mathrm{pulse}_i) + \alpha_j) + N_i \tag{8.8}$$

where $X_{\mathrm{BPM\,j}}(\mathrm{pulse}_i)$ corresponds to the horizontal measurement at the j^{th} BPM for the i^{th} pulse; δ_j and α_j are the linear relation coefficients between the measurement of the first and the j^{th} BPM; N_i is the noise value of the first BPM for the i^{th} pulse.

Equation 8.8 is equivalent, in matrix notation, to:

$$\begin{pmatrix} X_{\mathrm{BPM}\ 1}(\mathrm{pulse}_1) \\ \vdots \\ X_{\mathrm{BPM}\ 1}(\mathrm{pulse}_n) \end{pmatrix} = \begin{pmatrix} X_{\mathrm{BPM}\ 2}(\mathrm{pulse}_1) & \cdots & X_{\mathrm{BPM}\ m}(\mathrm{pulse}_1) & 1 \\ & \vdots & & \\ X_{\mathrm{BPM}\ 2}(\mathrm{pulse}_n) & \cdots & X_{\mathrm{BPM}\ m}(\mathrm{pulse}_n) & 1 \end{pmatrix} \times \begin{pmatrix} \delta_2 \\ \vdots \\ \delta_m \\ \alpha \end{pmatrix} + \begin{pmatrix} N_1 \\ \vdots \\ N_n \end{pmatrix} \tag{8.9}$$

Where: $\alpha = \sum_{j=2}^{m} \alpha_j$.

Let's call B_1 the vector of the first BPM readings and B_{all} this big matrix of all BPM readings except the first. Since the noise is random, we can have an estimation of the vector Δ containing the $m-1$ δ and the α coefficients writing:

$$\Delta = B_{all}^{-1} \cdot B_1 \tag{8.10}$$

The vector $N(BPM_1)$ containing the noise amplitude at each pulse for the first BPM can be obtained by this relation:

$$N(BPM_1) = B_1 - B_{all} \cdot (B_{all}^{-1} \cdot B_1) \tag{8.11}$$

The norm of the $N(BPM_1)$ vector, equal to the RMS of the noise amplitudes, will give the resolution of the first BPM. The same method is then applied for each BPM. However, the noise must be of the same order of magnitude for all the BPMs, or we get trouble when inverting the matrix. That's why the resolution measurement has been divided into two parts, one for the stripline and button BPMs and one for C-Band and S-Band cavity BPMs. The results are presented in figure 8.13. 300 pulses without any lattice change were used for this analysis.

The measured resolution of the buttons and striplines is $10 - 20\mu m$ and the resolution of the cavity BPMs is between $500nm$ and $1\mu m$ in the horizontal plane and $400nm$ in the vertical one. The large resolution of MQF4X was later found to be due to a bad contact at one electrode, but the reason is not clear why MQF9X also has large values.

MQF14FF was a test cavity where the $20dB$ attenuation was removed. It appears that the signal was saturating in the vertical plane for this BPM.

8.3.3 Experimental Fluctuation Determination

Once we knew the resolutions of the BPMs, we could optimize the reconstruction of the incoming parameters. To test this reconstruction, trajectory

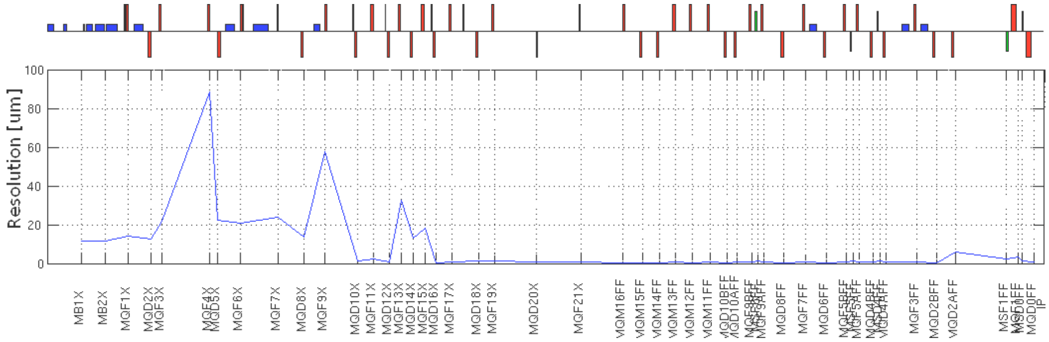

(a) Horizontal stripline and button BPMs

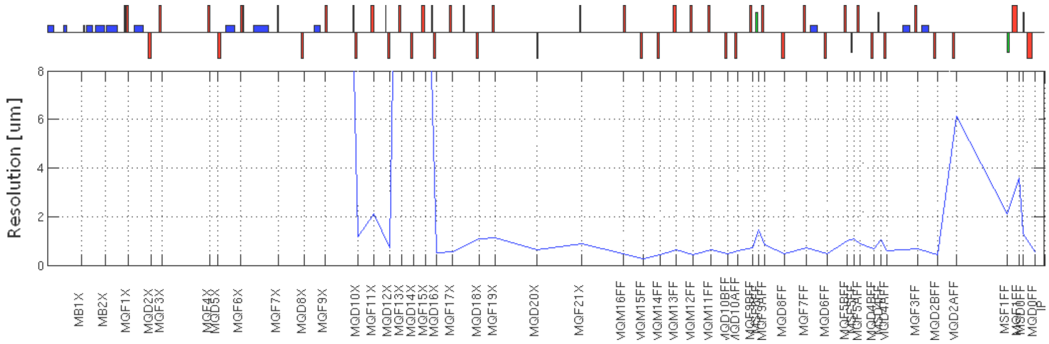

(b) Horizontal C-band cavity BPM resolutions

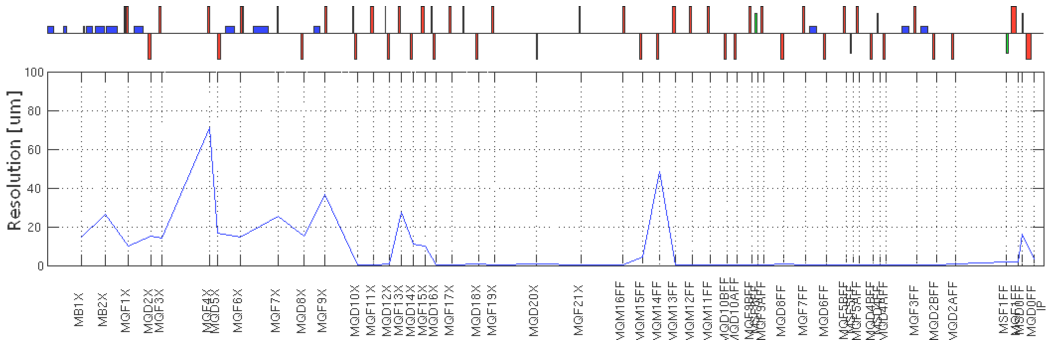

(c) Vertical stripline and button BPMs

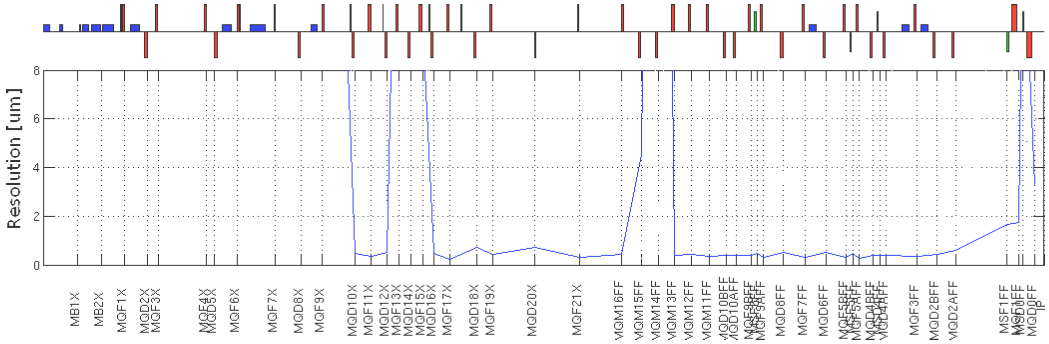

(d) Vertical C-band cavity BPM resolutions

Figure 8.13: Determination of horizontal and vertical BPM resolutions using correlation analysis.

data were taken during a dispersion measurement changing the ring cavity frequency to vary the beam energy. The sequence of the measurement was: ring cavity frequency change off, on ($0kHz$), $-3kHz$, $-2kHz$, $-1kHz$, $0kHz$, $1kHz$, $2kHz$, $3kHz$, $2kHz$, $1kHz$, $0kHz$, $-1kHz$, $-2kHz$, $-3kHz$, off. In this mode of operation, the absolute cavity ring frequency is not known precisely which means that running with the frequency change on with $0kHz$ introduces an unknown frequency change.

The parameters were reconstructed as described in section 8.3.1, using the injection point as reference. The time evolution of these reconstructed parameters is shown in figure 8.14. The fit was done using only the cavity BPMs with the resolutions determined as described in the previous section. The trajectory, deduced from the fitted parameters, was then propagated to all BPMs.

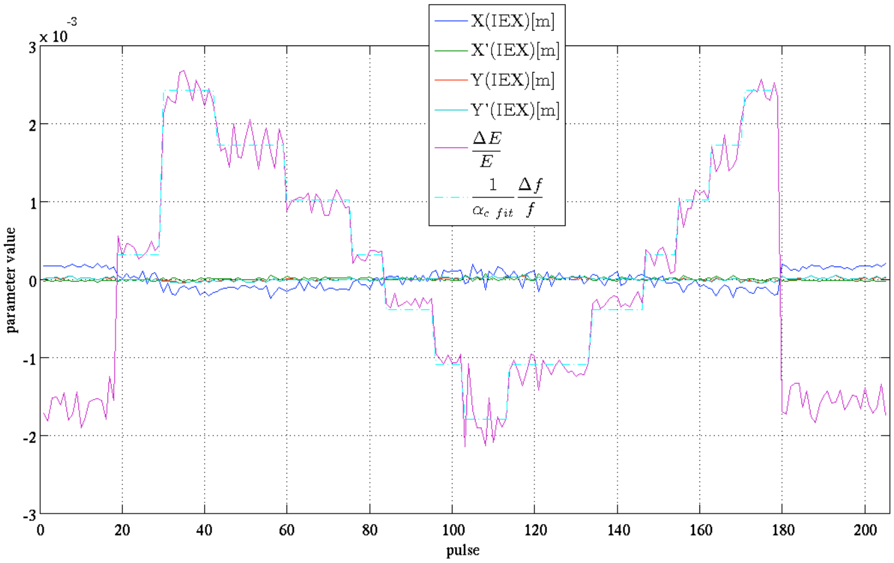

Figure 8.14: Reconstruction of the parameters at the injection point during a dispersion measurement.

The different ring cavity frequency steps applied during the dispersion measurement are clearly visible on the energy curve, as well as a correlation with

X, which indicates that some incoming dispersion was present. As the nominal dispersion is zero at that point, this dispersion was due to a mismatch in the ATF ring. It can be corrected in the extraction line.

This reconstruction also allows to estimate the absolute value of the frequency change. The $0kHz$ setting corresponds in fact to a $2.7 \pm 0.2kHz$ frequency change as one can see in the first two steps corresponding to the "ring cavity frequency change off" and "ring cavity frequency change on at $0kHz$" settings.

We can see in the figure 8.14, the pulse to pulse fluctuations of the reconstructed $\frac{\Delta E}{E}$ were about 5×10^{-4} . If we look at the histogram with the errors on that energy reconstruction (figure 8.15), we note its range is between 0 and 2×10^{-4}, which means that these reconstructed fluctuations were statistically meaningful.

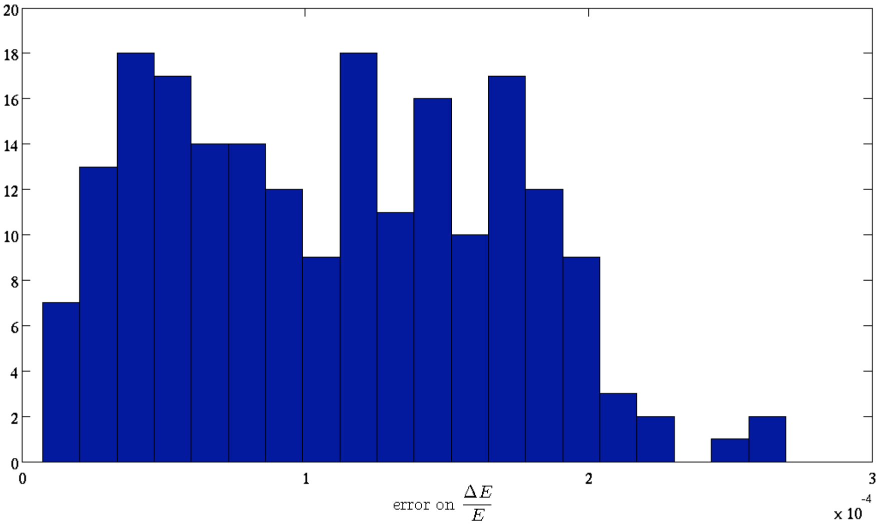

Figure 8.15: Histogram of the errors on the reconstruction of the energy in figure 8.14.

The formula 8.12 gives the relation between the frequency change and the momentum of the beam.

$$\frac{\Delta p}{p} = \frac{\gamma^2}{1 - \alpha_c \gamma^2} \frac{\Delta f_{ring}}{f_{ring}} \simeq -\frac{1}{\alpha_c} \frac{\Delta f_{ring}}{f_{ring}} \tag{8.12}$$

α_c is the momentum compaction factor of the ATF ring. The value of this factor can be obtained using the model: $\alpha_{c\ model} = \oint_{ring} \frac{D(s)}{\rho} \mathrm{d}s = 2.173 \cdot 10^{-3}$ and, as we know the ring frequency $f_{ring} = 714MHz$, we can measure this factor by fitting:

$$\alpha_{c\ fit} = -\frac{(\frac{\Delta f_{ring}}{f_{ring}})_{meas}}{(\frac{\Delta p}{p})_{meas}} \tag{8.13}$$

The fit result is presented in figure 8.16 and the energy variation, according to equation 8.12 using that fitted momentum compaction factor $\alpha_{c\ fit} = (1.99 \pm 0.02) \times 10^{-3}$, is superposed on the energy reconstructed fluctuation (figure 8.14).

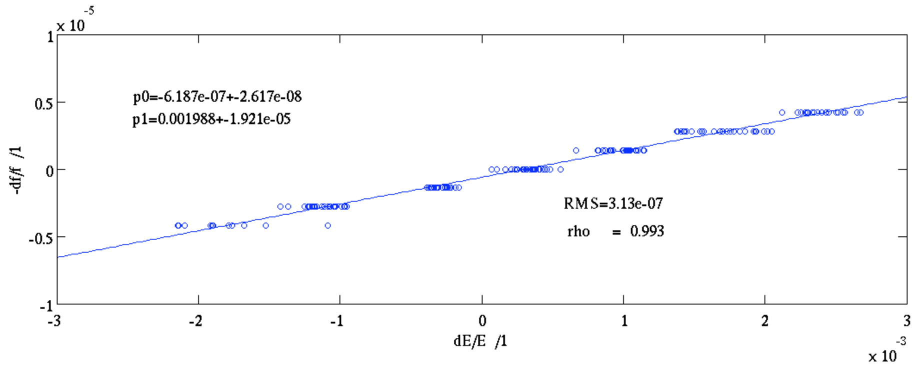

Figure 8.16: Fit of the momentum compaction factor.

We then tried to reconstruct the fluctuations of the orbit in periods when no change was applied. We made the parameter reconstruction using the same data as for the BPM resolution measurements presented in section 8.3.2.

We saw in section 8.3.2 that we can compute the BPM noise at each pulse N, if we subtract it from the BPM measurement ΔX_{read}, we get the real position

ΔX of the beam with respect to the electrical center of the BPM (or center of the magnet if BBA has been done previously): $\Delta X = \Delta X_{read} - N$.

To appreciate the precision achievable with this reconstruction, we compute for each BPM the quadratic sum of the beam position minus the reconstructed trajectory $\sqrt{\sum_{pulses}(\Delta X - \Delta X_{reco})^2}$ and plot it as the fit precision along with the resolution of the BPM for horizontal and vertical displacements (figure 8.17). The cavity BPMs on mover (except the sextupole ones) were used for this reconstruction.

We can see that the fit precision is a few microns in horizontal cavity BPMs and essentially below $1\mu m$ in the vertical plane. The statistical error can be estimated to be about the resolutions of the used BPMs divided by the square root of the number of BPMs used corresponding to $\simeq \frac{0.5}{20} \simeq 0.1\mu m$. As the statistical error is much below the fit precision, it means that the precision is limited by systematics such as errors on the transfer matrices, BPM scale factors or BPMs rotations. The fit resolution becomes bad for the MQF19X to MQF21X BPMs in the horizontal plane: as they are not on movers, their calibrations are more difficult, so scale errors are expected.

Also, comparing the fit precision with the spread of the raw measurement is indicative. If the trajectory fit is really incorrect, it will be uncorrelated to BPM measurements which are not used in the fit. So the fit quality will be close to the spread of the readings at these BPMs. However, we see the fit is good at the MQF13X, MQD14X and MQF15X stripline BPMs for example, giving us the assurance that the reconstruction is good even for beam fluctuations.

The characterization of this jitter at the injection has been done and the histogram of the energy jitter is presented in figure 8.18. The energy jitter was really low (2×10^{-5}). In the past, amplitudes of about 8×10^{-5} have been measured[40].

The amplitude of the position jitter should be below $\frac{1}{10}$ of the beam size. The

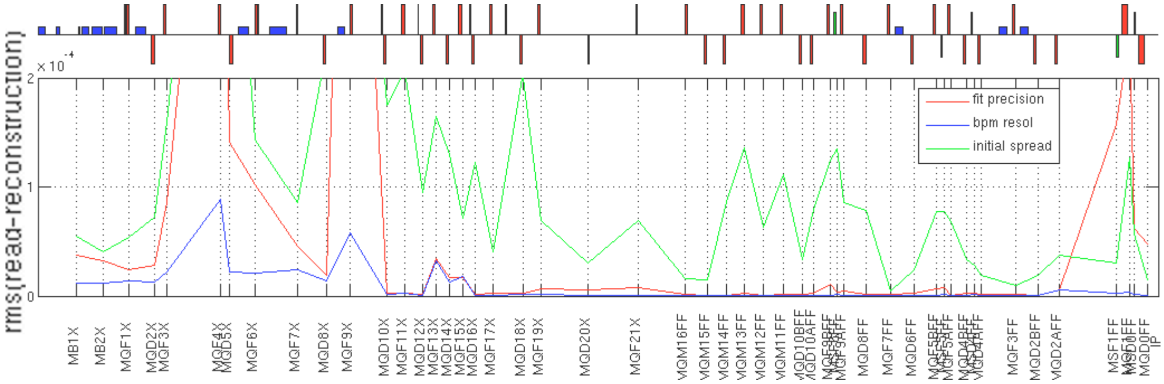

(a) Horizontal stripline and button BPMs

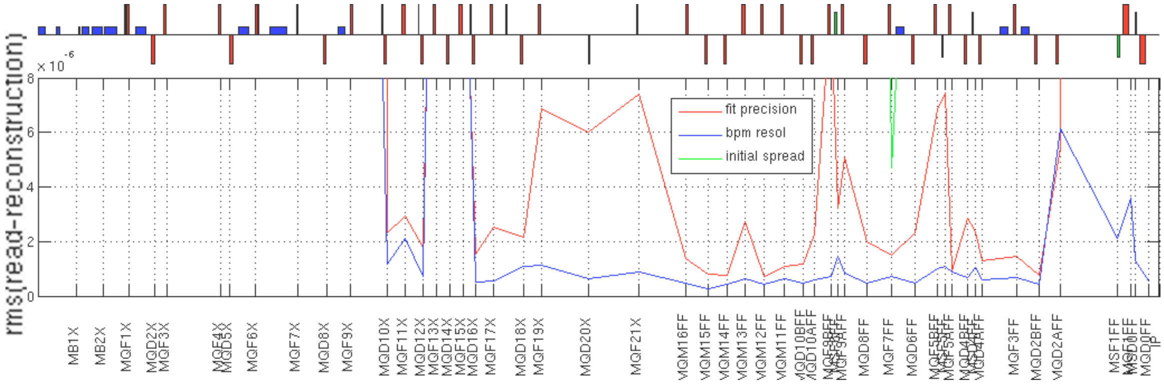

(b) Horizontal C-band cavity BPMs

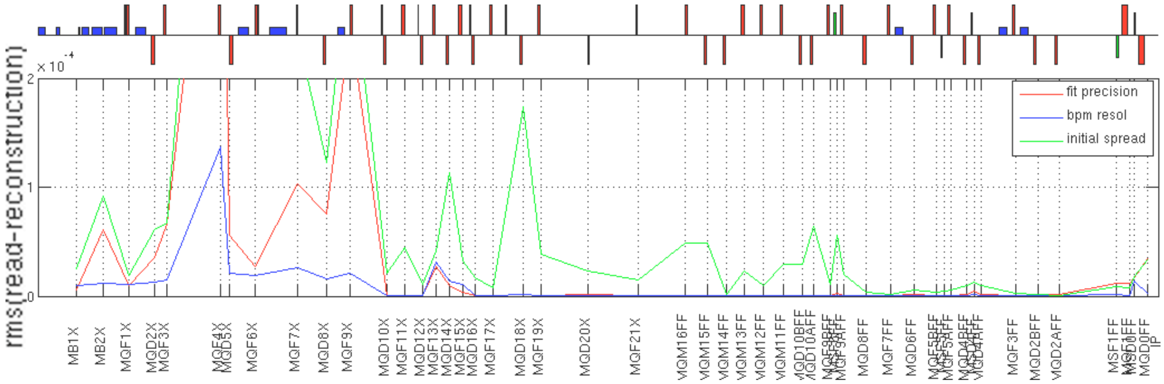

(c) Vertical stripline and button BPMs

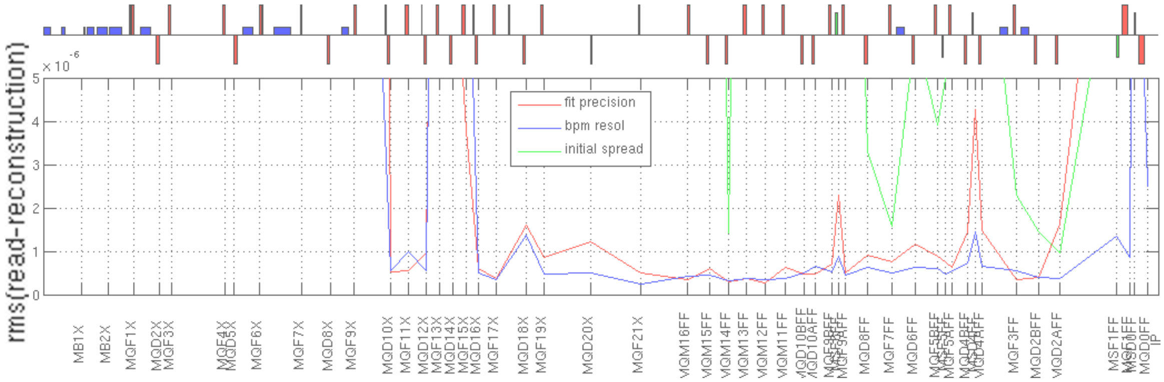

(d) Vertical C-band cavity BPMs

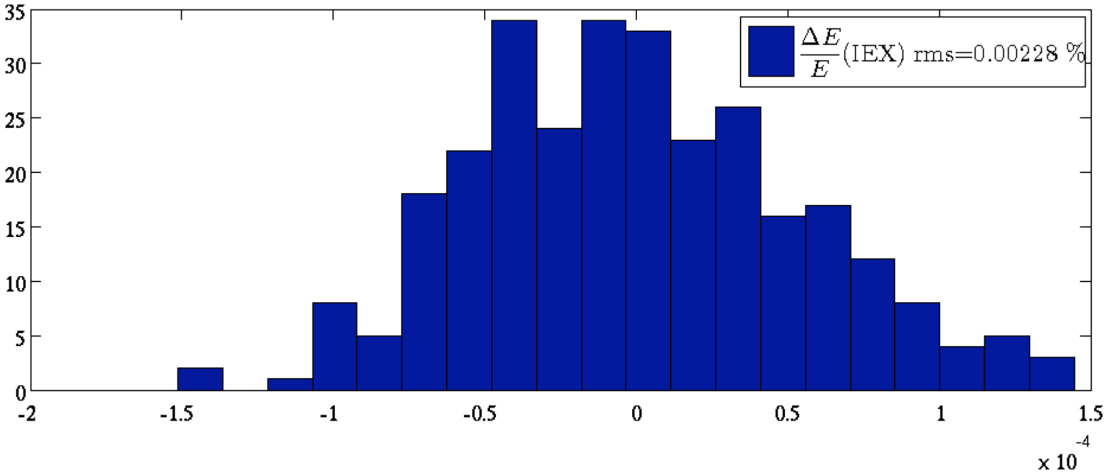

Figure 8.18: Energy jitter reconstructed.

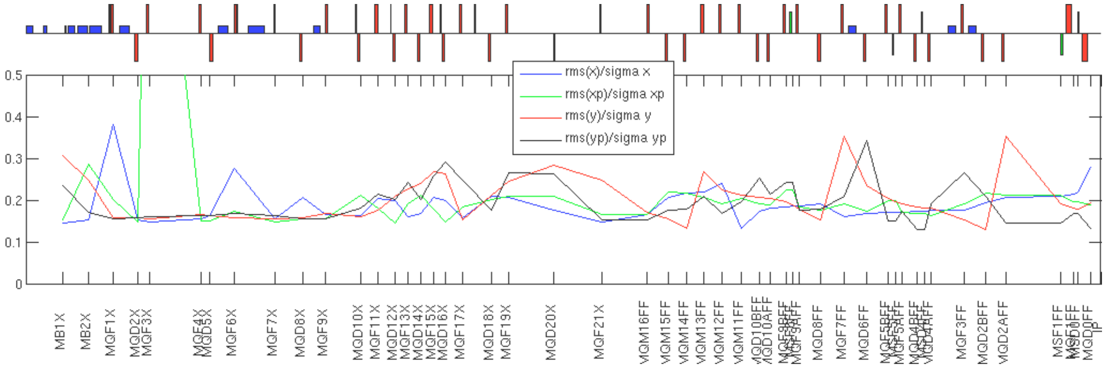

Figure 8.19: Amplitude of the jitter reconstructed normalized to the corresponding beam size.

figure 8.19 shows the factor of the RMS of the fluctuations for X, X', Y and Y' normalized by the corresponding beam size.

The beam jitter amplitude is almost $\frac{1}{5}$ of the beam size which is not so bad, but it needs to be corrected to fulfill the ATF2 goals. The variation of this ratio along the beam line indicates a mismatch between the model and the reality.

8.4 Dispersion Measurement

8.4.1 Principle of the Dispersion Measurement

The dispersion functions $D_x(s)$ and $D_y(s)$ describe the position displacement correlated to the energy whereas angular dispersion functions $D'_x(s)$ and $D'_y(s)$ describe the angular displacement correlated to the energy:

$$\begin{aligned}
\frac{\partial \Delta X(s)}{\partial \frac{\Delta E}{E}} &= D_x(s) \\
\frac{\partial \Delta Y(s)}{\partial \frac{\Delta E}{E}} &= D_y(s) \\
\frac{\partial \Delta X(s)'}{\partial \frac{\Delta E}{E}} &= D'_x(s) \\
\frac{\partial \Delta Y(s)'}{\partial \frac{\Delta E}{E}} &= D'_y(s)
\end{aligned}$$

We saw that we are able to reconstruct the pulse to pulse energy fluctuations. The correlation between the energy reconstruction and the BPM position measurements allows measuring the dispersion at each BPM. We have, with $R_{ij} = R_{ij}(ref \ \rightarrow \ BPM)$:

$$\Delta X(BPM) = R_{16} \times \frac{\Delta E}{E} + R_{11} \times X(ref) + \cdots + R_{14} \times Y'(ref) \tag{8.14}$$

The correlation between the position and the energy can be separated as:

$$\begin{array}{ccccccccc} \frac{\partial \Delta X(BPM)}{\partial \frac{\Delta E}{E}} & = & R_{16} & + & \frac{\partial X(ref)}{\partial \frac{\Delta E}{E}} \times R_{11} & + & \cdots & + & \frac{\partial Y'(ref)}{\partial \frac{\Delta E}{E}} \times R_{14} \\ D_x(BPM) & = & D_{x\ mod}(BPM) & + & D_x(ref) \times R_{11} & + & \cdots & + & D'_y(ref) \times R_{14} \end{array} \tag{8.15}$$

That means that the measured dispersion is a combination of the model dispersion and the propagation of the mismatched dispersion from injection.

To calculate the spatial and angular dispersion at a reference point $D(ref)$ from the difference ΔD between the measured spatial dispersion at each of the n BPM, D_x and D_y, and the modeled ones, $D_{x\ mod}$ and $D_{y\ mod}$, we must solve:

$$\Delta D = M \times D(ref) \tag{8.16}$$

With :

$$\Delta D = \begin{pmatrix} D_x(BPM_1) - D_{x\ mod}(BPM_1) \\ \vdots \\ D_x(BPM_n) - D_{x\ mod}(BPM_n) \\ D_y(BPM_1) - D_{y\ mod}(BPM_1) \\ \vdots \\ D_y(BPM_n) - D_{y\ mod}(BPM_n) \end{pmatrix}$$

$$M = \begin{pmatrix} R_{11}(ref \rightarrow BPM_1) & \cdots & R_{14}(ref \rightarrow BPM_1) \\ \vdots & & \vdots \\ R_{11}(ref \rightarrow BPM_n) & \cdots & R_{14}(ref \rightarrow BPM_n) \\ R_{31}(ref \rightarrow BPM_1) & \cdots & R_{34}(ref \rightarrow BPM_1) \\ \vdots & & \vdots \\ R_{31}(ref \rightarrow BPM_n) & \cdots & R_{34}(ref \rightarrow BPM_n) \end{pmatrix}$$

And

$$D(ref) = \begin{pmatrix} D_x(ref) \\ D'_x(ref) \\ D_y(ref) \\ D'_y(ref) \end{pmatrix}$$

To solve this equation, we use least square minimization. The horizontal and vertical dispersions are measured at each BPM through a linear fit of the beam positions function of the energy. The errors $D\ _{err}$ on the measured dispersion D obtained by these fits are used in the least square minimization: instead of finding $D(ref)$ minimizing $\chi^2 = \|(\Delta D - M \times D)^T \times (\Delta D - M \times D)\|$, we minimize $\chi^2 = \|(\Delta D - M \times D)^T \times W \times (\Delta D - M \times D)\|$. W is a diagonal matrix with elements $w_{ii} = \frac{1}{D_{err}(BPM_i)}$. The energy change can be determined by:

- Changing the ring frequency and using the compaction momentum factor (eq. 8.12).

- Using the energy jitter from the beam parameter reconstruction (see section 8.3.1) in a similar way to what has been done in SLC [41].

8.4.2 Dispersion Correction

Horizontal Dispersion correction

As shown chapter A.2, the dispersion is created by the dipoles magnets and we saw equation 8.15 that the dispersion is transported through the lattice like the position parameters. When dispersion correction is needed, as we cannot change the dipole strengths because that would change the geometry of the accelerator, we use the quadrupoles magnets. However, changing the quadrupole strengths has also effects on the monochromatic beam size, which must later be corrected by β matching.

Using equation 8.15 with a quadrupole as reference point, we have, with $R_{ij} = R_{ij}(quad \rightarrow BPM)$:

$$D_x(BPM) = R_{16} + D_x(quad) \times R_{11} + \cdots + D'_y(quad) \times R_{14} \tag{8.17}$$

From the equation above, it can be noted that the dispersion at a quadrupole is multiplied by the transfer matrix elements. To change the dispersion without affecting too much the other parameters of the line, the strength of a quadrupole where the dispersion is large will be changed by a small amount. Looking at the transfer matrix of a quadrupole of strength k and length l, in the thin lens approximation, the spatial dispersion does not change and the angular dispersions becomes:

$$\begin{array}{rclcl} D'_x(after) & = & klD_x(before) & + & D'_x(before) \\ D'_y(after) & = & -klD_y(before) & + & D'_y(before) \end{array} \tag{8.18}$$

When a change in quadrupole strength Δk is introduced, the changes in angular dispersions are:

$$\begin{array}{rcl} \frac{\Delta D'_x(after)}{\Delta k} & = & lD_x(before) \\ \frac{\Delta D'_y(after)}{\Delta k} & = & -lD_y(before) \end{array} \tag{8.19}$$

Using the notation $R_{ij}(k \rightarrow l) = R_{ij}(quad_k \rightarrow BPMl)$, the change in the angular dispersions at the m quadrupoles $\Delta D'_x(k)$ with $k = 1 \ldots m$ introduces a variation of the spatial dispersions measured in the n BPMs, $\Delta D_x(l)$ with $l = 1 \ldots n$ as shown in equation 8.21.

Finding the correction means finding the solution of equation 8.21. Once the desired variations in angular dispersions are calculated, the corresponding change in quadrupole strengths is obtained from equation 8.19. The expected change in dispersion at the BPMs can then be obtained applying the equation 8.21.

The horizontal dispersion in ATF2 is corrected using QF1X and QF6X where the spatial dispersion is nominally maximum $D_x(QF1X) = 0.5m$ and $D_x(QF6X) = -0.5m$. The usual changes in strengths are below $\frac{\Delta k}{k} < 10\%$. For the correction, two quadrupoles at different phases are enough because there are only two independent parameters, $D_x(incoming)$ and $D'_x(incoming)$, to be corrected.

Vertical Dispersion correction

As the nominal vertical dispersion in ATF2 is zero all accelerator long, the correction scheme used for the horizontal dispersion cannot be applied, instead a pair of skew quadrupoles (QK1X and QK2X) is used. They are placed close to QF1X and QF6X to be in region of high horizontal dispersion. The principle is to use the same strengths for both skew quadrupoles. The vertical dispersion is generated by coupling from the horizontal dispersion. The XY coupling introduced by the first skew quad is canceled by the second thanks to an ad hoc transfer matrix relation.

When a change in skew quadrupole strength Δk is introduced, the variations in angular dispersion and angles are:

$$\begin{aligned}
\frac{\Delta D'_x(after)}{\Delta k} &= -lD_y(before) \\
\frac{\Delta D'_y(after)}{\Delta k} &= -lD_x(before) \\
\frac{\Delta X'(after)}{\Delta k} &= -lY(before) \\
\frac{\Delta Y'(after)}{\Delta k} &= -lX(before)
\end{aligned} \tag{8.20}$$

$$\begin{pmatrix} \Delta D_x(1) \\ \vdots \\ \Delta D_x(n) \\ \Delta D_y(1) \\ \vdots \\ \Delta D_y(n) \end{pmatrix} = \begin{pmatrix} R_{12}(1 \to 1) & \cdots & R_{12}(m \to 1) & R_{14}(1 \to 1) & \cdots & R_{14}(m \to 1) \\ \vdots & & \vdots & \vdots & & \vdots \\ R_{12}(1 \to n) & \cdots & R_{12}(m \to n) & R_{14}(1 \to n) & \cdots & R_{14}(m \to n) \\ R_{14}(1 \to 1) & \cdots & R_{14}(m \to 1) & R_{34}(1 \to 1) & \cdots & R_{34}(m \to 1) \\ \vdots & & \vdots & \vdots & & \vdots \\ R_{14}(1 \to n) & \cdots & R_{14}(m \to n) & R_{34}(1 \to n) & \cdots & R_{34}(m \to n) \end{pmatrix} \times \begin{pmatrix} \Delta D'_x(1) \\ \vdots \\ \Delta D'_x(m) \\ \Delta D'_y(1) \\ \vdots \\ \Delta D'_y(m) \end{pmatrix} \qquad (8.21)$$

As the design vertical dispersion is zero, its effect on the horizontal can be neglected and we obtain, with $\Delta k = \Delta k(QS1X) = \Delta k(QS2X)$ and the notations $\Delta D'_y(a1) = \Delta D_y x'(after\ QS1X)$ and $D_x(b2) = D_x(before\ QS2X)$:

$$\begin{array}{rcrcc}
\Delta D'_y(a1) & = & -\Delta kl\ D_x(b1) & & \\
\Delta D'_y(a2) & = & -\Delta kl\ D_x(b2) & + & \Delta D'_y(b2) \\
 & = & -\Delta kl\ D_x(b2) & + & R_{44}(1 \to 2)\ \Delta D'_y(a1) \\
 & = & -\Delta kl\ D_x(b2) & - & \Delta kl\ R_{44}(1 \to 2)\ D_x(b1)
\end{array} \tag{8.22}$$

The transfer matrix between QK1X and QK2X is by design:

$$R(1 \to 2) = \begin{pmatrix} 1 & 0 & 0 & 0 \\ 0 & 1 & 0 & 0 \\ 0 & 0 & -1 & 0 \\ 0 & 0 & 0 & -1 \end{pmatrix}$$

and the horizontal dispersion is opposite at these two points ($D = D_x(b1) = -D_x(b2)$), so we have $\Delta D'_y(a2) = 2\Delta klD$ whereas the angles introduced cancel each other:

$$\begin{array}{rcrcc}
\Delta Y'(a1) & = & -\Delta kl\ X(b1) & & \\
\Delta Y'(a2) & = & -\Delta kl\ X(b2) & + & \Delta Y'(b2) \\
 & = & -R_{11}(2 \to 1)\Delta kl\ X(b1) & + & R_{44}(1 \to 2)\Delta Y'(a1) \\
 & = & -\Delta kl\ X(b1) & + & \Delta kl\ X(b1) \\
 & = & 0 & &
\end{array} \tag{8.23}$$

The correction is obtained for the horizontal plane finding the solution of equation 8.21 and the corresponding change in quadrupole strength is deduced from equation 8.20. The expected change in dispersion at the BPMs is obtained from equation 8.21.

As there are only two skew quadrupoles to correct dispersion and since they are at the same phases to avoid introducing XY coupling, only one phase of the vertical dispersion can be corrected.

Adding two other skew quadrupoles has been considered to give the possibility to correct the other phase, but an efficient solution was not found. The solution retained is to create a local dispersive bump using steering correctors.

Considering n correctors, a vertical dispersive bump is defined as a trajectory variation creating only spatial ($D_y(end)$) or angular ($D'_y(end)$) dispersion (eq. 8.24), but no displacement ($Y(end)$) and no angle ($Y'(end)$) at the end of the last corrector used (eq. 8.25).

Solving this system allows to find the corrector angle knob creating a dispersive bump. With the ratio of $D_y(end)$ and $D'_y(end)$, it is even possible to choose the phase of the dispersion corrected. The opposite phase of the skew quad correction is chosen for complementarity with that correction.

The vertical dispersion correction remains a challenge in ATF2 because the transfer matrix between the two skew quadrupoles is not exactly the design one, resulting in some coupling leakage after the second skew quadrupole. Also the dispersion bump induces an offset in the second kicker where a sextupole field has been found, creating non linear effects and background.

8.4.3 Comparison of two Dispersion Reconstruction Methods

Using the data displayed figure 8.14, where the energy had been changed using the ring cavity frequency, we fit the dispersion at all BPMs. As shown figure 8.20, it is more precise to use the energy value from the reconstruction than the one obtained using the momentum compaction factor, so that will always be the case from now.

$$\begin{pmatrix} \Delta D_y(end) \\ \Delta D'_y(end) \end{pmatrix} = \begin{pmatrix} R_{33}(1 \to n) & \cdots & R_{33}(n \to n) & R_{34}(1 \to n) & \cdots & R_{34}(n \to n) \\ R_{43}(1 \to n) & \cdots & R_{43}(n \to n) & R_{44}(1 \to n) & \cdots & R_{44}(n \to n) \end{pmatrix} \times \begin{pmatrix} D_y(1) \\ \vdots \\ D_y(n) \\ D'_y(1) \\ \vdots \\ D'_y(n) \end{pmatrix} \tag{8.24}$$

$$\begin{pmatrix} \Delta Y(end) \\ \Delta Y'(end) \end{pmatrix} = \begin{pmatrix} 0 \\ 0 \end{pmatrix} = \begin{pmatrix} R_{34}(1 \to n) & \cdots & R_{34}(n \to n) \\ R_{44}(1 \to n) & \cdots & R_{44}(n \to n) \end{pmatrix} \times \begin{pmatrix} Y'(1) \\ \vdots \\ Y'(n) \end{pmatrix} \tag{8.25}$$

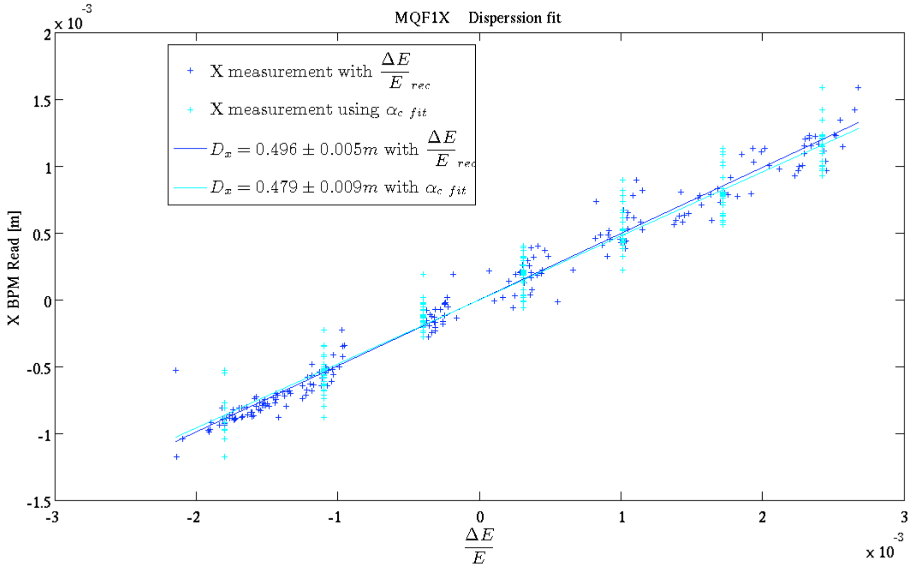

Figure 8.20: Two methods for horizontal dispersion fit at MQF1X.

From the measurements of the dispersions in the BPMs, the fit of the incoming spatial and angular dispersion at the injection point is deduced by least square minimization (equation 8.16). The incoming dispersion is then propagated along the beam line to be compared with the individual BPM measurements. The trajectory resulting from this propagation using the cavity BPMs is compared figure 8.21 with the individual BPM dispersion measurements.

One of the strengths of this method is reduced systematic errors compared with methods based on single positions measurement.

The same measurement has been used with beam jitter (without changing the ring cavity frequency). The results are shown in figure 8.22.

On this graph, the dispersion after the correction is also estimated. However, this correction has not been tested yet. We can see that the fit is consistent with most of the individual horizontal measurements and with most of the vertical cavity BPM measurements. The dispersion measurements are very close with the two methods (see table 8.3).

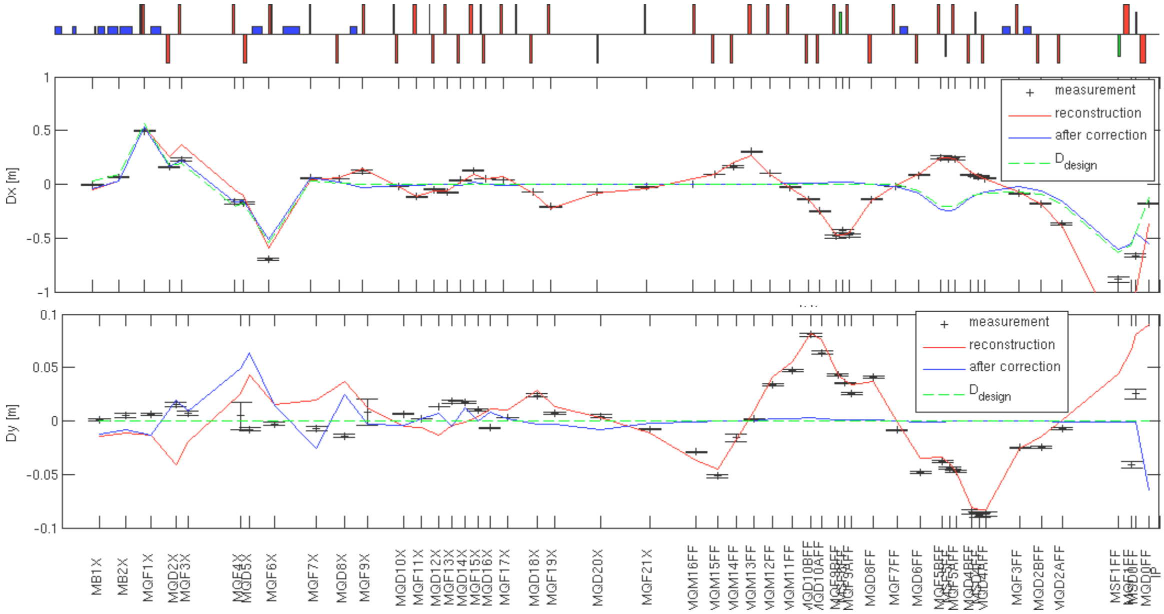

Figure 8.21: Reconstructed dispersion compared to individual BPM measurements based on changing the ring cavity frequency.

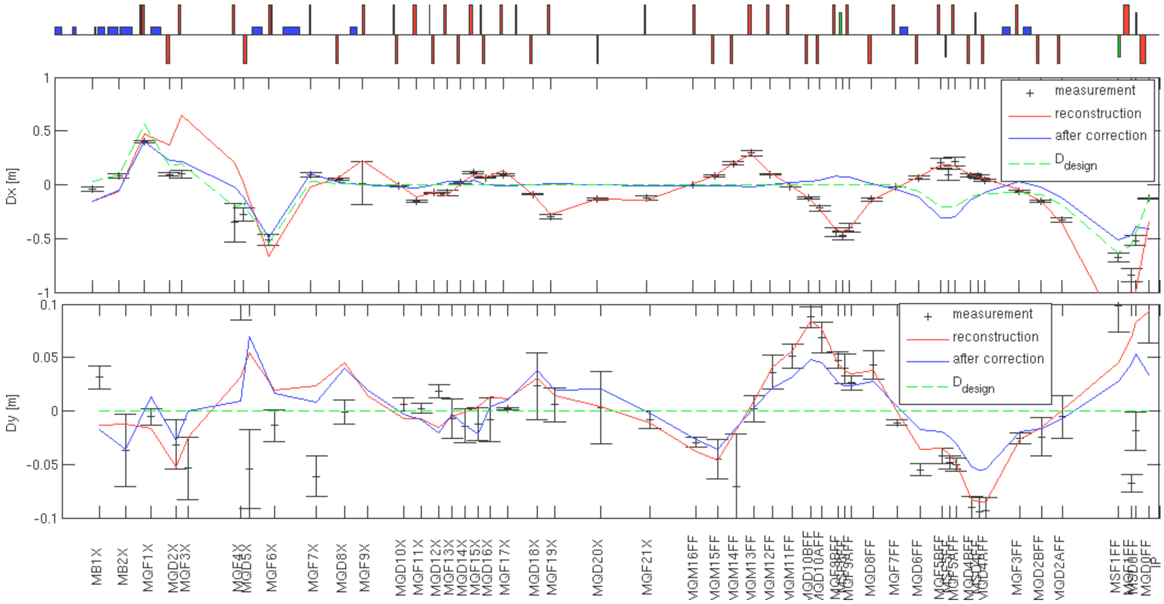

Figure 8.22: Reconstructed dispersion compared to individual BPM measurements based on using beam fluctuations.

	measurement changing ring cavity frequency	measurement from fluctuation
$D_x(MQD10X)[mm]$	-22 ± 2	-22 ± 1
$D'_x(MQD10X)[mrad]$	-73 ± 1	-79 ± 1
$D_y(MQD10X)[mm]$	-6 ± 3	-9 ± 2
$D'_y(MQD10X)[mrad]$	0 ± 4	6 ± 2
$D_x(IP)[mm]$	-127 ± 1	-131 ± 1
$D'_x(IP)[mrad]$	271 ± 1	278 ± 1
$D_y(IP)[mm]$	29 ± 3	24 ± 3
$D'_y(IP)[mrad]$	-67 ± 8	-58 ± 6

Table 8.3: Comparison of the two dispersion fit methods using MQD10X or IP as reference point.

One can see that the errors on the measurements do not depend on the choice of method. The reason for that is that the reconstructed dispersion at injection is dominated by the systematic errors (BPMs scales factors, transfer matrices estimation, etc.).

The criteria for a good dispersion correction can be deduced from the influence of the dispersion on the beam size (notation σ_{tot} for the beam size with the dispersion effect and σ_{mono} for the monochromatic beam size).

For example to calculate the dispersion D_{max} at IP which increases the beam size by $r = 10\%$ at IP, as we have:

$$\sigma_{tot} = \sqrt{\sigma_{mono}^2 + (D\frac{\Delta E}{E})^2}$$

we get:

$$r = \frac{\sigma_{tot}}{\sigma_{mono}} - 1 = \sqrt{1 + \left(\frac{D_{max}\frac{\Delta E}{E}}{\sigma_{mono}}\right)^2} - 1 \simeq \left(\frac{D_{max}\frac{\Delta E}{E}}{2\sigma_{mono}}\right)^2 \quad \text{if } D_{max}\frac{\Delta E}{E} \ll \sigma_{mono}$$

So,

$$D_{max} = 2\frac{\sqrt{r}\sigma_{mono}}{\frac{\Delta E}{E}} \tag{8.26}$$

From equation 8.26 we get, for $r = 10\%$ and nominal optics, that the dispersion must not exceed $D_{x\ max} = 10mm$ and $D_{y\ max} = 1mm$. As the measurements of the dispersion show a few mm precision (table 8.3), further improvements on the vertical measurement are needed at the IP.

Chapter 9

BEAM SIZE TUNING

Once the trajectory and the extraction line corrections detailed in chapter 6 are done, optical corrections in the final focus are made by moving sextupoles.

The more advanced techniques to achieve the $37nm$ vertical beam size are expected to take about a day [42] and some others up to a week [43] depending on the beam size goal. For the early commissioning stage, a simpler technique has been proposed based on pre-computed ratios of sextupole displacements acting orthogonally on the biggest correlations based on simulations.

Also, in the simulation, this technique has been tested without any previous tuning except trajectory correction, similar to what is sometimes done experimentally due to the busy ATF2 schedule. However, this study was stopped when the ATF2 commissioning started, to focus on the on-going experiments and to get the possibility to acquire data. This is why some aspects have not been studied.

9.1 Correction Moving Sextupoles

9.1.1 Effect of Sextupole Displacements

As described in section A.2.5, the field of a sextupole is:

$$\begin{aligned} B_x &= mxy \\ B_y &= m(x^2 - y^2) \end{aligned}$$

If we consider a horizontal displacement of δ_x, the field becomes:

$$\begin{aligned}
B_x(\delta_x) &= 2m(x-\delta_x)y \\
&= 2mxy - 2m\delta_x y \\
&= 2mxy + K_{\delta_x} y \text{ with } K_{\delta_x} = -2m\delta_x \\
B_y(\delta_x) &= m((x-\delta_x)^2 - y^2) \\
&= m(x^2-y^2) - 2m\delta_x x + m\delta_x^2 \\
&= m(x^2-y^2) + K_{\delta_x} x + D_{\delta_x} \text{ with } D_{\delta_x} = m\delta_x^2
\end{aligned} \tag{9.1}$$

That means a horizontal displacement of a sextupole induces a quadrupole field of strength K_{δ_x} and a horizontal dipole field of strength D_{δ_x}.
With a vertical displacement of δ_y of the sextupole, the field becomes:

$$\begin{aligned}
B_x(\delta_y) &= 2mx(y-\delta_y) \\
&= 2mxy - 2m\delta_y x \\
&= 2mxy + K_{\delta_y} x \text{ with} K_{\delta_y} = -2m\delta_y \\
B_y(\delta_y) &= m(x^2 - (y-\delta_y)^2) \\
&= m(x^2-y^2) - 2m\delta_y y + m\delta_y^2 \\
&= m(x^2-y^2) + K_{\delta_y} y + D_{\delta_y} \text{ with } D_{\delta_y} = m\delta_y^2
\end{aligned} \tag{9.2}$$

That means a vertical displacement of a sextupole induces a skew quadrupole field of strength K_{δ_y} and a vertical dipole field of strength D_{δ_y}.

The magnetic fields create correlations between the five dimensions of phase space (x, x', y, y' and E). As the electrons are relativistic, the force applied to them and the corresponding angle are (in thin lens approximation):

$$\begin{aligned} m_e x'' &= F_x &&= -ecB_y \\ m_e y'' &= F_y &&= ecB_x \\ x' &= \tfrac{ec}{m_e} B_y L \\ y' &= \tfrac{ec}{m_e} B_x L \end{aligned} \tag{9.3}$$

where L the magnetic length of the magnet.

As the magnetic fields depend on the transverse position in the magnet, the angle introduced by going through the magnets, will depend on the transverse position too. These angles are converted into position during the transfer along the beam line, creating correlations in the five dimensional phase space.

If we consider the matrix B_b containing the coordinates of each of the N electrons before the magnet, the matrix (C) of the introduced kicks and the matrix B_a after the magnet, we have:

$$\begin{aligned} B_b &= \begin{pmatrix} x(e_1^-) & x'(e_1^-) & y(e_1^-) & y'(e_1^-)\frac{dE}{E}(e_1^-) \\ & & \vdots & \\ x(e_N^-) & x'(e_N^-) & y(e_N^-) & y'(e_N^-)\frac{dE}{E}(e_N^-) \end{pmatrix} \\ C &= \begin{pmatrix} 0 & \frac{ec}{m_e}B_y(x_1,y_1)L & 0 & \frac{ec}{m_e}B_x(x_1,y_1)L & 0 \\ & & \vdots & & \\ 0 & \frac{ec}{m_e}B_y(x_N,y_N)L & 0 & \frac{ec}{m_e}B_x(x_N,y_N)L & 0 \end{pmatrix} \\ B_a &= C + B_b \end{aligned} \tag{9.4}$$

To investigate the influence at a downstream position, looking at the electron position matrix B_d, relating with the magnet output with the transfer matrix R, we obtain:

$$\begin{aligned} B_d &= B_a \times R \\ &= C \times R + B_b \times R \end{aligned} \tag{9.5}$$

The $R \times C$ term corresponds to the influence of the magnet on the beam positions. This term modifies the linear and higher order coefficients between the positions of the electrons.
We introduce the notations:

- The centered variable $\overline{x} = x - < x > = x - \frac{1}{N}\sum_{i=1}^{N} x_i$.
- The covariance $< \overline{x}\,\overline{y} > = \frac{1}{N}\sum_{i=1}^{N} \overline{x}_i \cdot \overline{y}_i$.

The A coefficient, between the x and y position, is computed from the covariance by:

$$A = \frac{< \overline{x}\,\overline{y} >}{< \overline{x}\,\overline{x} >} \tag{9.6}$$

The figure 9.1 shows the correlation introduced by a quadrupole field on a beam distribution.

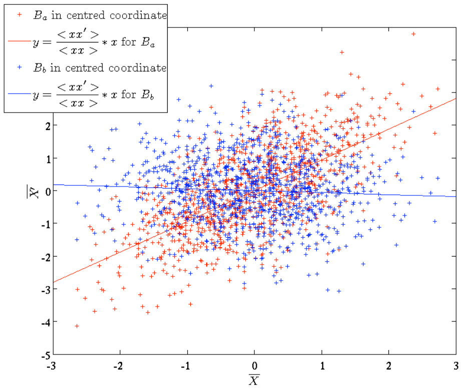

Figure 9.1: $\overline{X}$ and $\overline{X'}$ positions of the electrons with or without a quadrupole field.

The covariance matrix Σ, which gives the covariance between all the dimensions (for example the element $\sigma_{ij} = < z_i\, z_j >$), can be deduced from the electron position matrix:

$$\Sigma = B^T B \tag{9.7}$$

If we use the notation Σ_a and Σ_b to represent respectively the covariance matrix after a displaced sextupole and the covariance matrix before it, we get:

$$\begin{aligned} \Sigma_a &= B_a^T B_a \\ &= (B_b + C)^T (B_b + C) \\ &= B_b^T B_b + B_b^T C + C^T B_b + C^T C \end{aligned} \quad (9.8)$$

And

$$\begin{aligned} B_b^T B_b &= \Sigma_b \\ B_b^T C &= \frac{ec}{m_e} L \begin{pmatrix} 0 & < B_y\, x > & 0 & < B_x\, x > & 0 \\ 0 & < B_y\, x' > & 0 & < B_x\, x' > & 0 \\ & \vdots & \vdots & \vdots & \vdots \\ 0 & < B_y\, \frac{\Delta E}{E} > & 0 & < B_x\, \frac{\Delta E}{E} > & 0 \end{pmatrix} \end{aligned} \quad (9.9)$$

$$C^T B_b = \frac{ec}{m_e} L \begin{pmatrix} 0 & \cdots & 0 \\ < B_y\, x > & \cdots & < B_y\, \frac{\Delta E}{E} > \\ 0 & \cdots & 0 \\ < B_x\, x > & \cdots & < B_x\, \frac{\Delta E}{E} > \\ 0 & \cdots & 0 \end{pmatrix} \quad (9.10)$$

$$C^T C = (\frac{ec}{m_e} L)^2 \begin{pmatrix} 0 & & \cdots & & 0 \\ 0 & < B_y\, B_y > & 0 & < B_y\, B_x > & 0 \\ 0 & & \cdots & & 0 \\ 0 & < B_x\, B_y > & 0 & < B_x\, B_x > & 0 \\ 0 & & \cdots & & 0 \end{pmatrix} \quad (9.11)$$

We obtain that the beam covariance matrix after the sextupole (Σ_a) is the combination of the one before the sextupole (Σ_b) and an effect matrix ($\Sigma_{effect} = B_b^T C + C^T B_b + C^T C$). The expression of Σ_{effect} is given equation 9.12 with $a = \frac{ec}{m_e} L$.

$$\Sigma_{effect} =$$

$$\begin{pmatrix} 0 & a < B_y\ x > & 0 & a < B_x\ x > & 0 \\ a < B_y\ x > & 2a < B_y\ x' > + a^2 < B_y\ B_y > & a < B_y\ y > & 2a < B_x\ x' > + a < B_y\ y' > + a^2 < B_y\ B_x > & < B_y\ \frac{\Delta E}{E} > \\ 0 & q < B_y\ y > & 0 & q < B_x\ y > & 0 \\ a < B_x\ x > & a < B_y\ y' > + a < B_x\ x' > + a^2 < B_x\ B_y > & a < B_x\ y > & 2a < B_x\ y' > + a^2 < B_x\ B_x > & < B_x\ \frac{\Delta E}{E} > \\ 0 & < B_y\ \frac{\Delta E}{E} > & 0 & < B_x\ \frac{\Delta E}{E} > & 0 \end{pmatrix} \tag{9.12}$$

$$\begin{aligned} \Sigma_{effect}(quad) &= \begin{pmatrix} 0 & aK < x^2 > & 0 & 0 & 0 \\ aK < x^2 > & a^2K^2 < x^2 > & 0 & 0 & KD_x < {\frac{\Delta E}{E}}^2 > \\ 0 & 0 & 0 & aK < y^2 > & 0 \\ 0 & 0 & aK < y^2 > & a^2K^2 < y^2 > & KD_y < {\frac{\Delta E}{E}}^2 > \\ 0 & KD_x < {\frac{\Delta E}{E}}^2 > & 0 & KD_y < {\frac{\Delta E}{E}}^2 > & 0 \end{pmatrix} \\ \Sigma_{effect}(skew) &= \begin{pmatrix} 0 & 0 & 0 & aK < x^2 > & 0 \\ 0 & a^2K^2 < y^2 > & aK < y^2 > & 0 & KD_y < {\frac{\Delta E}{E}}^2 > \\ 0 & aK < y^2 > & 0 & 0 & 0 \\ aK < x^2 > & 0 & 0 & a^2K^2 < x^2 > & KD_x < {\frac{\Delta E}{E}}^2 > \\ 0 & KD_y < {\frac{\Delta E}{E}}^2 > & 0 & KD_x < {\frac{\Delta E}{E}}^2 > & 0 \end{pmatrix} \end{aligned} \tag{9.13}$$

That general form of the covariance matrix of the effect due to the introduction of a field, can be applied for the quadrupole and the skew quadrupole case ($\Sigma_{effect}(quad)$ and $\Sigma_{effect}(skew)$), using K as their strengths and D_x and D_y as the dispersion at that point. Result is shown equation 9.13.

That approximation of the Σ_{effect} matrix derives form the fact the beam is large in the sextupole (see figure 9.2) so we can neglect the $< x\ x' > < y\ y' >$ and beam coupling variance compared to $< x^2 >$ and $< y^2 >$.

A quadrupole field introduces $< x\ x' >$ and $< y\ y' >$ covariance proportional respectively to the square of the horizontal beam size at the sextupole position $< x^2 >$ and to the square of the vertical beam size $< y^2 >$. A skew quadrupole field introduces $< x\ y' >$, $< x'\ y >$ covariance proportional respectively to the square of the horizontal and of the vertical beam size.

These covariances can be tracked to a downstream point, where they are described by the Σ_d matrix, thanks to the transfer matrix R between the sextupole and that point:

$$\Sigma_d = R \Sigma_a R^T \tag{9.14}$$

As there are no skew quadrupoles in the final focus, these matrices are block diagonal, so a quadrupole field will only affect the beam size, $< x\ x' >$ and $< y\ y' >$. As $< x^2 > \quad \gg \quad < y^2 >$, a skew quadrupole field will not change the horizontal beam size.

Moving sextupoles introduces quadrupole fields, so it is possible using only these displacements to correct beam divergence ($< xx' >$ and $< yy' >$ correlations).

As it is also possible to add skew quadrupole fields moving sextupoles, part of the coupling can also be corrected ($< x'y >$, $< xy' >$ correlations).

As there are sextupoles in dispersive and non-dispersive regions, as shown in figure 9.2 part of dispersion can be corrected ($< x'E >$ and $< y'E >$ correlations).

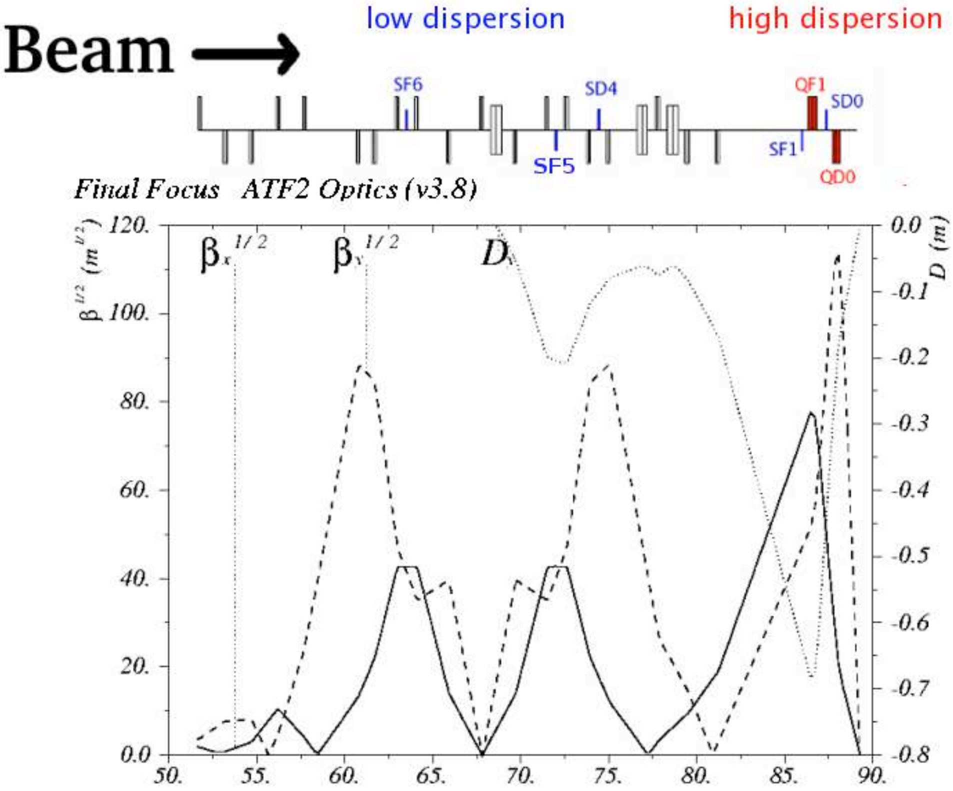

Figure 9.2: Nominal β function and dispersion function in the final focus.

The vertical positions of the beam particles at the IP function of their horizontal angles reveal a quadratic dependence, suggesting higher order correlations. It has been found that the higher order correlations which the biggest effect on the vertical beam size after the introduction of errors are $< yx'x' >_{IP}$ and $< yx'\frac{\Delta E}{E} >_{IP}$. These effects are non-linear, but it has been figured out that the same method as for the linear correlations can be used to define knobs. The knobs for these higher order aberrations are not strictly linear or orthogonal, but the simulation suggests that they are good enough to be used in an iterative procedure.

9.1.2 Knob Determination

As all the magnets after the matching section are at $\frac{\pi}{2}$ phase from the IP (see figure 9.3) and as there are no skew quadrupoles, the R transfer matrix between each element and the IP can be approximated as:

$$R = \begin{pmatrix} 0 & R_{12} & 0 & 0 & R_{15} \\ R_{21} & 0 & 0 & 0 & R_{25} \\ 0 & 0 & 0 & R_{34} & 0 \\ 0 & 0 & R_{43} & 0 & 0 \\ 0 & 0 & 0 & 0 & 1 \end{pmatrix} \tag{9.15}$$

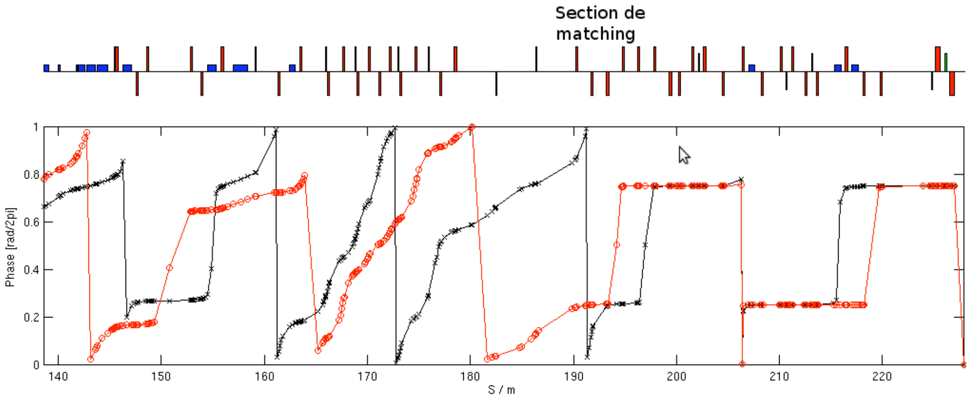

Figure 9.3: Horizontal (black) and vertical (red) phases advance along ATF2.

The effect on the beam covariance matrix at the IP introduced from a sextupole horizontal (resp. vertical) displacement equivalent to the add of quadrupole (resp. skew quadrupole) field according to equations 9.13, 9.15 and using $a = \frac{ec}{m_e} KL$, is shown equation 9.16 (resp. equation 9.17).

$$\Sigma_{effect\ quad}(IP) = R \times \Sigma_{effect}(quad) \times R^T =$$

$$\begin{pmatrix}
\begin{array}{c} R_{12}^2 a^2 < x^2 > + \\ 2R_{12}R_{15}KD_x < \frac{\Delta E}{E}^2 > \end{array} & \begin{array}{c} R_{12}(R_{21}a < x^2 > + \\ R_{25}KD_y < \frac{\Delta E}{E}^2 >) \end{array} & R_{15}R_{34}KD_y < \frac{\Delta E}{E}^2 > & 0 & R_{12}KD_x < \frac{\Delta E}{E}^2 > \\
\begin{array}{c} aR_{12}(R_{21} < x^2 > + \\ R_{25}KD_y < \frac{\Delta E}{E}^2 >) \end{array} & 0 & R_{25}R_{34}KD_y < \frac{\Delta E}{E}^2 > & 0 & 0 \\
R_{15}R_{34}KD_y < \frac{\Delta E}{E}^2 & R_{25}R_{34}KD_y < \frac{\Delta E}{E}^2 > & R34^2 a^2 < y^2 > & aR_{34}R_{43} < x^2 > & R_{34}KD_y < \frac{\Delta E}{E}^2 > \\
0 & 0 & aR_{34}R_{43} < x^2 > & 0 & 0 \\
R_{12}KD_x < \frac{\Delta E}{E}^2 > & 0 & R_{34}KD_y < \frac{\Delta E}{E}^2 > & 0 & 0
\end{pmatrix} \tag{9.16}$$

$$\Sigma_{effect\ skew}(IP) = R \times \Sigma_{effect}(skew) \times R^T =$$

$$\begin{pmatrix}
\begin{array}{c} R_{12}^2 a^2 < y^2 > + \\ 2R_{12}R_{15}KD_y < \frac{\Delta E}{E}^2 > \end{array} & R_{12}R_{25}KD_y < \frac{\Delta E}{E}^2 > & R_{15}R_{34}KD_x < \frac{\Delta E}{E}^2 > & aR_{12}R_{43} < y^2 > & R_{12}KD_y < \frac{\Delta E}{E}^2 > \\
R_{12}R_{25}KD_y < \frac{\Delta E}{E}^2 > & 0 & \begin{array}{c} R_{34}(aR_{21} < x^2 > + \\ R_{25}KD_x) < \frac{\Delta E}{E}^2 >) \end{array} & 0 & 0 \\
R_{15}R_{34}KD_x < \frac{\Delta E}{E}^2 > & \begin{array}{c} R_{34}(aR_{21} < x^2 > + \\ R_{25}KD_x) < \frac{\Delta E}{E}^2 >) \end{array} & R34^2 a^2 < x^2 > & 0 & R_{34}KD_x < \frac{\Delta E}{E}^2 > \\
R_{12}R_{34}a < y^2 > & 0 & 0 & 0 & 0 \\
R_{12}KD_y < \frac{\Delta E}{E}^2 > & 0 & R_{34}KD_x < \frac{\Delta E}{E}^2 > & 0 & 0
\end{pmatrix} \tag{9.17}$$

The $< x^2 >, < y^2 > \ and < \frac{\Delta E}{E}^2 >$ are the covariances at the sextupole position.

The element at the line i and column j (f.e. 1^{st} line, 2^{nd} column) is the coefficient between the i^{th} and the j^{th} dimensions introduced (between x and x'). That element describes the way this correlation is introduced, for example an $R_{12}(R_{21}a < x^2 >)$ element shows that a quadrupole field introduces, at the IP, an $< xx' >$ correlation due to the combined contribution of the conversion of x' to x through R_{12} and the conversion of x' to x through R_{21}.

We see also that, as the sextupoles are all at $\frac{\pi}{2}$ phase from IP, the only correlations between the beam electron positions at the IP which can be corrected using horizontal and vertical displacements of these sextupoles are $< xx' >_{IP}$ and $< yy' >_{IP}$ (waist positions at the IP), $< xy >_{IP}$, $< xy' >_{IP}$ and $< x'y >_{IP}$ (coupling at the IP), $< xE >_{IP}$ and $< yE >_{IP}$ (dispersion at the IP). Except for the effect on the beam size at IP, the effects of the sextupole displacements are linear with the displacement δ_x or δ_y since $K_{quad} = 2m\delta_x$ and $K_{skew} = 2m\delta_x$. This means the variation of the covariance coefficients $A_{ij} = \frac{<\overline{x_i}\ \overline{x_j}>}{<\overline{x_i}\ \overline{x_i}>}$ (eq. 9.6), function of the displacement of the sextupole in simulation, is linear. So we can deduce the matrix M giving the relation between the displacements δ_{xy} of the sextupoles and the desired coefficient A:

$$A = M \times \delta_{xy} \tag{9.18}$$

with:

$$A = \begin{pmatrix} \frac{1}{\Delta}\frac{<x\ x'>}{<x^2>} \\ \frac{1}{\Delta}\frac{<y\ y'>}{<y^2>} \\ \frac{1}{\Delta}\frac{<x'\ y>}{<y^2>} \\ \frac{1}{\Delta}\frac{<x\ y>}{<y^2>} \\ \frac{1}{\Delta}\frac{<\frac{\Delta E}{E}^2\ y>}{<y^2>} \\ \frac{1}{\Delta}\frac{<x'\ \frac{\Delta E}{E}^2\ y>}{<y^2>} \end{pmatrix} \text{ and } \delta_{xy} = \begin{pmatrix} \delta_x(SF6FF) \\ \delta_x(SF5FF) \\ \delta_x(SD4FF) \\ \delta_x(SD2FF) \\ \delta_x(SF1FF) \\ \delta_x(SD0FF) \\ \delta_y(SF6FF) \\ \delta_y(SF5FF) \\ \delta_y(SD4FF) \\ \delta_y(SD2FF) \\ \delta_y(SF1FF) \\ \delta_y(SD0FF) \end{pmatrix}$$

The M matrix can be easily obtained in simulation because applying the i^{th} movements in the δ_{xy} vector fills the corresponding i^{th} column in the M matrix with the simulated variations of the covariance coefficients normalized by the Δ displacement.

As this M matrix gives the relation between the A coefficients and the δ_{xy} displacements, to get the needed displacements for the chosen A coefficients, we have:

$$\delta_{xy} = M^{-1} \times A \tag{9.19}$$

In fact, the i^{th} line of the M^{-1} matrix gives the combination of sextupoles displacements needed to introduce only the i^{th} A coefficient. That matrix line is called knob for the corresponding correlation.

From equations 9.16 and 9.17, if we use the formalism σ_x and σ_y for the beam sizes at the IP without the sextupole effects, the beam sizes at the IP ($\sqrt{< x^2 >_{IP}}$ and $\sqrt{< y^2 >_{IP}}$) function of the beam sizes at the sextupole $< x^2 >_{sext}$

and $< y^2 >_{sext}$ become:

$$\begin{aligned}
\sqrt{< x^2 >_{IP} (quad)} &= \sqrt{\sigma_x + R_{12}^2 a^2 < x^2 >_{sext} + 2R_{12}R_{15}KD_x} \\
\sqrt{< y^2 >_{IP} (quad)} &= \sqrt{\sigma_y + R_{34}^2 a^2 < y^2 >_{sext}} \\
\sqrt{< x^2 >_{IP} (skew)} &= \sqrt{\sigma_x + R_{12}^2 a^2 < y^2 >_{sext} + 2R_{12}R_{15}KD_y} \\
\sqrt{< y^2 >_{IP} (skew)} &= \sqrt{\sigma_y + R_{34}^2 a^2 < x^2 >_{sext} < \frac{\Delta E}{E}^2 >_{sext}}
\end{aligned} \tag{9.20}$$

As $K_{quad} = 2m\delta_x$, $K_{skew} = 2m\delta_y$ and $a = \frac{ec}{m_e} 2mL\delta_x y$, the square of the beam size is a parabolic function of the displacement of the sextupole, with the minimum for a 0 displacement between the sextupole and the beam (corresponding to no field introduced).

9.1.3 *Simulation results*

The simulation of these displacements has been made with the tracking code PLACET [35]. The errors indicated in table 8.1 have been used in the simulation to perturb the nominal beam line. Steering is the first correction introduced and the algorithm employed is the same as the one described in section 8.2.

The proposed correction of the beam size, is a basic and very robust method, even if it is not as precise as some of the more advanced methods[42][43], it has the possibility to be implemented easily as it only requires sextupole displacements, beam size measurements and parabolic fits. It has been shown in simulation to be applicable just after the trajectory correction.

At the IP, as the beam with the nominal unperturbed lattice is at a focal point the $< x\, x' >$ and $< y\, y' >$ nominal variances are zeros; as it is uncoupled, the $< x\, y >$, $< x'\, y >$, $< x\, y' >$ and $< x'\, y' >$ nominal variances are zeros too; as the nominal dispersion functions are zero, $< x\, \frac{\Delta E}{E} >= 0$ and $< y\, \frac{\Delta E}{E} >= 0$. As the optics has been designed to correct for the second orders effects too, variances like $< x'^2\ y >$ and $< x' \frac{\Delta E}{E}\ y >$ are also zero. However, the perturbations we applied induce these correlations.

To find the positions of the sextupole centers with respect to the beam, the bigger correlations are scanned according to the corresponding knob coefficients (fives measurements are made in the simulation) then, a parabola is fitted according to the square of the beam size and the correction is applied setting the knob value at the minimum of the parabola.

This is made for the correlations found to have the biggest influence on the vertical beam size. Once corrected for:

- $< x\ x' >$: This term is related to the horizontal waist position. It strongly affects the horizontal beam size. Correcting for it reduce the influence of the coupling on the vertical beam size.

- $< y\ y' >$: This term is related to the vertical waist position, when it equal to zero, the waist is at the IP location.

- $< x'\ y >$: this term is related to the coupling, it increases the vertical beam size proportionally to the large horizontal beam size in the sextupoles. It has to be zero in order to have an uncoupled beam.

- $< y\ E >$: this term is related to the dispersion. When it is zero, there is no more dispersion at the IP.

- $< x'^2 y >$ and $x' \frac{\Delta E}{E}\ y$ are the second order terms acting on the vertical beam size. They are easy to create with the sextupole movers since x and $\frac{\Delta E}{E}$ are big in the sextupoles and the phase between the sextupoles and IP is $\frac{\pi}{2}$.

These six knobs are computed to be orthogonal which means modifying the knob corresponding to a given correlation will not affect the other correlations.

That is possible thanks to the linearity of the effects with the displacements (see equations 9.13 and 9.17). However it does not seem to be valid for the last two 3rd order variances ($< x'^2 y >$ and $x' \frac{\Delta E}{E}\, y$). Iterations in the correcting procedure are therefore needed.

If an applied correction does not decrease the beam-size, it is canceled. The range of the parabola is taken at the beginning to increase the vertical beam size by a factor around four and that range is decreased by a factor two at each successful correction. Nevertheless if the parabolic fit becomes problematic, the range is increased by a factor two. The start range has been chosen to include, in most of the case, the minimum of the parabola in order to improve the fit precision. The range is decreased after a successful correction because the minimum of the parabola is then shifted to be around zero for the next correction, again to increase the parabola fit precision. In the case where a correction is found to be very small, it is skipped in the next iteration, increasing the overall speed of the algorithm.

None of the corrections presented in chapter 6, except the steering correction, has been implemented in the simulation. The error on the beam size measurement has not been simulated either. The present simulation has been made with several error configurations changing the misalignments of the magnets, decreasing them down to $0.1\times$ the nominal misalignments. In order to see the robustness of the algorithm, they have also been increased up to $1.5\times$ the nominal misalignments. 100 simulations (100 seeds) have been made for each misalignment category, in steps of $0.1\times$.

In the commissioning process, the beam size tuning has been planned to be tested, at the beginning, with higher β function at the IP (bigger beam sizes) to make the tuning procedure easier. To see how the algorithm reacts to the easier tuning procedures, the simulations of the beam size tuning previously described have been done with the following configurations:

- the nominal beam line
- a configuration with $4 \times \beta_y$
- a configuration with $4 \times \beta_x$ and $4 \times \beta_y$

The figures 9.4 shows, for each of these β configurations, the proportion of seeds which have a vertical beam size below $1.2\times$, $2.4\times$ and $12\times$ the nominal beam sizes after 800 beam size measurements.

As a beam size measurement performed with the Shintake monitor takes about $1min$, the 800 beam size measurements correspond, in time, to about $16h$. As a correction uses 5 measurements to fit the parabola, it means 160 corrections are applied.

For the nominal beam line, for example, to have 80% of the seeds going below $44nm$ and 100% below $88nm$, the displacements have to be $\frac{1}{2}$ of the estimated ones, which means the corrections, which has not been simulated between the steering and the sextupoles knobs scans, must be effective enough to get a beam line perturbed down to this level. At the estimated displacement level, only 50% of the seeds are below $44nm$ and 80% below $88nm$.

Another observation is that with a configuration with $4 \times \beta_y$ (twice the vertical beam size) at the IP, we obtain almost 80% of the seeds below $88nm$ and 90% of the seeds below $176nm$. The described algorithm can be used directly after the steering with this configuration. Nevertheless, to obtain a $88nm$ vertical beam size using the algorithm with the nominal configuration, even if the correction is not perfect, the nominal β configuration shows better proportions of seeds than the $4 \times \beta_y$ configuration.

Also, increasing β_x does not seem to help the tuning process as the configuration with $4 \times \beta_x$ and $4 \times \beta_y$ at IP shows worse results than the configuration with $4 \times \beta_y$ at IP.

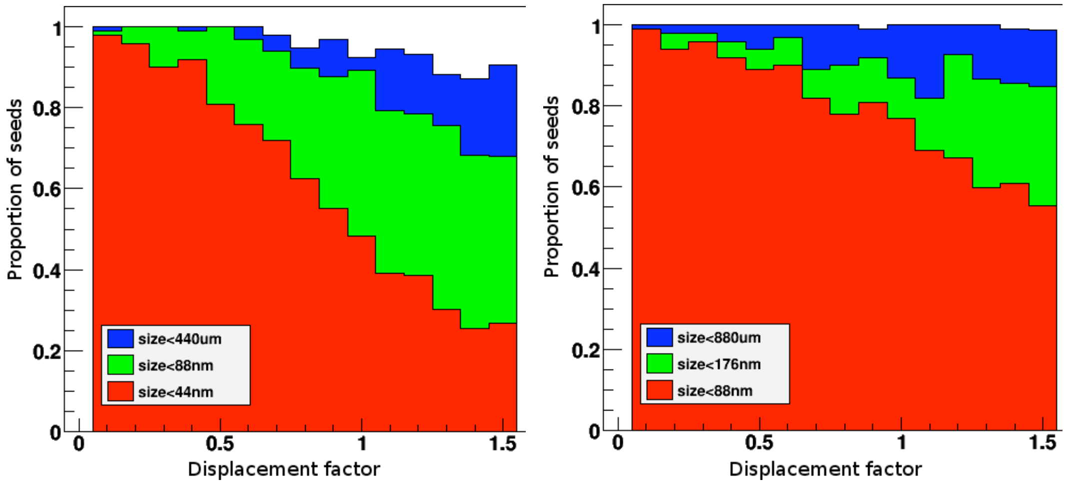

(a) Nominal beam line

(b) $4 \times \beta_y$, nominal β_x

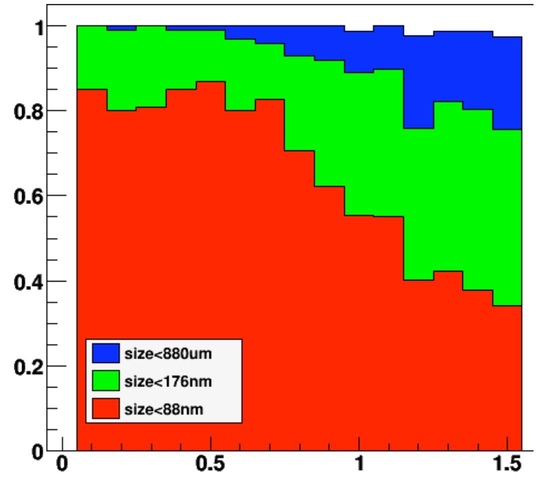

(c) $4 \times \beta_y$, $4 \times \beta_x$

Figure 9.4: Proportion of seeds which has a vertical beam size below $1.2\times$ (in red), $2.4\times$ (in yellow) and $12\times$ (in blue) the nominal beam size after 800 beam size measurements function of the misalignment factor.

The figures 9.5 shows, for each beta configuration, the proportion of seeds which have reached 110% of the minimal achievable size in less than 200, 400 and 800 beam size measurements.

Concerning the convergence speed, with the nominal configuration and the estimated displacements, we get 40% of the seeds reaching $1.1\times$ the minimum beam size before 200 beam size measurements ($3h20$), 70% before 400 beam size measurements and in 10% of cases, more than 800 beam size measurements are needed. However if the other corrections performance improves the beam line in such a way that it can be compared to a beam line with the displacements of a half of the estimated ones, we get 70% of the seeds which reach $1.1\times$ the minimum beam size before 200 beam size measurements and over 90% before 400.

Increasing the β function at IP increases the convergence speed because the proportion of seeds reaching $1.1\times$ the minimum beam size before a specified number of beam size measurements increases. It becomes reasonable (with chances over 80%) to reach $1.1\times$ the minimum beam size before 400 beam size measurements for $4\times\beta_y$ configuration and even before 200 beam size measurements for the $4\times\beta_x$ and $4\times\beta_y$ configuration.

In conclusion, this simple method can be used with the nominal configuration of the ATF2 beam line with high chances to succeed reaching the vertical beam size desired if the corrections in the extraction line have successfully improved the beam line status in such a way that the misalignments of the magnets are half of the estimated initial ones. In that case, the full corrections procedure would take about $4h$. It appears also, that using that algorithm, the minimum vertical beam size obtained in 80% of the cases for nominal displacements does not depend on the β functions and is about $88nm$. However increasing the β functions reduce the number of corrections needed to reach that minimum. Also, an increase of the β_y function by a factor 4 is enough to

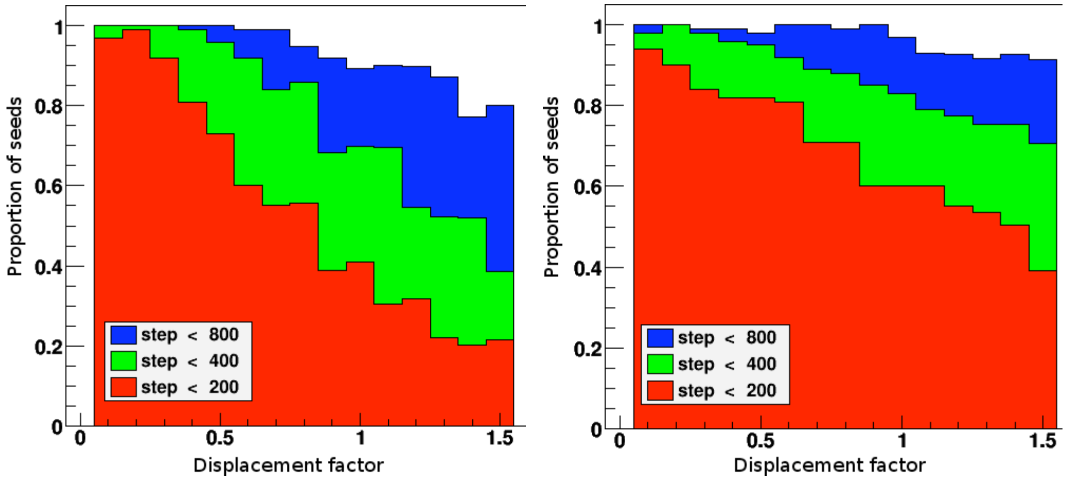

(a) Nominal beam line

(b) $4 \times \beta_y$, nominal β_x

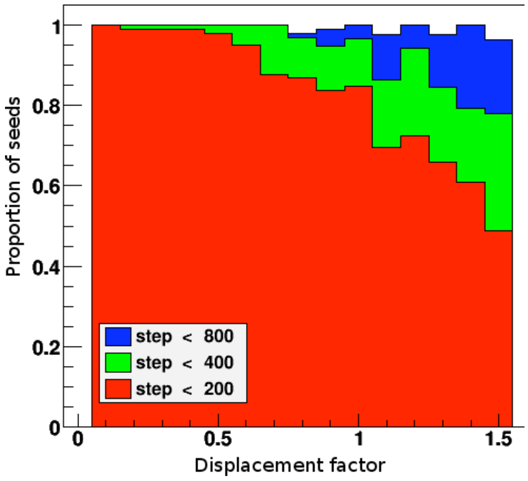

(c) $4 \times \beta_y$, $4 \times \beta_x$

Figure 9.5: Proportion of seeds which has reached 110% of the minimal achieved size before the step 200 (in red), 400 (in yellow) and 800 (in blue).

enable applying this correction method just after the steering correction since 80% of the seeds reached the minimum beam sizes with nominal errors.

However, to fully estimate the robustness and performance of this method, we need to simulate the influence of the precision of the beam size measurements by the Shintake monitor. Also, a separate study of the influence of the incoming errors in the final focus and of the final focus errors themselves would be important to define an experimentally usable criteria on quantifying the quality of the previous corrections.

Chapter 10

CONCLUSION AND PROSPECTS

10.1 Conclusion

During the 3 years of my PhD, I contributed to the ATF2 experiment and commissioning, especially concentrating on the most urgent topics during the year I spent at KEK (Tsukuba - Japan). It allowed me to take care of several aspects of ATF2, from the testing of the electronics of the stripline BPMs to the conception of several algorithms and their experimental implementation.

The testing of the stripline BPM electronics allowed to determine that due to the noise from the two kickers, another electronics at higher frequency should be used to gain in resolution and stability. This change of the electronics has been made at the beginning of this year, and the first results (unpublished yet) are very promising.

I developed several tools which are now available to the collaboration using an advanced control system called the Flight Simulator. The usage of this versatile control system allowing both the offline full simulation of ATF2 beam line and the control of the ATF2 lattice, helped me a lot in the development of the tools and made me more familiar with control systems I did not know.

The first tool I developed was for simple matrix transfer measurements, but it has been found to be very useful to find discrepancies between the model and the actual ATF2 accelerator. The second tool I developed was to correct the trajectory in the extraction and final focus beam line. Despite a sporadic bug in corrector strength assignments, it has been successfully tested and the experimental results agree well with the simulation (with a spread of BPM reading after correction of $\simeq 0.5mm$ horizontally and $\simeq 0.2mm$ vertically). The last developed tool allows to reconstruct the parameters of the beam trajectory fluctuations. That reconstruction has been made possible only thanks to the high resolution cavity BPMs and results show a resolution of the reconstruction of the beam trajectory fluctuations below $1\mu m$ all along the beam line dominated by the systematic effects such as BPM scale factors and errors on the model transfer matrices. The reconstruction of the parameters of the fluctuations allowed to reconstruct the dispersion too. The dispersion reconstruction is dominated by the same systematic errors as the reconstruction of the trajectory fluctuation parameters, so it appears that introducing beam energy variations with the ring cavity has little influence on the precision of the dispersion measurement, which was found to be a few millimeters.

Prior to the ATF2 commissioning, I developed in simulation a beam size tuning procedure using sextupole displacements, simple but robust, which could be used in the high β configuration. In that scenario, it has been found that only trajectory corrections would be necessary before applying the beam size tuning procedure and reaching in most of the cases the minimum beam size.

10.2 Prospects

Now that the stripline BPMs electronics has been upgraded, we should be able to use them in all the tools presented while they have been mostly ignored up to now. Also, the additional monitors planned (IPBPMs, tilt monitors) will provide an increase of the precision of the trajectory measurement.

The tools themselves may be also improved. As mentioned before, an automated determination of the causes of the differences between the model and the measured transfer matrices would be very helpful in the transfer matrix check tool.

The orbit fluctuation reconstruction is limited by systematic errors. The precision of the reconstruction would be largely increased if the dominant systematic errors were corrected. The use of the upgraded stripline BPMs would be especially nice in that tool because it would allow consistency checks of the reconstructed trajectory all the way to the beginning of the line.

The dispersion measurement tool will benefit twice from the better understanding of the systematics: first because it uses the energy reconstruction in the estimation of the dispersion at each BPM, secondly because the global dispersion fit is limited by the same systematics as the fluctuation recontruction. Experimental test of the proposed dispersion correction would be nice too.

The method of beam size tuning using sextupole displacements is probably the topic where further studies would be the most productive, mainly because that work has been stopped when the ATF2 commissioning started. In simulation, the influence of the measured beam size resolution would be the first thing to check, as we expect a larger tolerance on beam size measurement errors as compared to other methods. The reason because those errors has little influence on the determination of the abscissa of the parabola minimum as long as the two sides of the parabola are measured. Obviously, an experimental test of this method would be very nice too !

Appendix A

LINEAR OPTICS

A.1 Twiss Parameters

A.1.1 Beam Motion in magnet systems

The coordinate system chosen for accelerator physics is usually curved and follows a reference trajectory (see fig. A.1). That reference trajectory is the trajectory of a hypothetical particle with the initial design position and energy.

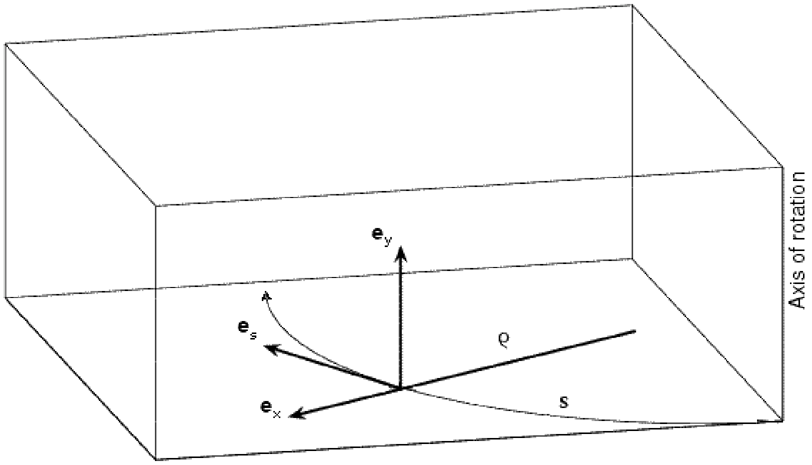

Figure A.1: Curved coordinate system following a reference trajectory.

In this coordinate system, in the linear approximation, trajectories are described by equations A.1 where $\rho = -\frac{p}{qB_y}$, $k = \frac{e}{p}\frac{\partial B_y}{\partial x}$ and Δp is the momentum difference from the design momentum p_0:

$$\begin{aligned} y'' + ky &= 0 \\ x'' - (k - \tfrac{1}{\rho^2})x &= \tfrac{1}{\rho}\tfrac{\Delta p}{p_0} \end{aligned} \tag{A.1}$$

or:

$$w'' + K(s)w = \frac{1}{\rho}\frac{\Delta p}{p_0} \text{ with} \begin{cases} K & = \quad k \qquad \text{for w=y} \\ K & = \quad -(k - \frac{1}{\rho^2}) \quad \text{for w=x} \end{cases} \tag{A.2}$$

Equation A.2 is called Hill's equation and the general solution is given by equation A.3 for sections where K and ρ are constants. This condition is valid piecewise all along the beam line for the case of the hard hedge model. In the hard edge model the strength of the magnet is assumed zero everywhere unless along the magnetic length where it is assumed constant.

$$\begin{pmatrix} w \\ w' \\ \frac{\Delta p}{p_0} \end{pmatrix}_s = \begin{pmatrix} C & S & D \\ C' & S' & D' \\ 0 & 0 & 1 \end{pmatrix} \times \begin{pmatrix} w \\ w' \\ \frac{\Delta p}{p_0} \end{pmatrix}_0$$

with, if $K = 0$

$$\begin{pmatrix} C & S & D \\ C' & S' & D' \end{pmatrix} = \begin{pmatrix} 1 & s & 0 \\ 0 & 1 & 0 \end{pmatrix}$$

if $K > 0$ (focusing)

$$\begin{pmatrix} C & S & D \\ C' & S' & D' \end{pmatrix} = \begin{pmatrix} \cos(s\sqrt{|K|}) & \frac{1}{\sqrt{|K|}}\sin(s\sqrt{|K|}) & \frac{1}{\rho|K|}(1-\cos(s\sqrt{|K|})) \\ -\sqrt{|K|}\sin(s\sqrt{|K|}) & \cos(s\sqrt{|K|}) & \frac{1}{\rho\sqrt{|K|}}\sin(s\sqrt{|K|}) \end{pmatrix}$$

and, if $K < 0$ (defocusing)

$$\begin{pmatrix} C & S & D \\ C' & S' & D' \end{pmatrix} = \begin{pmatrix} \cosh(s\sqrt{|K|}) & \frac{1}{\sqrt{|K|}}\sinh(s\sqrt{|K|}) & -\frac{1}{\rho|K|}(1-\cosh(s\sqrt{|K|})) \\ \sqrt{|K|}\sinh(s\sqrt{|K|}) & \cosh(s\sqrt{|K|}) & \frac{1}{\rho\sqrt{|K|}}\sinh(s\sqrt{|K|}) \end{pmatrix} \tag{A.3}$$

A.1.2 Twiss Functions

An other way to write the general solution of Hill's equation $w'' + Kw = 0$ is:

$$\begin{aligned} w(s) &= \sqrt{\epsilon\beta(s)}\cos(\Phi(s) - \Phi_0) \\ &= \sqrt{\epsilon\beta(s)}\cos(\Delta\Phi) \end{aligned} \tag{A.4}$$

with the phase function defined as: $\Phi(s) = s\sqrt{|K|} = \int_{s_0}^{s} \frac{\mathrm{d}s}{\beta(s)}$.

$\beta(s)$ is called the β function and ϵ, which is a constant when the energy of the beam does not change, can be identified to the emittance for a particle at one standard deviation of the particle distribution. In the linear approximation, the normalized emittance $\epsilon_n = \beta\gamma\epsilon$ does not change with the energy.

The β function can be determined solving equation A.5 using the three Twiss functions $\alpha(s)$, $\beta(s)$ and $\gamma(s)$:

$$\begin{aligned} &\alpha'(s) - \gamma(s) + K(s)\beta(s) = 0 \\ &\text{with: } \gamma(s) = \tfrac{1+\alpha(s)^2}{\beta(s)} \\ &\text{and } \alpha(s) = \tfrac{\beta'(s)}{2} \end{aligned} \tag{A.5}$$

The particle distribution in phase space is an ellipse parameterized by the Twiss functions as shown figure A.2. The tilt is parameterized by $-\frac{\alpha}{\beta}$, the spatial spread by $\sqrt{\epsilon\beta}$ and the angular spread by $\sqrt{\epsilon\gamma}$.

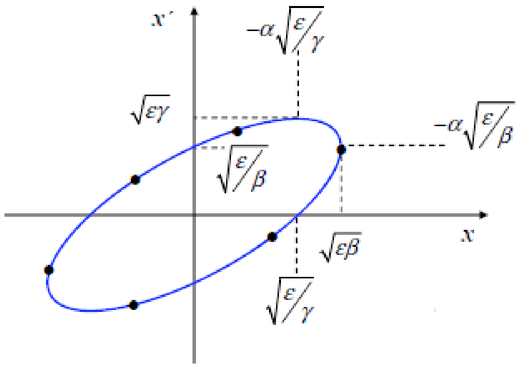

Figure A.2: Beam ellipse function of the twiss functions.

The square root of the β function is proportional to the amplitude of the beam oscillations and to the beam size. The phase advance $\Delta\Phi$ determines how displacements of the beam are converted in angles and vice versa. For example a displacement is totally converted in angle between two points separated by a phase advance of $\frac{\pi}{2}$ and in the case of phase advance of 0 or π the magnification is given by the ratio of the square root of the β functions (see eq. A.6). This formalism is very similar to conventional linear optics.

The relation between w, w' and w_0, w'_0 can be written using the same formalism as in equation A.3 using the Twiss functions the equation A.4:

$$\begin{pmatrix} w \\ w' \end{pmatrix}_s = \begin{pmatrix} C & S \\ C' & S' \end{pmatrix} \times \begin{pmatrix} w \\ w' \end{pmatrix}_0$$

with

$$\begin{pmatrix} C & S \\ C' & S' \end{pmatrix} = \begin{pmatrix} \sqrt{\frac{\beta}{\beta_0}}(\cos\Delta\Phi + \alpha_0 \sin\Delta\Phi) & \sqrt{\beta_0\beta}\sin\Delta\Phi \\ -\frac{1}{\sqrt{\beta_0\beta}}\left[(\alpha - \alpha_0)\cos\Delta\Phi + (1 + \alpha\alpha_0)\sin\Delta\Phi\right] & \sqrt{\frac{\beta}{\beta_0}}(\cos\Delta\Phi - \alpha\sin\Delta\Phi) \end{pmatrix} \tag{A.6}$$

A.2 Transfer Matrices

As we saw above, the parameters of the beam (x, x', y, y', z and $\frac{\delta E}{E}$) can be determined anywhere in the accelerator if they are known at one reference position, using the lattice properties. The matrix $R(ref \to s)$, called transfer matrix, gives the parameter evolution between the reference position (ref) and the position s.

As the beam is relativistic and there is no chicane in ATF2, z is constant so we will ignore it in the following.

$$\begin{pmatrix} x \\ x' \\ y \\ y' \\ \frac{\delta E}{E} \end{pmatrix}_s = R \times \begin{pmatrix} x \\ x' \\ y \\ y' \\ \frac{\delta E}{E} \end{pmatrix}_0$$

From eq. A.3, we saw how to calculate R in a constant field (i.e. in a single magnet or drift space). To obtain the overall transfer matrix for a more complex system, we have to multiply from left the transfer matrices of each element:

$$R_{0\to 3} = R_{2\to 3} \cdot R_{1\to 2} \cdot R_{0\to 1} \tag{A.7}$$

The transfer matrices in the hard edge approximation for the most used elements are given below.

A.2.1 Drift space

The drift space is the simplest element with no magnetic field at all ($\frac{1}{\rho} = 0$ and $K = 0$). For a drift space of length l:

$$R_{\text{drift}} = \begin{pmatrix} 1 & l & 0 & 0 & 0 \\ 0 & 1 & 0 & 0 & 0 \\ 0 & 0 & 1 & l & 0 \\ 0 & 0 & 0 & 1 & 0 \\ 0 & 0 & 0 & 0 & 1 \end{pmatrix}$$

A.2.2 Quadrupole Magnet

A quadrupole magnet is an element with four poles (see fig. A.3) where the field is proportional to the distance from the center ($\frac{1}{\rho} = 0$ and $K = \text{const}$). For $k > 0$ there is horizontal defocusing and vertical focusing. It is the opposite case for $k < 0$. For a quadrupole magnet of strength k and length l with $\Phi = l\sqrt{|k|}$:

$$R_{\text{quad}} = \begin{pmatrix} \cosh\Phi & \frac{1}{\sqrt{|k|}}\sinh\Phi & 0 & 0 & 0 \\ \sqrt{|k|}\sinh\Phi & \cosh\Phi & 0 & 0 & 0 \\ 0 & 0 & \cos\Phi & \frac{1}{\sqrt{|k|}}\sin\Phi & 0 \\ 0 & 0 & -\sqrt{|k|}\sin\Phi & \cos\Phi & 0 \\ 0 & 0 & 0 & 0 & 1 \end{pmatrix}$$

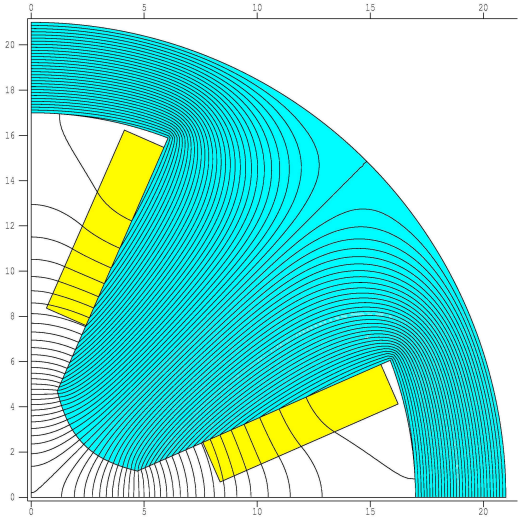

Figure A.3: Field (quarter profile) of a quadrupole magnet. The iron core is shown in blue and conductors in yellow.

In the case where the length of the quadrupole is small compared to its focal length $f = \frac{1}{kl}$, $l \ll f$ and $l \ll 1$, it can be represented by a thin lens positioned at its center. With this thin lens approximation the transfer matrix becomes (for a horizontally defocusing quadrupole):

$$R_{\text{quad}} = \begin{pmatrix} 1 & 0 & 0 & 0 & 0 \\ \frac{1}{f} & 1 & 0 & 0 & 0 \\ 0 & 0 & 1 & 0 & 0 \\ 0 & 0 & -\frac{1}{f} & 1 & 0 \\ 0 & 0 & 0 & 0 & 1 \end{pmatrix}$$

A.2.3 Skew Quadrupole Magnet

A skew quadrupole is a quadrupole rotated by $\frac{\pi}{4}$. It introduces coupling between the horizontal and vertical planes; it is usually used to correct rotation errors in the other elements of the beam line. The transfer matrix of a skew quadrupole of length l and strength k is (with $\Phi = \sqrt{k}l$), in thin lens approximation:

$$R_{\text{skew quad}} = \begin{pmatrix} 1 & & 0 & 0 & 0 \\ 0 & 1 & -kl & 0 & 0 \\ 0 & 0 & 1 & 0 & 0 \\ -kl & 0 & 0 & 1 & 0 \\ 0 & 0 & 0 & 0 & 1 \end{pmatrix}$$

A.2.4 Sector Magnet

The sector magnet is a dipole magnet ($B(x, y) = \text{const} \Rightarrow \rho = \text{const}$ and $K = 0$) shaped to be orthogonal to the beam trajectory at its entry and exit (see fig. A.4). For a horizontal sector magnet of length l and bending radius ρ with

$\Phi = \frac{l}{\rho}$, the transfer matrix is:

$$R_{\text{sector}} = \begin{pmatrix} \cos\Phi & \rho\sin\Phi & 0 & 0 & \rho(1-\cos\Phi) \\ -\frac{1}{\rho}\sin\Phi & \cos\Phi & 0 & 0 & \sin\Phi \\ 0 & 0 & 1 & l & 0 \\ 0 & 0 & 0 & 1 & 0 \\ 0 & 0 & 0 & 0 & 1 \end{pmatrix}$$

We can see that a sector magnet introduces horizontal dispersion (correlation between horizontal position and energy) and a weak horizontal focusing of strength $\frac{1}{\rho^2}$.

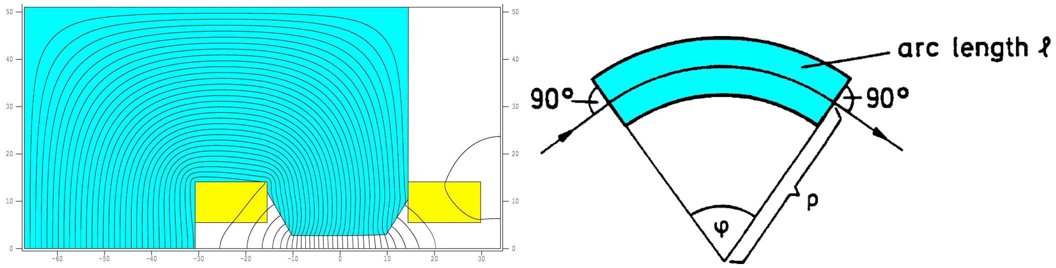

Figure A.4: Field (half of a profile) and shape (top view) of a sector magnet.

A.2.5 Sextupole

A sextupole magnet is an element with six poles (see fig. A.5). The field projections of a sextupole of strength $m = -\frac{\partial^2 B_y}{\partial^2 y}$ on the horizontal and vertical axes, are respectively $B_x = 2mxy$ and $B_y = m(x^2 - y^2)$.

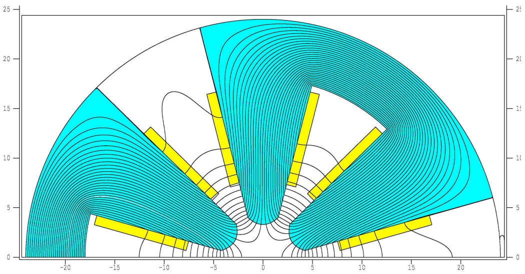

Figure A.5: Field (half of a profile) of a sextupole magnet.

GREETINGS, REMERCIEMENTS

Je tiens a remercier Guy Wormser d'avoir accepté de présider mon jury de thèse, ainsi que Frank Zimmermann et Philip Burrows pour avoir accepté d'être mes rapporteurs. Je remercie aussi Patrick Puzo, Alessandro Variola et Glen Russell White pour avoir accepté de faire partie du mon jury de thèse.

Je tiens a remercier tout particulièrement Philip Bambade, mon tuteur, pour m'avoir permis d'effectuer ce travail, pour ces innombrables conseils, sa motivation contagieuse, de m'avoir suivi au Japon et tant d'autre choses. Merci aussi à tout mes collègues de travail (et plus particulièrement Cécile, Freddy, Julien, Olivier, Nicolas, Sophie) pour votre bonne humeur et votre soutien.

I want to thanks Toshiaki Tauchi my Japonese supervisor, as well as all the ATF team for their welcoming and all the things I learned with them in the control room. I hope to come back soon ! Thanks too to the ATF secretaries to be so friendly and helpful.

I would like to thanks also all the ATF collaborators, particularly Glen Russell White, you can be proud of your baby (the Flight Simulator), the greatest tool ever in a control room ! Without your involvement, this thesis would have so much less experimental results. Thanks also to Mark Woodley for your optics and technical expertise. Thanks Stewart Boogert for your impressive work on the cavity BPMs and for all your advices.

Maria Carla merci a toi pour ton soutien, ta patience (je sais comme tu as souffert de cette année au Japon), ton aide pour la correction du manuscrit et j'en oublie surement. Bon courage pour ta thèse ;-)

Merci aussi à ma famille et tout mes amis m'ayant soutenu tout au long de

ce travail. Christophe tu pourras vraiment dire que tu m'aura suivi jusque au bout du monde, Mathieu on doit se faire faire un caps' pour fêter ça, Pauline pour ton hospitalité sans faille.

I soulaud like to thanks also all the people I met in Japan who contributed to make of the year spent there one of the best year ever. J.C., Clem, Krys, David, Chrina, Amelie and Caroline we should try to make a barbecue here once everyone came back. Sandrine and Eric thanks for your good vibes ! Yuri, Nico, Christophe and Amandine I really enjoyed being your room mate !

Finally, thank you reader.

BIBLIOGRAPHY

[1] R. Assmann, M. Lamont, and S. Myers. A brief history of the LEP collider. *Nucl. Phys. Proc. Suppl.*, 109B:17–31, 2002.

[2] F. Furuta et al. Experimental comparison at KEK of high gradient performance of different single cell superconducting cavity designs. Prepared for European Particle Accelerator Conference (EPAC 06), Edinburgh, Scotland, 26-30 Jun 2006.

[3] James Brau, (ed.) et al. International Linear Collider reference design report. 1: Executive summary. 2: Physics at the ILC. 3: Accelerator. 4: Detectors. ILC-REPORT-2007-001.

[4] M. Zobov, P. Raimondi, D. Shatilov, and K. Ohmi. Crab Waist Collision Studies for e+e- Factories. 2008.

[5] A. Mikhailichenko et al. The E166 experiment: Undulator-based production of polarized positrons. *AIP Conf. Proc.*, 915:1095–1100, 2007.

[6] T. Raubenheimer, L. Z. Rivkin, and R. D. Ruth. DAMPING RING DESIGNS FOR A TeV LINEAR COLLIDER. Contributed to DPF Summer Study: Snowmass '88, High Energy Physics in the 1990's, Snowmass, Colo., Jun 27 - Jul 15, 1988.

[7] Tor O. Raubenheimer. The Generation and acceleration of low emittance flat beams for future linear colliders. SLAC-0387.

[8] K. Kubo, M. Akemoto, S. Anderson, T. Aoki, S. Araki, K. L. F. Bane, P. Blum, J. Corlett, K. Dobashi, P. Emma, J. Frisch, M. Fukuda, Z. Guo, K. Hasegawa, H. Hayano, T. Higo, A. Higurashi, Y. Honda, T. Iimura, T. Imai, K. Jobe, S. Kamada, P. Karataev, S. Kashiwagi, E. Kim, T. Kobuki, and T. Kotseroglou. Extremely low vertical-emittance beam in the accelerator test facility at kek. *Phys. Rev. Lett.*, 88(19):194801, Apr 2002.

[9] Y. Honda et al. Achievement of ultra-low emittance beam in the ATF damping ring. *Phys. Rev. Lett.*, 92:054802, 2004.

[10] M. Berndt et al. Final focus test beam: Project design report. SLAC-0376.

[11] S. Araki et al. Proposal of the next incarnation of accelerator test facility at KEK for the International Linear Collider. SLAC-PUB-11202.

[12] Boris Ivanovich Grishanov et al. ATF2 proposal. SLAC-R-771.

[13] B. I. Grishanov et al. ATF2 proposal. Vol. 2. 2006.

[14] J. Resta-Lopez and Philip N. Burrows. Layout and Simulations of the FONT System at ATF2. EPAC'08, 11th European Particle Accelerator Conference, 23- 27 June 2008, Genoa, Italy.

[15] M. D. Woodley and P. E. Emma. Measurement and correction of cross-plane coupling in transport lines. *ECONF C*, 000821:MOc19, 2000.

[16] Pantaleo Raimondi and Andrei Seryi. A novel final focus design for future linear colliders. *Phys. Rev. Lett.*, 86:3779–3782, 2001.

[17] A Lyapin, B Maiheu, M Wing, S Shin, Y Honda, T Tauchi, N Terunuma, A Heo, E Kim, K Kim, R C E Ainsworth, S T Boogert, G Boorman, S Molloy, D McCormick, J Nelson, G White, and D Ward. Development of the c-band bpm system for atf2.. oai:cds.cern.ch:1225901. (EuCARD-CON-2009-005), 2009.

[18] A Lyapin, B Maiheu, M Wing, S Shin, Y Honda, T Tauchi, N Terunuma, A Heo, E Kim, K Kim, R C E Ainsworth, S T Boogert, G Boorman, S Molloy, D McCormick, J Nelson, G White, and D Ward. Development of the s-band bpm system for atf2. In *Proceedings of PAC09 Particle Accelerator Conference (PAC09)*, Vancouver, BC, Canada, 2009. Joint Accelerator Conferences Website.

[19] Sean Walston et al. Performance of a High Resolution Cavity Beam Position Monitor System. *Nucl. Instrum. Meth.*, A578:1–22, 2007.

[20] T Nakamura. *Development of Beam-position Monitors with High Position Resolution*. PhD thesis, 2008.

[21] D Okamoto and Y Honda. Cavity beam orbit tilt monitor studies at atf2. Presentation at the 8th ATF Technical Board Meeting, 2009.

[22] M. C. Ross et al. Wire scanners for beam size and emittance measurements at the SLC. Presented at IEEE Particle Accelerator Conf., San Francisco, CA, May 6-9, 1991.

[23] H. Hayano. Wire scanners for small emittance beam measurement in ATF. 2000.

[24] A. Aryshev et al. Micron Size Laser-wire System at the ATF Extraction Line. EPAC'08, 11th European Particle Accelerator Conference, 23- 27 June 2008, Genoa, Italy.

[25] A. Aryshev et al. Micron Size Laser-wire System at the ATF Extraction Line, Recent Results and ATF-II Upgrade. In *Proceedings of PAC09 Particle Accelerator Conference (PAC09)*, Vancouver, BC, Canada, 2009. Joint Accelerator Conferences Website.

[26] Taikan Suehara, Masahiro Oroku, Takashi Yamanaka, Hakutaro Yoda, Tomoya Nakamura, Yoshio Kamiya, Yosuke Honda, Tatsuya Kume, Toshiaki Tauchi, Tomoyuki Sanuki, and Sachio Komamiya. A nanometer beam size monitor for atf2. *Nuclear Instruments and Methods in Physics Research Section A: Accelerators, Spectrometers, Detectors and Associated Equipment*, 616(1):1 – 8, 2010.

[27] T. Shintake et al. Experiments of nanometer spot size monitor at FFTB using laser interferometry. Contributed paper at 1995 Particle Accelerator Conference and International Conference on High-Energy Accelerators, May 1 - 5, 1995, Dallas, Texas, U.S.A.

[28] T. Yamanaka et al. Status of the First Commissioning of the Shintake Monitor for ATF2. In *Proceedings of PAC09 Particle Accelerator Conference (PAC09)*, Vancouver, BC, Canada, 2009. Joint Accelerator Conferences Website.

[29] Proposal of high resolution single shot bpm electronics replacement for atf-dr. 1998. ATF-02-01.

[30] C. Rimbault et al. 4D Emittance Measurements Using Multiple Wire and Waist Scan Methods in the ATF Extraction Line. EPAC'08, 11th European Particle Accelerator Conference, 23- 27 June 2008, Genoa, Italy.

[31] S Bai. Optical configurations with variable β^* at different ip locations in atf2. ATF-08-05.

[32] P. Bambade et al. Present status and first results of the final focus beam line at the KEK Accelerator Test Facility. *Phys. Rev. ST Accel. Beams*, 13:042801, 2010.

[33] G. White, S. Molloy, A. Seryi, D. Schulte, R. Tomas, S. Kuroda, P. Bambade, and Y. Renier. A Flight Simulator for ATF2 - A Mechanism for International Collaboration in the Writing and Deployment of Online Beam Dynamics Algorithms. In *Proceedings of EPAC08 Particle Accelerator Conference (EPAC08)*, pages 1562–1564, Genoa Italie, 2008. Joint Accelerator Conferences Website. accelconf.web.cern.ch/accelconf/e08/papers/tupp016.pdf - SLAC-PUB-13304, LAL/RT 08-15.

[34] K. Hirata, S. Kamada, K. Oide, N. Yamamoto, and K. Yokoya. *SAD / Tkinter Manual (Japanese)*. KEK.

[35] D. Schulte. *The Tracking Code PLACET, http: / / dschulte.home.cern.ch / dschulte / physics / placet / placet.ps*. CERN.

[36] S. Molloy, M.T.F. Pivi, G. White, and Y. Renier. Interfacing Of Third-Party Accelerator Code With The LUCRETIA Flight Simulator. In *Proceedings of PAC09 Particle Accelerator Conference (PAC09)*, Vancouver, BC, Canada, 2009. Joint Accelerator Conferences Website.

[37] P. Tenenbaum. Lucretia: A Matlab-based toolbox for the modelling and simulation of single-pass electron beam transport systems. 2005. Contributed to Particle Accelerator Conference (PAC 05), Knoxville, Tennessee, 16-20 May 2005.

[38] Hans Grote and F. Christoph Iselin. *The MAD Program User's Reference Manual*. CERN, 5 edition. CERN/SL/90-13.

[39] M. Slater et al. Cavity BPM system tests for the ILC energy spectrometer. *Nucl. Instrum. Meth.*, A592:201–217, 2008.

[40] K. Kubo. Beam-energy fluctuation in DR, estimated from horizontal orbit. 1999. ATF-99-11.

[41] P. Emma, T. H. Fieguth, and T. Lohse. ONLINE MONITORING OF DISPERSION FUNCTIONS AND TRANSFER MATRICES AT THE SLC. *Nucl. Instrum. Meth.*, A288:313, 1990.

[42] G. R. White. IP beam size tuning. Presentation at the 7th ATF2 Project Meeting.

[43] R. Tomas. The ultra-low betas recent studies. Presentation at the 7th ATF2 Project Meeting.

[44] C. Rimbault. Coupling correction. Presentation at the 7th ATF2 Project Meeting.

[45] T. Suehara et al. R&D Status of ATF2 IP Beam Size Monitor (Shintake Monitor). 2007.

[46] K Wille. *The Physics of Particle Accelerators. An Introduction*. Oxford University Press, April 2001. ISBN13: 9780198505495.